Challenge Journal of STRUCTURAL MECHANICS

Vol.2 No.1 (2016)

ISSN 2149-8024

TULPAR ACADEMIC PUBLISHING

Challenge Journal of Structural Mechanics

E-mail: *cjsmec@challengejournal.com*

Web page: *cjsmec.challengejournal.com*

TULPAR Academic Publishing
www.tulparpublishing.com

Challenge Journal of Structural Mechanics

CONTENTS

TULPAR ACADEMIC PUBLISHING

Challenge Journal of Structural Mechanics

Impact of adjacent footings on immediate settlement of shallow footings

Mustafa Aytekin *

Department of Civil Engineering & Architecture, University of Bahrain, 32038 Isa Town, Kingdom of Bahrain

ABSTRACT

When the settlement of a footing under a structure is estimated by considering the bearing pressure of that footing only, the estimated value of the settlement may not be good enough since the other neighboring footings are going to effect the settlement of the footing under consideration also. Thus, in the settlement estimation of a footing, the effect of neighboring footings must be considered. In this study, impact of adjacent footings is considered on the estimation of elastic settlement of shallow foundations. In the estimation of elastic (immediate) settlement, the Schmertmann's method that is a very popular method in the elastic settlement estimation of shallow foundations is employed. In order to consider effect of neighboring footings on elastic settlement of main footing in different configurations, a MATLAB script has been generated. Elastic settlements of the various configurations are estimated by the script and several conclusions have been reached.

ARTICLE INFO

Article history:
Received 4 Nowember 2015
Accepted 27 January 2016

Keywords:
Elastic settlement
Shallow foundations
Schmertmann method
Effect of neighboring footings

1. Introduction

Several methods are in use for estimation of elastic (immediate) settlement of shallow footings in foundation engineering applications. Almost all of these methods consider only one isolated spread footing in the estimation of immediate settlement (Das, 2007; Coduto, 2001). In the real life of practice, it is very seldom to see a single footing is constructed. Mostly, a spread footing would have other footings around it. To estimate the elastic settlement of shallow footings that rest on granular soil like sand and/or gravel, several methods are available in the literature (Das, 2010; Cernica, 1995). Most of these methods are based on elastic approach. Modulus of elasticity, E_s, is employed in the elastic settlement calculations.

In these methods, the elastic settlement of footings estimated by considering the net pressure increment under the footing only but not considered the stress increment due to the neighboring footings at the same depth. Actually, the net stress increments under the spread footings would be larger when neighboring footings effect is considered. Thus, the estimated value of elastic settlement will be less than what is going to occur in the field since only the stress increment due to the one single footing has been considered. There are several methods to estimate the elastic settlement of shallow foundations. Schmertmann's method is one of several methods that was developed primarily as a means of estimating the spread footing settlement on sandy soils (Meyerhof, 1965; Schmertmann et al., 1978; Berardi et al., 1991). The method is employed with cone penetration test (CPT) and/or standard penetration test (SPT).

Unlike many of the other methods that are purely empirical to estimate elastic settlement, the Schmertmann's method is based on physical model in which strain influence factors are employed. Estimation of modulus of elasticity is a very important issue in the method. Thus, data from filed tests such as tip resistance of CPT or SPT-N value is used. Lee J at al., (2010) claimed that the depth of influenced zone under the isolated footing is deeper than the depth assumed by the Schmertmann's method. However, the Schmertmann's method gives reasonable estimations of shallow foundations.

2. Schmertmann's Method

The Schmertmann's method (1970) considered the variation of soil strain under a footing with an assumption of peak strain would occur at a depth of half width

* *Corresponding author*. Tel.: +973-36936675 ; Fax: +973-17680843 ; E-mail address: maytekin1@gmail.com (M. Aytekin)
ISSN: 2149-8024 / DOI: http://dx.doi.org/10.20528/cjsmec.2016.01.001

of footing ($B/2$) as seen in Fig.1. Then, the strain would be equal to zero at a depth of twice of the width of the footing. However, when he had more investigation Schmertmann (1978) proposed a modified variation of strain within the depth as seen in Fig.2.

In the modified model there are two types of stain variations. One of them is for axisymmetric problems that are for spread footings. The other one is for plane strain problems that are for strip footings.

The method uses a simple triangular strain distribution that was corrected in 1978 as seen in Fig. 1, and estimates the strain influence factor at the midpoint of each layer. Then using the proper strain influence factors estimates the elastic settlement of a footing. Later on, a time factor also be included to account for time dependent (creep) effects. However, the author does not believe it is essential on the calculation of immediate settlement that is assumed to be independent of time. In the method, an *influence factor*, I_z is defined depends on the type of the problem. The problem can be either an axisymmetric or plain strain state. In the axisymmetric state, I_z has a value of 0.1 at the base level of the footing and then varies linearly to a peak value of I_{zp} at a depth of $B/2$. After the peak value of strain influence, it diminishes to zero at a depth of $2B$. In the plane strain state I_z has a value of 0.2 at the base level of the foundation and then varies linearly to a peak value of I_{zp} at a depth of B. After the peak value of strain influence, it diminishes to zero at a depth of $4B$ as seen in Fig. 2.

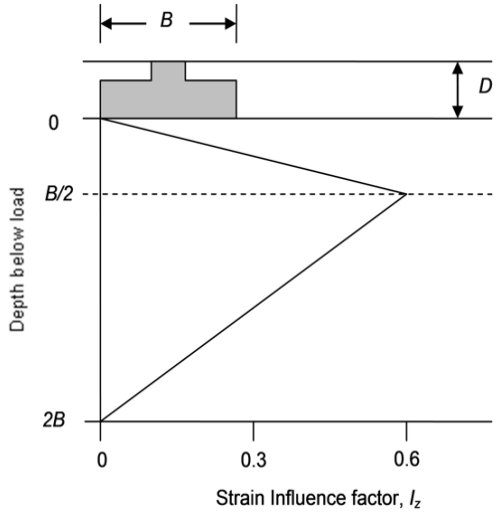

Fig. 1. Variation of strain under a footing (Schmertmann, 1970).

The peak value for influence factor, is calculated by Eq. (1)

$$I_{zp} = 0.5 + 0.1\sqrt{\frac{q-\sigma'_{zD}}{\sigma'_{zp}}}\,, \qquad (1)$$

where

σ'_{zD} = effective overburden pressure at bottom of the footing

q = the applied footing pressure (contact pressure)

σ'_{zp} = effective stress at the depth of $B/2$ for axisymmetric strain (square and circular footing), and effective stress at the depth of B for plane strain (strip footing)

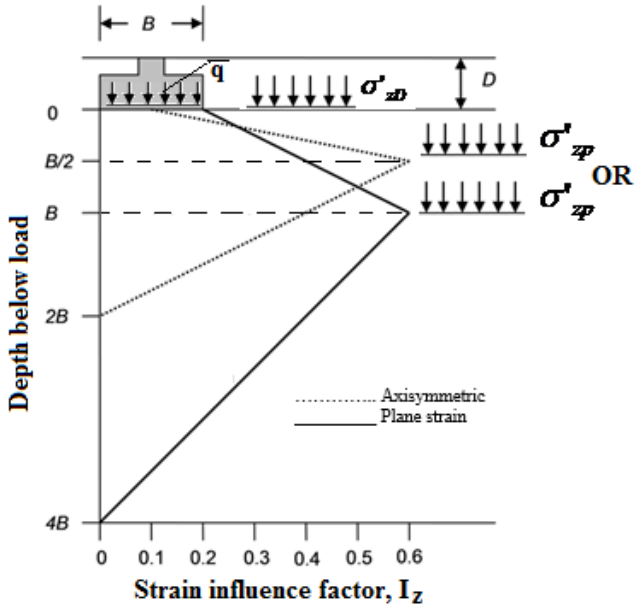

Fig. 2. Strain influence factors (Schmertmann et al. 1978).

According to Fig.1, the exact value of I_{zi} at any depth can be determined as follows;

For square and circular footings (L/B=1)

$$I_z = 0.1 + \frac{z}{B}(2I_{zp} - 0.2) \quad if \quad \left(0 \le z \le \frac{B}{2}\right), \qquad (2)$$

$$I_z = 0.667 I_{zp}\left(2 - \frac{z}{B}\right) \qquad if \quad \left(\frac{B}{2} \le z \le 2B\right), \qquad (3)$$

For strip (continuous) footings $\frac{L}{B} \ge 10$

$$I_z = 0.2 + \left(\frac{z}{B}\right)(I_{zp} - 0.2) \quad if \quad (0 \le z \le B), \qquad (4)$$

$$I_z = 0.333 I_{zp}\left(4 - \frac{z}{B}\right) \qquad if \quad (B \le z \le 4B), \qquad (5)$$

For rectangular footings in which the length is greater than ten times the width, the plane strain approach is used. For rectangular loads in which the length is less than ten times the width, a linear interpolation between the axisymmetric and plane strain case is performed, dependent on the length to width ratio.

For rectangular footings $1 < \left(\frac{L}{B}\right) < 10$

$$I_z = I_{zp} + 0.111(I_{zc} - I_{zs}) * \left(\frac{L}{B} - 1\right), \qquad (6)$$

where

I_{zc} = strain influence factor for strip footing that has a width of B,

I_{zs} = strain influence factor for square footing that has a width of B, this value must be at least zero or larger.

The equation for settlement is:

$$S_i = C_1 C_2 C_3 (q - \sigma'_{zD}) \sum_{i=1}^{n} \frac{\Delta z_i I_{zi}}{E_{si}}, \qquad (7)$$

where

$$C_1 = 1 - 0.5\left(\frac{\sigma'_{zD}}{q-\sigma'_{zD}}\right), \quad (8)$$

the correction to account for strain relief from excavated soil

$$C_2 = 1 + 0.2\,log\left(\frac{t}{0.1}\right), \quad (9)$$

correction for time-dependent creep

$$C_3 = 1.03 - 0.03\left(\frac{L}{B}\right) \geq 0.73\ , \quad (10)$$

the correction for shape of the footing base

t = time (years)

E_{si} = one-dimensional elastic modulus of soil layer i

Δ_{zi} = thickness of soil layer

I_{zi} = the influence factor at the centre of soil layer i as described below.

The elastic modulus E_s can be estimated from the results of a Cone Penetration test:

$E_s = 2.5q_c$ (1978 formulation, axisymmetric footing)

$E_s = 3.5q_c$ (1978 formulation, plane strain footing)

where q_c is the cone tip bearing resistance. If the Schmertmann's 1978 formulation is being used, the value for E_s is calculated to be between the axisymmetric case and plane strain case if the length of the footing is less than ten times the width.

The accuracy of the Schmertmann's method improves when the strain profile is sampled more densely. If the soil profile is fairly homogeneous, it is tedious to specify many layers with the same properties in order to improve the accuracy.

3. Effect of Adjacent Footings on Settlement

In the elastic settlement estimation of footings, interactions between adjacent footings are not taken into account in the conventional approach. However, it is noted that shallow foundations for typical buildings consist of multiple footings that are generally in close proximity.

In this paper, four configurations that could be possible in practice seen in Fig.2 have been considered: a) only main footing, b) one adjacent footing c) two adjacent footings d) three adjacent footings d) four adjacent footings. A MATLAB code has been generated to calculate the settlement under the footing by the Schmertmann's Method for the four cases mentioned. In order to simplify the problem it is assumed that all of the footings have identical contact pressure and their bases are square with a width of B. However, different widths and contact pressures can also be considered for the practical applications. In the estimation of stress increment under the footing at a depth of $B/2$, the stress increments due to the neighboring footings are considered by Boussinesq's theory (Fig.3). Then, as it is seen in Fig. 4, an increment on bearing pressure of footing under which the settlement would be estimated is back calculated and added to the contact pressure at the base of the footing. This process is repeated up to the number of adjacent footings that may have impact on the settlement. Then, settlement of the footing is calculated for the four different configurations seen in Fig. 3 by the Schemertmann's method that has been programmed in the MATLAB script.

In the modeling of the problem L1= L2=L is assumed. Also, four cases have been investigated namely "Case I, L/B=0.5", "Case II, L/B=0.75", "Case III, L/B=1", and "Case IV, L/B=3". In each case, the number of the neighboring footings has been varied from 1 to 4 with respect to the configurations seen in Fig. 3. Then, four different settlements were calculated by the MATLAB script.

The calculated increments of settlements due to the adjacent footings have been normalized by dividing the settlement of main footing with no adjacent footing. Finally, normalized settlement increments versus number of adjacent footings have been plotted as seen in Fig.4. As it is seen in Fig.4, stress increments due to adjacent footings at the depth of $B/2$ under the foundation for which the settlement will be calculated. Depend on the number of adjacent footings, all the stress increments are superimposed under the main foundation at the depth of $B/2$ at which the strain increment is the maximum.

The percentages of settlement increments can be estimated by the following equations found for the cases investigated in this study.

$$\text{Case}I \qquad S_p = 1.6981n - 0.0046\ , \quad (11)$$

$$\text{Case}II \qquad S_p = 0.731n - 0.0008\ , \quad (12)$$

$$\text{Case}III \qquad S_p = 0.3843n - 0.0002\ , \quad (13)$$

$$\text{Case}IV \qquad S_p = 0.0348n\ , \quad (14)$$

where

S_p= percentage of settlement increment,

n= number of adjacent footings

As it can be seen in Fig. 6, the effect of adjacent footings on settlement is decreased rapidly with increased distance to the main footing, and there is no effect with a distance larger than 3B on the settlement.

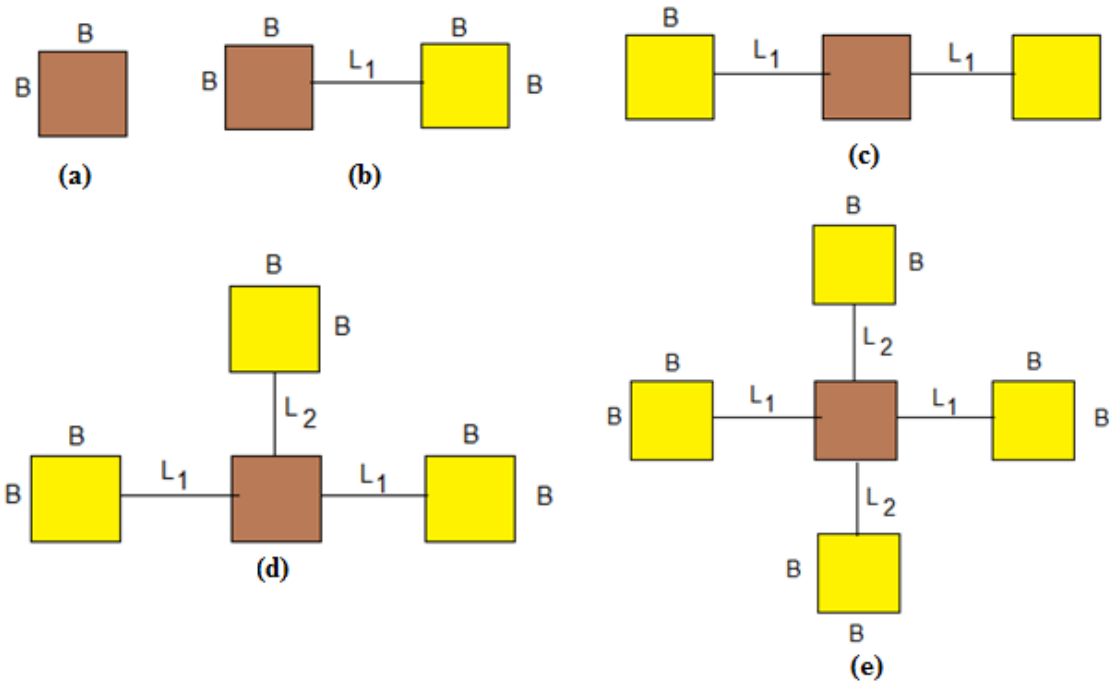

Fig. 3. Configuration of multiple footing arrangements.

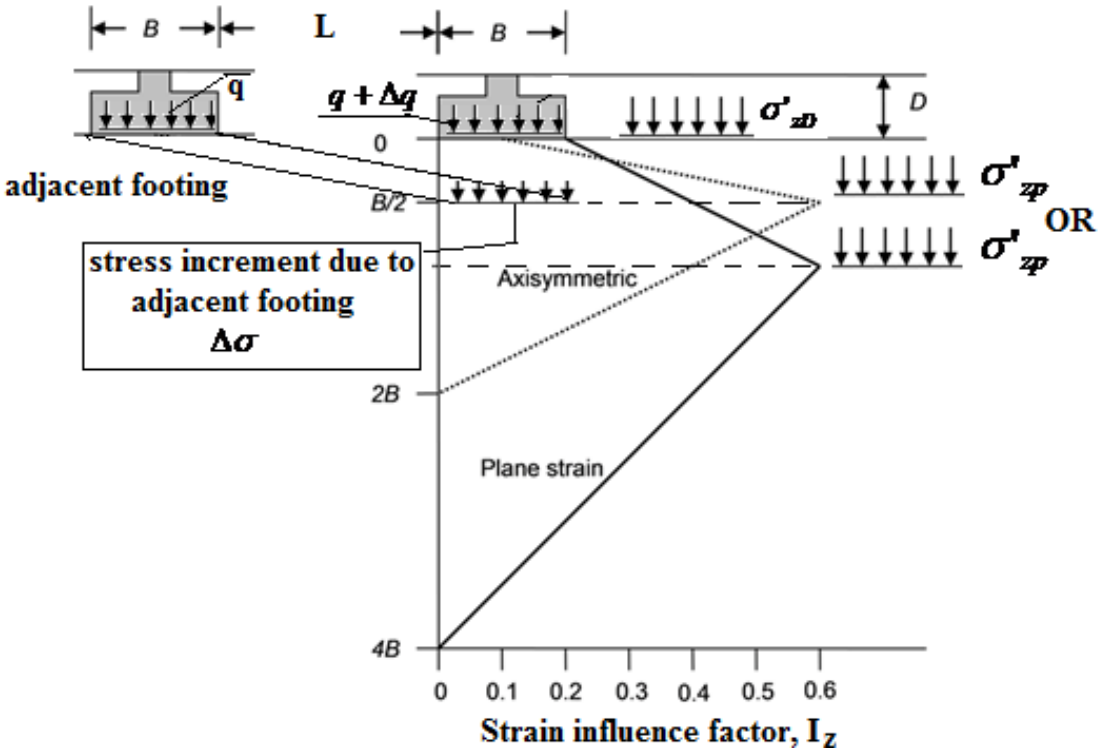

Fig. 4. Stress increment due to adjacent footing under the main footing.

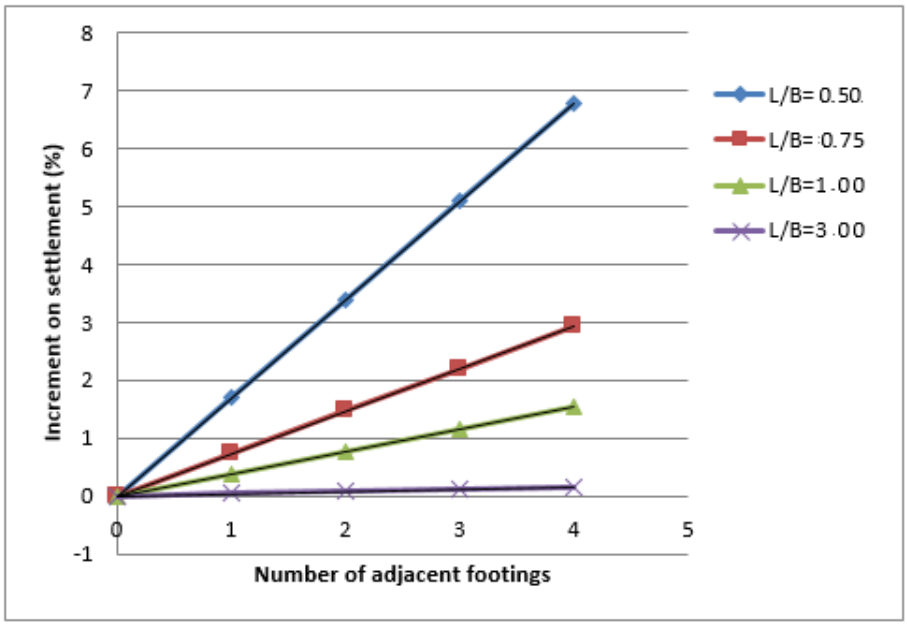

Fig. 5. Increment ratio versus number of adjacent footings.

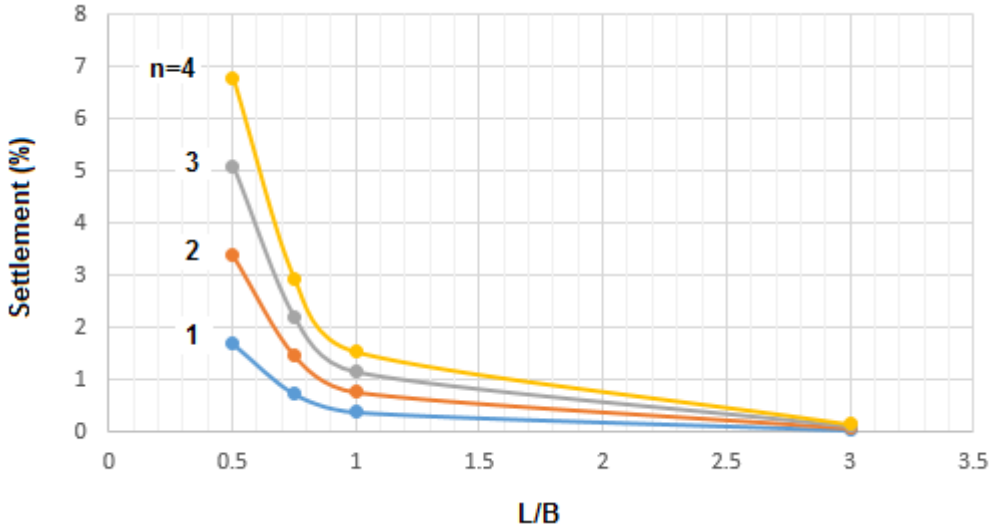

Fig. 6. Variation of settlement (%) versus ratio of distance between footings and their widths.

4. Conclusions

In this paper, a method of settlement estimation that takes account of the proximity of adjacent footings is presented based on Schmertmann's method. The following conclusions may be drawn based on the results of this study:

- The settlement of an isolated footing with adjacent footings is always larger than one with no adjacent footing. The effect of adjacent footings on settlement of main footing is increased linearly with the number of adjacent footing.
- The effect of adjacent footings on settlement is decreased more with smaller increment on distance to the main footing, and there is no effect with a distance larger than 3*B* on settlement.
- The derived equations [11 to 14] can be employed to estimate settlement increment of a main footing under the conditions explained in four cases. Also, similar equations can be driven for various conditions.

References

Berardi R, Jamiolkowski M, Lancellotta R (1991). Settlement of shallow foundations in sands selection of stiffness on the basis of penetration resistance, Proceedings of the Congress Sponsored by the Geotechnical Engineering Division of the ASCE, *Geotechnical Special Publication*, 27, 185-200.

Cernica JN (1995). Geotechnical Engineering Foundation Design. John Wiley and Sons Inc., New York.

Coduto DP (2001). Foundation Design Principles and Practices. Second Edition, Prentice Hall, Upper Saddle River, New Jersey.

Das BM (2007). Principles of Foundation Engineering. SI edition, Sixth edition, Cengage Learning, 200 First Stamford Place, Suite 400, Stamford.

Das BM (2010). Principles of Geotechnical Engineering. Seventh edition, Cengage Learning, 200 First Stamford Place, Suite 400, Stamford.

Lee J, Eun J, Prezzi M, Salgado R (2010). Settlement estimation of multiple footings in sands. *2nd International Symposium on Cone Penetration Testing*, CA, USA.

Meyerhof G (1965). Shallow foundation. *Journal of Soil Mechanics and Foundations Division*, 91(SM2), 21-31.

Schmertmann JH (1970). Static cone to compute static settlement over sand. *Journal of Soil Mechanics and Foundations Division*, 96(SM3), 1011-1042.

Schmertmann JH, Hartman JP, Brown PR (1978). Improved strain influence factor diagrams. *Journal of the Geotechnical Engineering Division*, 104(GT8), 1131-1135.

Challenge Journal of Structural Mechanics

Some open issues in the seismic design of bridges to Eurocode 8-2

Stergios A. Mitoulis *

Department of Civil and Environmental Engineering, University of Surrey, Guildford GU2 7XH, United Kingdom

ABSTRACT

This paper summarises the ongoing research on the seismic design of isolated and integral bridges at the University of Surrey. The first part of the paper focuses on the tensile stresses of elastomeric bearings that might be developed under seismic excitations, due to the rotations of the pier cap. The problem is described analytically and a multi-level performance criterion is proposed to limit the tensile stresses on the isolators. The second part of the paper sheds light on the response of integral bridges and the interaction with the backfill soil. A method for the estimation of the equivalent damping ratio of short-span integral bridges is presented to enable the seismic design of short period bridges based on Eurocode 8-2. For long-span integral bridges, a novel isolation scheme is proposed for the abutment. The isolator is a compressible inclusion comprises tyre derived aggregates (TDA) and is placed between the abutment and a mechanically stabilised backfill. The analysis of the isolated abutment showed that the compressible inclusion achieves to decouple the response of the bridge from the backfill. The analyses showed that both the pressures on the abutment and the settlements of the backfill soil were significantly reduced under the thermal and the seismic movements of the abutment. Thus, the proposed decoupling of the bridge from the abutment enables designs of long-span integral bridges based on ductility and reduces both construction and maintenance costs.

ARTICLE INFO

Article history:
Received 8 December 2015
Accepted 1 February 2016

Keywords:
Seismic design
Isolated bridges
Elastomeric bearings
Pier cap
Backfill soil

1. Introduction

Bridges are important infrastructure assets, which are costly to construct and maintain. Integral Abutment Bridges (IABs), which are jointless bridges with piers and/or abutments rigidly connected to the deck, are resilient frame structures that have minimum maintenance requirements, as they do not have bearings or expansion joints. However, integral bridges are expected to respond in an elastic manner (Eurocode 8-2, 2005) when subjected to the design earthquake motion. Hence, the available ductility of the piers is not utilised to reduce the seismic actions. Also, the damping of integral bridges that occurs due to the inelastic behaviour of the backfill (Caltrans, 2013) is not recognised by Eurocode 8-2 as a source of damping. Additionally, in short-span jointless bridges, the kinematic effects in the backfill soil may magnify the displacements of the backfill (Zhang and Makris, 2002) and thus increase the displacements of the deck (Inel et al., 2002; Kotsoglou and Pantazopoulou, 2007; Taskari and Sextos, 2015). In long-span integral systems, the interaction of the bridge with the backfill soil under serviceability or seismic loads causes significant settlements of the backfill soil (Mitoulis et al., 2014), soil densification and ratcheting flow patterns (England and Tsang, 2001), which increase the soil pressures in the long-term (Arockiasamy and Sivakumar, 2005). Hence, the condition of the backfill soil deteriorates in time and it requires maintenance and/or replacement that results in bridge closures and costly downtime.

The aforementioned design challenges of integral systems lead to the wide application of seismically isolated bridges. In isolated bridges, the seismic action is being enhanced by bearings, expansion joints and, in some cases, dampers. The structure is required to exhibit zero-damage under the prescribed seismic action and this is the requirement for all the structural components and especially the bearings, on which the overall bridge

* *Corresponding author*. Tel.: +44-0-1483-68-6654 ; E-mail address: s.mitoulis@surrey.ac.uk (S. A. Mitoulis)
ISSN: 2149-8024 / DOI: http://dx.doi.org/10.20528/cjsmec.2016.02.002

integrity is relied. However, when the bearings are positively connected to the pier and to the deck, they might be exposed to tensile stresses (Mitoulis, 2014), and this possibility increases when the bearings are placed eccentrically with respect the axis of the pier, which is common in Southern Europe where precast beams are used for the erection of the deck. Kumar et al. (2014) recognised the potential of bearing uplift and for this reason developed a bearing model that accounts for the tensile non-linear response of elastomeric bearings under extended or beyond design basis shaking. The load deformation of the isolators under pure tensile loads was described before by Constantinou et al. (2007) and Warn (2006). Yang at el. (2010) tested bearings having a shear modulus G of 0.55 Mpa under pure tensile loads and identified that the bearing exhibit cavitation (Stanton et al., 2008; Dorfmann[1,2] et al., 2000 and 2003; Yura et al., 2001) when the tensile stresses σ_t exceeded 1-2 Mpa or a strain ε_t of 1%, whilst the bearing uplift potential is evident throughout most bridge design codes (AASHTO, 2012; CalTrans, 1999; EN1998-2, 2005; JRA, 2002).

This paper provides improvements and solutions for the aforementioned challenges of isolated and integral bridges designed to Eurocode 8-2. A criterion that defines three levels of the seismic response of bridge bearings subjected to combined shear, rotation and axial loading is presented to limit the tensile loading of the bearings of isolated bridges. For short-period integral bridges, a methodology for the estimation of the equivalent damping ratio will be described based on a previous research (Mitoulis et al, 2015). The paper concludes with the findings of previous studies on integral abutments that are isolated from the backfill soil by novel compressible inclusions of reused waste materials. It is shown that the proposed design enhances the bridge-backfill interaction under serviceability and seismic displacements of the deck and introduces new cost-effective designs for longer and resilient bridge structures.

2. A Stress Criterion for Mitigating Tension in Steel-Reinforced Elastomeric Bearings

The recent research on the response of isolated bridges subjected to longitudinal seismic excitations (Mitoulis, 2014) showed that the governing parameters that define the tensile displacements on the bearings are predominantly the eccentricity e of the bearing with respect the axis of the pier and the relative rotation of the pier cap and deck, i.e. $r_{pc\text{-}d}= r_{pc}\text{-}r_d$, as shown in Fig. 1a and 1b. The following procedure shows how the stresses on the bearing critical edge (see the far edge on Fig. 1b) can be calculated based on the combination of: (a) the pure tensile displacement of the bearing $r_{pc\text{-}d} \bullet$ e, shown in Fig. 1b; (b) the rotation of the bearing $r_{pc\text{-}d}$ shown in Fig. 1d and (c) the shearing of the bearing by a displacement of u_x, shown in Fig. 1c.

2.1. Tensile stresses on the bearings imposed by the pier cap-deck rotations

The $r_{pc\text{-}d}$ induces a net tensile displacement to the isolators, (Fig. 1b) and a net rotation of the bearing, which is equal to $r_{pc\text{-}d}$, as shown in Fig. 1d. Hence, the total tensile displacement of the far edge of the bearing $v_{b,SEIS}^{r_{pc-d}}$ due to $r_{pc\text{-}d}$ is:

$$v_{b,seis}^{r_{pc-d}} = (r_{pc} - r_d) * \left(e + \frac{L}{2}\right) \rightarrow v_{b,seis}^{r_{pc-d}} = r_{pc-d} * \left(e + \frac{L}{2}\right), \quad (1)$$

where L in eq. (1) is the dimension of the isolator in the longitudinal direction. The axial stiffness K_{vb} of a steel-reinforced bearing is given by Kelly and Konstantinidis (2011):

$$K_{vb} = \frac{E_C * A}{\sum t_i}, \quad (2)$$

where E_c and A are the compression modulus and the area of the isolator respectively and Σt_i is the total thickness of the elastomer. The stress $\sigma_{v,t}$ caused by a net tensile strain of $\varepsilon_{v,t}$ is given by the following equation:

$$\sigma_{v,t} = E_C * \varepsilon_{v,t}. \quad (3)$$

For the tensile stress on the far edge of the bearing due to the rotation $r_{pc\text{-}d}$ the following procedure was followed. The flexural stiffness K_{rb} of the isolator is:

$$K_{rb} = \frac{E_c I_{eff}}{\sum t_i} = 0.329 \frac{E_c I}{\sum t_i}, \quad (4)$$

where I and I_{eff} are the moment of inertia of a beam cross-section with the shape of the bearing and the effective moment of inertia correspondingly. The compression modulus E_c' considering incompressibility behavior is:

$$E'c = 6.073 * G * S^2, \quad (5)$$

where G is the shear modulus of the bearings, S is the bearing shape factor and K is the bulk modulus, which is 2000Mpa (Kelly and Konstantinidis, 2011). It is:

$$E_c = \frac{E'_C * K}{E'_C + K}. \quad (6)$$

The stress $\sigma_{v,M}$ at the edge of the isolator due to the rotation of the bearing, which is shown in Fig. 1d , can be estimated based on the following equation:

$$\sigma_{v,M} = \frac{M*(L/2)}{I_{eff}}, \quad (7)$$

where M is the bending moment that causes a rotation $r_{pc\text{-}d}$ to the bearing, L is the longitudinal dimension of the isolator that is equal to the diameter for a circular bearing, and $y=L/2$ the distance of the edge of the bearing from the neutral axis of the bearing, which remains elastic and is symmetric. The strain $\varepsilon_{v,M}$ of the edge of the bearing due to the rotation $r_{pc\text{-}d}$ is:

$$\varepsilon_{v,M} = \frac{r_{pc-d}*(L/2)}{\sum t_i}, \quad (8)$$

which yields:

$$r_{pc-d} = \frac{\varepsilon_{v,M} * \sum t_i}{(L/2)} = \frac{2*\varepsilon_{v,M} * \sum t_i}{L}. \quad (9)$$

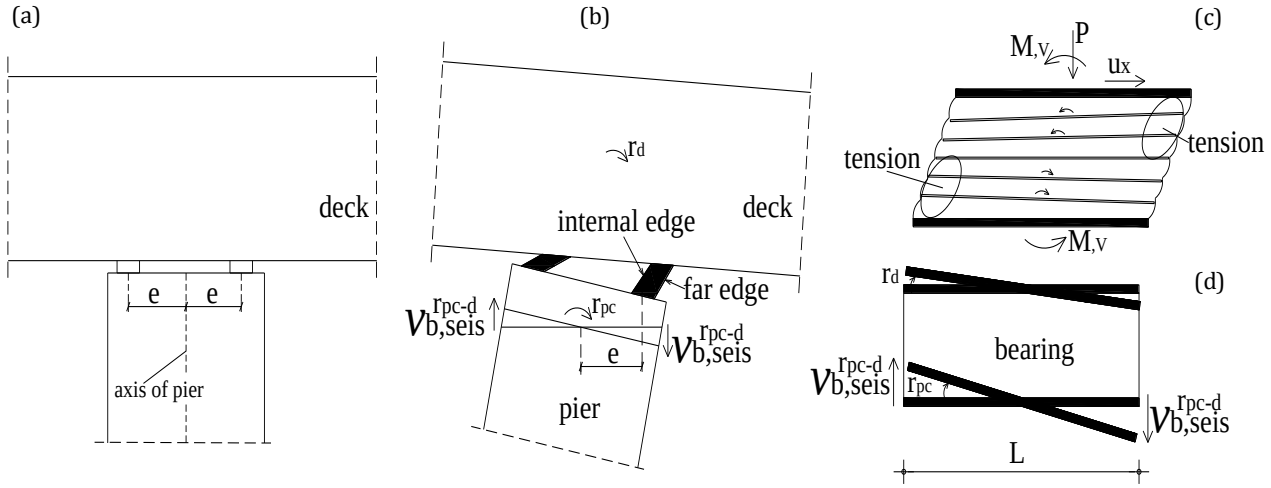

Fig. 1. (a) The geometry of the pier cap; (b) the net tensile displacement of the bearings on the right due to the rotation $r_{pc\text{-}d}$; (c) the tensile stresses under shear strains and; (d) the rotation of the bearing due to the rotation of the pier cap.

Also, the bending moment M of the isolator is:

$$M = K_{rb} * r_{pc-d} \,. \tag{10}$$

Hence, taking into account equation 7 it is:

$$\sigma_{v,M} = \frac{K_{rb} * r_{pc-d} * (L/2)}{I_{eff}} \Longrightarrow \sigma_{v,M} = \frac{K_{rb} * r_{pc-d} * L}{2 * I_{eff}} \,. \tag{11}$$

2.2. Tensile stresses on the bearings due to second order effects

The bending moment due to the shear strain $M_{,v}$, shown in Fig. 1c, also causes tensile stresses to the bearing. The bending moment is:

$$M_{,v} = \frac{P * u_x}{2}, \tag{12}$$

where P is the vertical load acting on the bearing when the bearing is sheared by a displacement of u_x, as shown in Fig1c. Hence, the tensile stress of the far edge of the bearing due to $M_{,v}$ is:

$$\sigma_{v,Mv} = \frac{M_{,v} * (L/2)}{I_{eff}} \longrightarrow \sigma_{v,Mv} = \frac{-P * u_x * L}{4 * I_{eff}}. \tag{13}$$

Notice that P is typically a compressive load (i.e. P<0) that creates tensile stresses, i.e. $\sigma_{v,Mv} \geq 0$.

2.3. Total tensile stresses on the bearings & proposed performance criterion

The maximum strain of the far edge of the bearing $\varepsilon_{b,ULS}^{max}$ is given by Eq. (14):

$$\varepsilon_{b,ULS}^{max} = \varepsilon_{v,t} + \varepsilon_{v,M} + \varepsilon_{v,Mv} + \varepsilon_{b,SLS} \,, \tag{14}$$

where $\varepsilon_{b,SLS}$ is the compressive strain of the bearing due to the self-weight of the deck plus a percentage of the variable loads, i.e. vertical load on the bearing at the onset of the seismic event and $\varepsilon_{v,Mv}$ is the tensile strain due to the $M_{,V}$ Hence, the maximum stress of the far edge of the bearing is:

$$\sigma_{b,ULS}^{max} = \sigma_{v,t} + \sigma_{v,M} + \sigma_{v,Mv} + \sigma_{b,SLS} \leq \sigma_b^{all} = (2\sim3) * G \,, \tag{15}$$

where $\sigma_{b,ULS}^{max}$ and $\sigma_{b,SLS}$ are the maximum tensile stress of the bearing during the seismic event (ULS) and the stress of the bearing that corresponds to the $\varepsilon_{b,SLS}$ respectively. Where, σ_b^{all} is the allowable tensile stress of the bearing. The above inequality assumes that the maximum tensile stress that will be induced on the isolator will be smaller than $\sigma_b^{all} = (2\sim3) * G$. Taking into account Eqs. (3), (11) and (13). Eq. (15) yields:

$$\sigma_{b,ULS}^{max} = E_c * \varepsilon_{v,t} + \frac{K_{rb} * r_{pc-d} * L}{2 * I_{eff}} - \frac{P * u_x * L}{4 * I_{eff}} + \sigma_{b,SLS} \leq \sigma_b^{all} = (2\sim3) * G \,. \tag{16}$$

The tensile strain due to the net tensile displacement $r_{pc\text{-}d} * e$ is:

$$\varepsilon_{v,t} = \frac{r_{pc-d} * e}{\sum t_i}, \tag{17}$$

If we substituted $\varepsilon_{v,t}$ of Eq. (17) in Eq. (16) then we get the maximum allowable stress of the far edge of the bearing as follows:

$$\sigma_{b,ULS}^{max} = E_c * \frac{r_{pc-d}*e}{\sum t_i} + \frac{K_{rb}*r_{pc-d}*L}{2*I_{eff}} - \frac{P*u_x*L}{4*I_{eff}} + \sigma_{b,SLS} \leq \sigma_{b,t}^{all} = (2\sim3) * G\,, \quad (18)$$

or

$$r_{pc-d} \leq \frac{\sigma_{b,t}^{all} - \sigma_{b,SLS} + \frac{P*u_x*L}{4*I_{eff}}}{\frac{E_c*e}{\sum t_i} + \frac{K_{rb}*L}{2*I_{eff}}}. \quad (19)$$

Inequality 19 describes the limit of the relative pier-deck rotation for which the far edge of the bearing under tension (bearing on the right in Figure 1b) will exhibit a maximum tensile stress of $\sigma_b^{all} = (2\sim3) * G$. Notice that force P is compressive, i.e. P<0, and induces a tensile stress at the far edge of the isolator. Also, notice that $\sigma_{b,t}^{all} > 0$ and $\sigma_{b,SLS} < 0$, which means that for the bearing to exhibit a tensile stress during an earthquake equal to, say, $\sigma_{b,ULS}^{max} = 2$ Mpa and the compressive stress of the bearing during SLS is, say, $\sigma_{b,SLS} = -5$ Mpa, the tensile displacements of the bearing due to the rotation of the pier cap and due to the shear displacement u_x should cause stress $\sigma_{b,ULS}^{max} - \sigma_{b,SLS} = 2 - (-5) = 7$ Mpa. If we substituted K_{rb} by Eq. (4) in Eq. (19) we get:

$$r_{pc-d} \leq \frac{\sigma_{b,t}^{all} - \sigma_{b,SLS} + \frac{P*u_x*L}{4*I_{eff}}}{\frac{E_c*e}{\sum t_i} + \frac{E_c*L}{2*\sum t_i}}, \quad (20)$$

Or taking into account eq. 5 and 6 we get:

$$r_{pc-d} \leq \frac{\sigma_{b,t}^{all} - \sigma_{b,SLS} + \frac{P*u_x*L}{4*I_{eff}}}{\frac{E_c}{\sum t_i}*\left(e+\frac{L}{2}\right)} \Rightarrow$$

$$r_{pc-d} \leq \frac{\sigma_{b,t}^{all} - \sigma_{b,SLS} + \frac{P*u_x*L}{4*I_{eff}}}{\frac{1}{\sum t_i}*\left(\frac{6.073*G*S^2*K}{6.073*G*S^2+K}\right)*\left(e+\frac{L}{2}\right)}\,. \quad (21)$$

Notice that it should always be P<0, i.e. the force on the bearing under the maximum shear displacement u_x should be compressive. If P>0 the bearing will be under tension and hence equation 13 would give a misleading result. Hence it should be:

$$P = \left(\sigma_{b,SLS} + \sigma_{v,t}\right) * A \leq 0 \Rightarrow \sigma_{b,SLS} + r_{pc-d} * \frac{E_c*e}{\sum t_i} \leq 0 \Rightarrow$$

$$r_{pc-d} \leq -\frac{\sigma_{b,SLS}*\sum t_i}{E_c*e}\,. \quad (22)$$

Based on Eq. (21) we can define the following criterion that represents the maximum allowable stresses of the bearing during SLS and ULS as follows:

$$\sigma_{b,t}^{all} < 2 * G \qquad for \quad SLS$$

$$2 * G \leq \sigma_{b,t}^{all} \leq 3 * G \qquad for \quad ULS\,. \quad (23)$$

The limits of $2 * G$ and $3 * G$ were selected based upon the literature (EN15129, 2009; Gent, 1990), which suggests that steel-reinforced bearings do not exhibit significant cavitation for stresses smaller than $2 * G$ and this was considered adequate for the SLS design situations. Partial cavitation of the elastomer is acceptable for accidental, i.e. infrequent loads that occurs for stresses $(2\sim3) * G$. Eq. (21) was validated by 3D FE models and it was found that the predicted rotation of the pier cap had a maximum deviation of 6% from the FEM.

3. Seismic Design of Integral Abutment Bridges

3.1. Damping of short-span integral bridges

A methodology is described in a recent paper for the estimation of the equivalent viscous damping ratio of short-span bridges (Mitoulis et al., 2015). The methodology enables the design of integral bridges in Europe as it can be used for performing simplified response spectrum analysis and displacement-based designs of integral bridges. The methodology was applied on a typical integral abutment with representative backfill soil properties. Numerical analyses of the coupled abutment-backfill system were performed with the FE code PLAXIS. Subsequently, the concept of equivalent viscous damping that was first proposed by Jacobsen (1930), to approximate the steady forced vibration response of linear single degree of freedom SDOF damped systems, was employed, and the hysteretic damping ratios were estimated based on the derived force-displacement curves of the coupled system.

It was observed that the abutment exhibited different behaviours for the two loading conditions that are illustrated in Fig. 2, as the abutment is stiffer when it pushes the backfill soil, whereas it is less stiff, when it moves away from it. Interestingly, the hysteretic damping ratios that were estimated for loading condition 2 were higher than the ones that were estimated for the first loading condition for the same target displacement. Also, it was observed that the equivalent damping ratio that was calculated for the bridge of a period of 0.4 sec was approximately 18%, whilst the equivalent damping ratio was found to be approximately 14% for bridges of a period of 0.8 sec. Notably, the above ratios include a 5% damping in the elastic range.

The analysis of equivalent SDOF bridge models, as shown in Fig. 3, showed that the damping is successfully predicted by the proposed method for the long-period - 0.8sec- systems, whilst for short-period systems (0.4 sec) the proposed method underestimates the damping ratio. Also, the proposed method was not able to account for the formation of the voids that are developed between the abutment and the backfill soil, which soften the system abutment-backfill and hence lead to larger displacements. Further analysis will be conducted to develop a model for the damping of integral bridges designed to Eurocode 8-2 that will account for the increased damping that occurs within the yielding backfill.

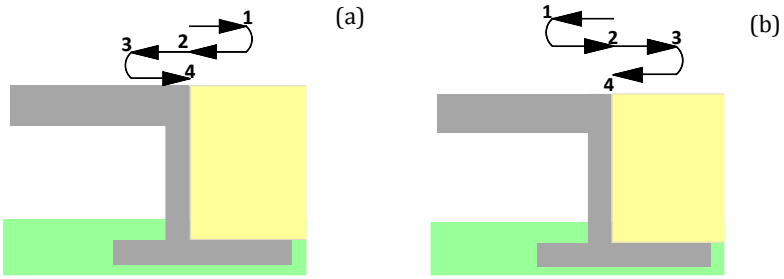

Fig. 2. (a) Loading 1: the abutment first pushes (p_s) the backfill soil and; (b)) loading 2, the abutment first pulls (p_l) the backfill soil.

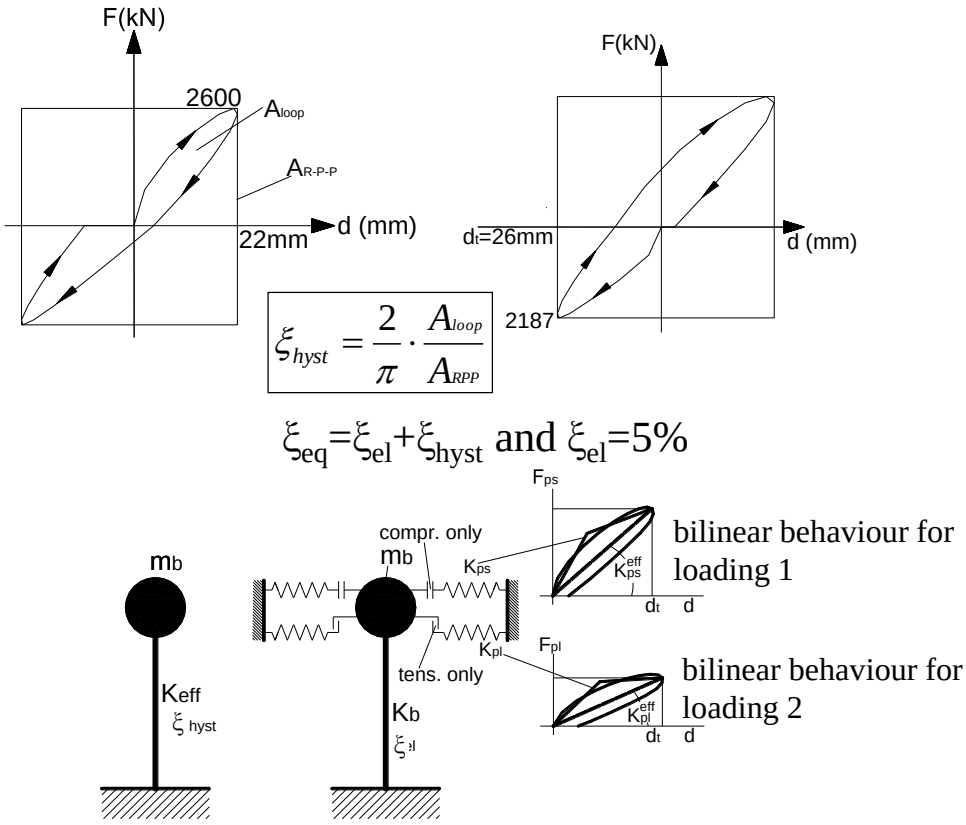

Fig. 3. The F-d curves for the bridge (effective period of 0.4sec & target displacement 25mm) and description of the linear and non-linear SDOF models of integral bridges.

3.2. Enhancing the response of long-span integral bridges

An isolation scheme is proposed for integral abutments to mitigate the adverse coupling of the bridge with the backfill soil under serviceability and seismic displacements, as shown in Fig. 4. The proposed isolation enables the design of longer maintenance-free bridges. For this purpose, novel compressible inclusions of reused tyre derived aggregates were studied and applied in numerical models of integral abutments with mechanically stabilised backfills. The properties of the compressible inclusions were defined by laboratory tests. An ad-hoc uniaxial test apparatus was produced for this purpose at the Laboratory of Strength of Materials at the University of Surrey.

Model compressible inclusions were tested under cyclic compressive strains, which correspond to realistic strains that are imposed to the inclusion by the movements of the integral abutment. The Young's modulus, the permanent deformations and the behaviour of the compressible inclusion was defined under the repetitive loads, strictly for the design purposes of this study. The experimental results were validated with the triaxial tests conducted in Aristotle University of Thessaloniki.

Subsequently, typical integral abutments were modelled and numerical analysis by 2D nonlinear FE model in Plaxis was conducted for bridges with or without compressible inclusions. The validation of the static and dynamic response of the model abutments was presented in a previous paper (Argyroudis et al, 2013). The settlements of the backfill and the soil pressures on the abutment were evaluated for bridges with and without compressible inclusions to assess the efficiency of the compressible inclusion. Fig. 5a and b show the settlements and the soil pressures for the conventional and the proposed integral abutment, with the compressible inclusion. The Figures are indicative as they show the results for one seismic motion only, which was scaled to a peak ground acceleration of 0.3g. It is shown that the use of isolators of tyre derived aggregates can enhance the bridge-backfill interaction by reducing significantly the settlements, as shown in Fig. 5a, and the pressures on the abutment, as shown in Fig. 5b. Therefore, the isolation of the abutment from the backfill soil is key to the application of long-span integral bridges. Also, it was observed that the bridge, which had its abutments isolated from the backfill soil, exhibited displacements which were significantly larger than the conventional integral bridge. Hence, the available ductility of the piers of integral bridges can be utilised as a means to reduce the seismic actions of this type of bridges, i.e. a behaviour factor larger than one proposed by Eurocode 8-2 can be used.

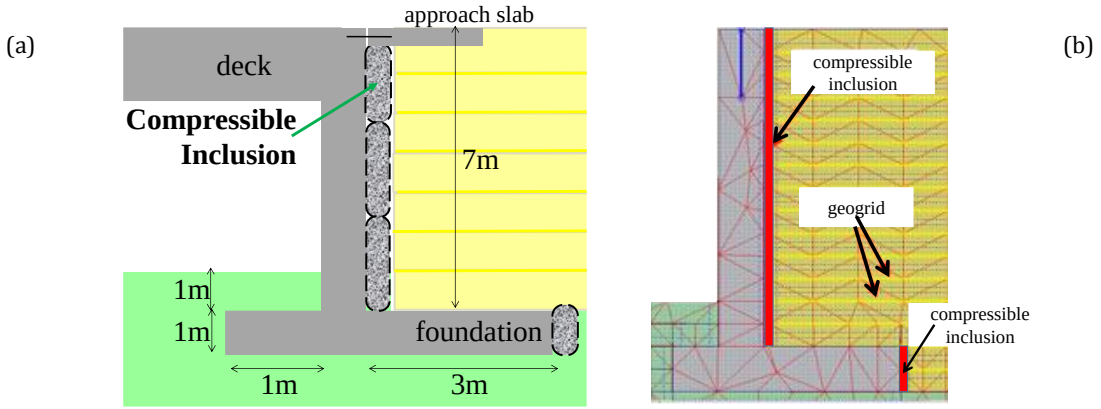

Fig. 4. (a) The isolation of the abutment with compressible inclusions and; (b) the 2D FE model that was analysed in PLAXIS.

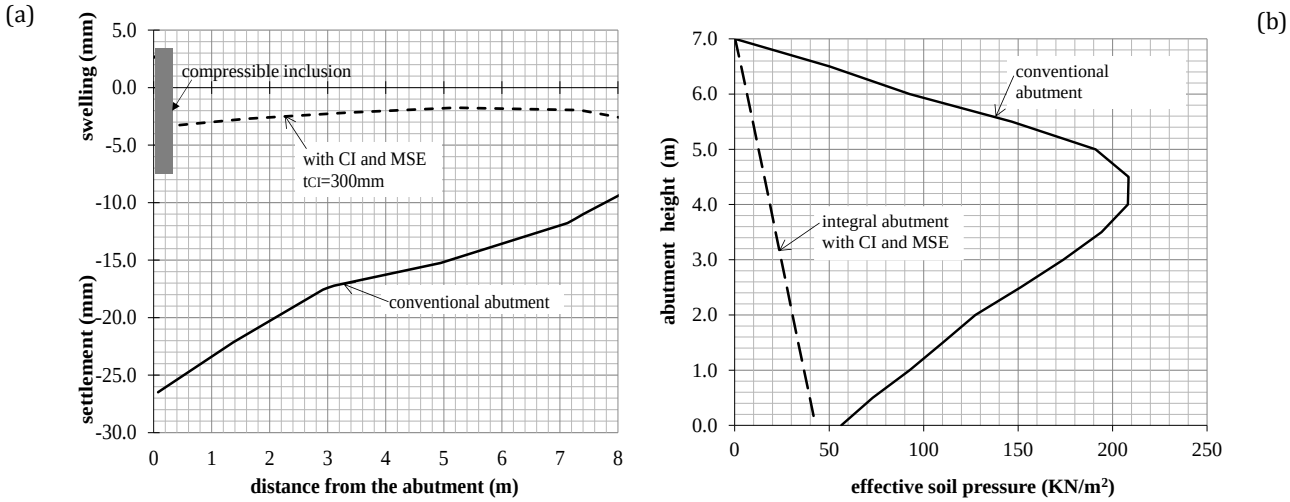

Fig. 5. (a) The swelling and the settlements of the backfill soil for integral abutments with and without compressible inclusions and; (b) the soil pressures on the abutment (indicative).

4. Conclusions

A synopsis of the research that is being conducted at the University of Surrey on earthquake resistant bridges was presented. Open issues on the design of seismically isolated and integral bridges were presented and solutions were proposed. The main outcomes of the research are summarised below:

The design of seismically isolated bridges with bearings eccentrically placed on the pier cap, which is common practice in Southern European countries, is required to account for potential tensile loading in the bearings. A stress-based criterion was described in this paper. The criterion was developed by applying elastic beam theory and defined the maximum tensile stresses at the critical edge of the bearing. The analytical model was validated through a FE model of a single-pier with

steel-reinforced bridge bearings. The criterion suggests three levels of bearing tensile stresses that represent SLS (no cavitation), ULS (potential of cavitation) and extensive cavitation of the elastomer of the isolator. The bounds of the aforementioned stress criterion were decided upon the international literature, the available laboratory tests and the current Eurocode provisions. The proposed criterion can be useful for limiting the rotation of the piers for different bridge types and for bearings placed either concentrically or eccentrically with respect the pier cap. This criterion was found to predict with acceptable accuracy the maximum tensile stress of the critical edge of the bearing.

The seismic response and design of integral abutment bridges to Eurocode 8-2 was discussed for both short- and long-span systems. For the short period integral bridges, the ongoing research on the estimation of the damping ratio of bridges is discussed based upon a previous paper. The studies to date resulted in equivalent damping ratios higher than the ones prescribed by Eurocode 8-2. Further verification of the numerical studies will be conducted with the aim to develop a model for the estimation of the equivalent damping ratio of integral bridges to simplify the analysis and design of this particular type of bridges in Europe.

A novel solution for long-span frame bridges was presented. The experimental and numerical studies conducted in collaboration with Aristotle University of Thessaloniki concluded that the isolation of integral abutments from the backfill soil by means of ad-hoc compressible inclusions, enables the design of longer and ductile integral bridges. Additionally, the isolation of the bridge by means of reused tyre derived aggregates enhances the long-term performance of the system as both the settlements of the backfill and the soil pressures on the abutment are significantly reduced.

REFERENCES

AASHTO (2012). LRFD Bridge Design Specifications. 6th ed., American Association of State Highway and Transportation Officials, with 2013 interim revisions. Washington, DC.

Argyroudis SA, Mitoulis SA, Pitilakis KD (2013). Seismic response of bridge abutments on surface foundation subjected to collision forces. *COMPDYN 4th International Conference in Computational Methods in Structural Dynamics and Earthquake Engineering*, Kos, Greece.

Arockiasamy M, Sivakumar M (2005). Time-dependent behavior of continuous composite integral abutment bridges. *Practice Periodical on Structural Design and Construction*, 10(3), 161–170.

California Department of Transportation [CalTrans] (1999). Bridge memo to designers (20-1) – Seismic design methodology. Sacramento, CA.

California Department of Transportation [CalTrans] (2013). Seismic design criteria, Version 1.7.

Constantinou MC, Whittaker AS, Kalpakidis Y, Fenz DM, Warn GP (2007). Performance of Seismic Isolation Hardware Under Service and Seismic Loading. Report 07-0012, MCEER, Buffalo, New York.

Dorfmann A, Burtscher SL (2000). Aspects of cavitation damage in seismic bearings. *Journal of Structural Engineering*, 126, 573-579.

Dorfmann A (2003). Stress softening of elastomers in hydrostatic tension. *Acta Mechanica*, 165(3), 117-137.

EN 1337-3 (2005). Structural bearings – Part 3: Elastomeric bearings.

EN 15129 (2009). Anti-seismic devices. BSI British Standards.

EN 1998-2 (2005). Eurocode 8: Design of structures for earthquake resistance, Part 2: Bridges.

England GL, Tsang NC (2001). Towards the design of soil loading for integral bridges-experimental evaluation. Department of Civil and Environmental Engineering, Imperial College, London.

Gent A (1990). Cavitation in rubber: a cautionary tale. *Rubber Chemistry and Technology*, 63(3), 49-53.

Iemura H, Taghikhany T, Takahashi Y, Jain S (2005). Effect of variation of normal force on seismic performance of resilient sliding isolation systems in highway bridges, Earthquake Engineering and Structural Dynamics, 34, 1777-1797.

Inel M, Aschheim M (2004). Seismic design of columns of short bridges accounting for embankment flexibility. *Journal of Structural Engineering*, 130(10), 1515–1528.

Jacobsen LS (1930). Steady forced vibrations as influenced by damping. *Transactions of the American Society of Mechanical Engineers*, 52, 169-181.

Japan Road Association (1997). Manual for seismic design of highway bridges. Tokyo.

Kelly JM, Konstantinidis DA (2011). Mechanics of Rubber Bearings for Seismic and Vibration Isolation. JohnWiley & Sons Ltd.

Kotsoglou A, Pantazopoulou S (2007). Bridge–embankment interaction under transverse ground excitation. *Earthquake Engineering & Structural Dynamics*, 36(12), 1719–1740.

Kumar M, Whittaker AS, Constantinou MC (2014). An advanced numerical model of elastomeric seismic isolation bearings. *Earthquake Engineering and Structural Dynamics*, 43, 1955-1974.

Mitoulis SA (2014). Uplift of elastomeric bearings in isolated bridges subjected to longitudinal seismic excitations. *Structure and Infrastructure Engineering*, 11(12), 1600-1615.

Mitoulis SA, Argyroudis S, Pitilakis KD (2014). Green rubberised backfills to enhance the longevity of integral abutment bridges. *15th European Conference On Earthquake Engineering*, Istanbul.

Mitoulis SA, Muhr A, Ahmadi H (2014). Uplift of elastomeric bearings in isolated bridges-A possible mechanism: Effects and remediation. *Proceedings of the 15th European conference on earthquake engineering*, Istanbul.

Mitoulis SA, Argyroudis S, Kowalsky M (2015). Evaluation of the stiffness and damping of abutments to extend DDBD to the design of integral bridges. *COMPDYN 2015, 5th ECCOMAS Thematic Conference on Computational Methods in Structural Dynamics and Earthquake Engineering*, Crete.

Stanton JF, Roeder CW, Mackenzie-Helnwein P, White C, Kuester C and Craig B (2008). Rotation limits for elastomeric bearing. *National Cooperative Highway Research Program Report No. 596,* Trans. Research Board, National Academy Press, Washington, D.C.

Taskari O, Sextos A (2015). Probabilistic assessment of abutment-embankment stiffness and implications in the predicted performance of short bridges. *Journal of Earthquake Engineering*, 19(5), 822-846.

Warn GP (2006). The coupled horizontal-vertical response of elastomeric and lead-rubber seismic isolation bearings. *Ph.D. thesis*, University at Buffalo.

Yang QR, Liu WG, He WF, Feng DM (2010). Tensile stiffness and deformation model of rubber isolators in tension and tension-shear states, *Journal of Engineering Mechanics*, 136, 429-437.

Yura J, Kumar A, Yakut A, Topkaya C, Collingwood E (2001). Elastomeric bridge bearings: Recommended test methods. *National Cooperative Highway Research Program Report No. 449*, Trans. Research Board, National Academy Press, Washington, D.C.

Zhang J, Makris N (2002). Kinematic response functions and dynamic stiffnesses of bridge embankments. *Earthquake Engineering Structural Dynamics,* 31, 1933–1966.

Challenge Journal of Structural Mechanics

Design procedure for ductile tension-only seismic bracing with an energy dissipation ring

Dejan Erdevicki *

Erdevicki Structural Engineering, 4205 Musqueam Drive, Vancouver V6N 3R8, Canada

ABSTRACT

This paper will present a design solution for a ductile, tension–only seismic bracing with the use of an energy dissipating ring. This type of bracing behaves very well under seismic loading and has shown, by testing carried out in conjunction with the University of British Columbia, that it can reach very high post elastic drift limits. The presented procedure is a method created by the author and is based on information collected during the research testing program performed by the Civil Engineering Department at the University of British Columbia. The team was led by Professor Carlos Ventura, in collaboration with Dejan Erdevicki from Erdevicki Structural Engineering. The presented design procedure describes the behaviour of the system, the relation between energy, forces, drift limits and capacities of the ring. It also includes geometrical limitations and requirements for the ring element and bracing system, to ensure that target drifts can be achieved. It allows the user to calculate seismic forces and reduction factors based on an energy criterion and the chosen final drift of the structure. For longer period structures, an equal displacement principle was discussed and considered. The procedure can be used for seismic capacity design and is easily adjusted to suit applicable national codes. Ring capacity tables and examples are also included. This ductile, tension–only bracing, with an energy dissipating ring, can be used for new structures, as well as for the retrofit of existing ones. The system is relatively simple and allows for easy replacement of the ring after an earthquake event if needed. The application of the bracing system for buildings, including multi-storey structures, will be discussed.

ARTICLE INFO

Article history:
Received 8 December 2015
Accepted 12 February 2016

Keywords:
Seismic bracing
Energy dissipation ring
Drift limit
Seismic design
Multi-storey structures

1. Introduction

The tension–only bracing illustrated in Fig. 1 is a simple and ductile bracing system that can be used as a seismic load-resisting structural element. The design procedure presented in this paper is a conservative method created by the author, based on the information collected during a series of tests on a full-scale braced frame carried out at the University of British Columbia. The testing program included quasi-static, cyclic and shake-table tests. Work on this research project started 2007 and most of the tests were performed from 2011 to 2013. The test program was performed at the UBC Earthquake Engineering Laboratory by a research team led by Professor Carlos Ventura, in collaboration with Dejan Erdevicki from Erdevicki Structural Engineering.

The test program was limited to 45 degree diagonals and one-story bracing. The author is confident that the procedure can be used also for multi-story bracing systems. The optimal angle for diagonals is 45°. Until further test results are conducted, the author recommends restricting the angle of diagonal bracing α to between 40° and 50°.

The system will dissipate energy by forming plastic hinges inside the central ring. Control of the number of hinging points and their locations is achieved using clamp plates. The design procedure presented in this paper is valid only if all the requirements for the ring and system design described below are fulfilled.

* *Corresponding author*. Tel.: +1-604-880-1720 ; E-mail address: erdevicki@telus.net (D. Erdevicki)
ISSN: 2149-8024 / DOI: http://dx.doi.org/10.20528/cjsmec.2016.02.003

Nomenclature

A	length of clamp plates, mm
A_{eq}	effective rod cross sectional area, mm^2
A_r	rod cross sectional area, mm^2
B	width of ring, mm
C	dimension between clamp plates, mm
D_{eq}	equivalent diameter of rod, mm
D_i	internal diameter of ring, mm
D_o	external diameter of ring, mm
E	modulus of elasticity of steel, MPa
F_u	tensile strength of ring material, MPa
F_y	yield strength of ring material, MPa
H	horizontal force, kN
H_{el}	elastic seismic horizontal force, kN
H_{ov}	overstrength horizontal force, kN
H_y	horizontal force causing yield, kN
h	height of braced frame, mm
h_i	height of ith floor in multi-storey frame, mm
K	initial elastic stiffness of bracing, kN/mm
K_r	elastic stiffness of ring, N/mm
L_d	length of diagonal, mm
M_f	factored bending moment at a section, kNmm
$M_{f\ wind}$	factored bending moment for wind at a section, kNmm
M_r	seismic flexural resistance at a section, kNmm
M_{rw}	factored flexural resistance for wind at a section, kNmm
R_0	material factor as specified in the applicable design code
R_d	ductility factor as described in Section 6
T_1	first natural period of vibration, sec
t_r	thickness of ring, mm
t_w	clamp plate thickness, mm
X, Y	sections of peak ring flexure
Z	diagonal force, kN
Z_{el}	elastic seismic rod tension force, kN
Z_f	factored rod tension force, kN
$Z_{f\ wind}$	factored rod wind force, kN
Z_r	ring factored tension resistance, kN
$Z_{r\ wind}$	ring factored tension wind resistance, kN
Z_y	ring yield tension capacity, kN
δ	horizontal deformation corresponding to H
δ_{el}	elastic horizontal deformation
δ_{max}	maximum horizontal deformation
δ_y	horizontal deformation causing yield
Φ	hole diameter, mm

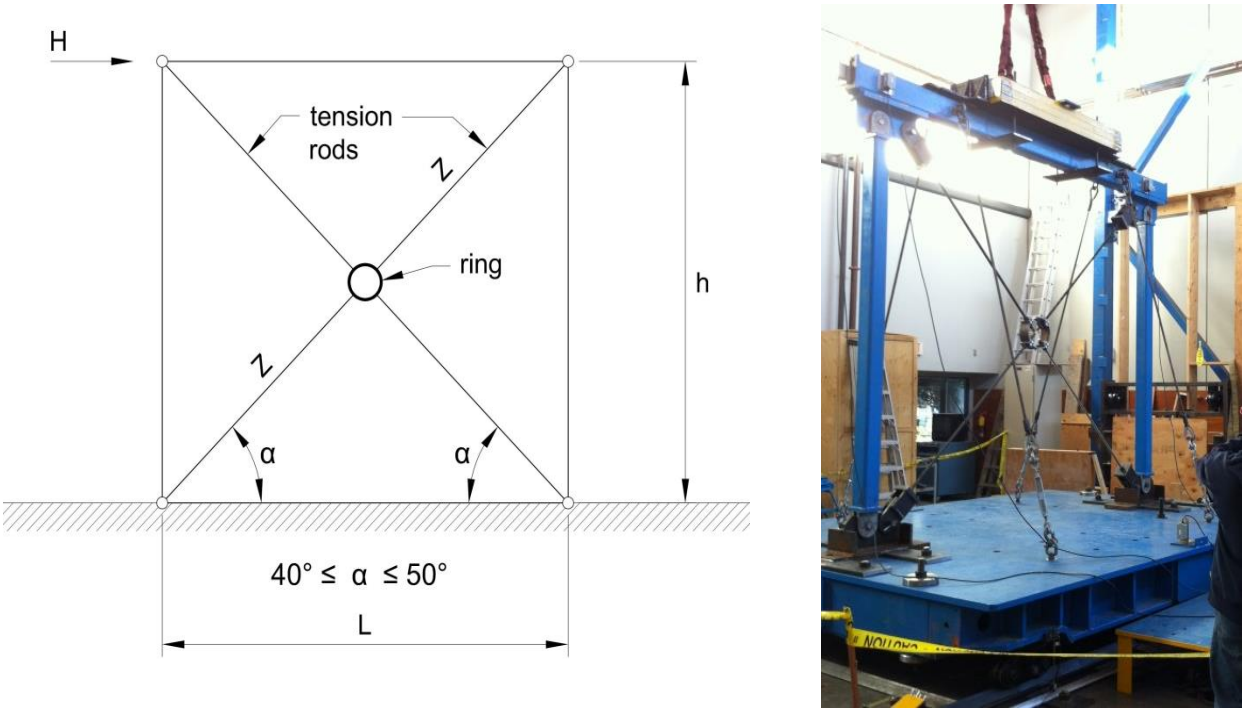

Fig. 1. Bracing system.

2. Ring General Requirements

The ring and washers are generally as shown in Fig. 2.

Based on current testing following geometric requirements are suggested:

- $Di > 142 > h / 21$
- $tr \geqslant 7$
- $B > 90 > 4 * \Phi$

The minimum tested inside ring diameter *Di* was 149 mm for a frame height of 3160 mm ($h / Di = 21.2$). Larger rings performed better as the post-elastic frame deformation for all quasi-static tests was limited to the same drift of $0.015 * h$. For that reason it is suggested that $Di > h / 21$ and $Di > 142$ mm. All tested rings were 90 mm wide and had 22 mm holes ($B / \Phi = 4.1$). The suggested B / Φ ratio is to limit the ring net-section reduction.

When tested, rings without double clamp plates fractured at the hole locations, whereas rings with double clamp plates fractured at the edges of the clamp plates and performed much better in the tests. All tested clamp plates were 50 mm long, 19 mm thick and had 22 mm diameter holes. These clamp plates worked well for overstrength diagonal loading of about 110 kN.

Making the clamp plates too narrow or too thin will reduce the clamp plate capacity and would impair ring performance. The clamp plates should remain elastic in resisting overstrength loading and should be capable of distributing the load evenly across the width of the ring. In addition, the clamp plates should not be too long in order to maximize the post-elastic deformation capacity of the rings. The minimum Di / A ratio tested was 2.98. The proposed Di / A ratio are therefore >3.0.

The following geometric limits are proposed, but could be varied in the light of satisfactory test results:

- $A \leqslant Di / 3, \geqslant 50, \geqslant 2 *$ rod diameter, $\geqslant Do / 6$
- $tw > 19, > B / 5, > 0.4 * A, > 1.25 * tr$
- Clamp plate radius to match inside and outside ring radius.
- Clamp plate corners to be chamfered 2-3 mm.
- Clamp plate material to be as strong, or stronger than the ring material.
- Ring and clamp plate holes are to be 2 mm larger than the rod diameter.
- Rod nuts and lock washers to be placed on the inside and outside of the ring.

3. Ring Capacity, Factored Loading and Overstrength Factor

The following simplified relationship between the rod tension force and ring moments can be used:

$Mf = 0.3 * Zf * C$ or $Zf = Mf / (0.3 * C)$ Eq. (4.1)

where

$C = (Do - tr) / 2 - A / 2 + 5$ mm

Numerical modeling of the ring and clamp plates would be another way to determine the maximum moment at Section X.

3.1. Non-seismic loading

For non-seismic loading, the ring bending resistance at Section X should be calculated based on the applicable steel design code, using the gross section $B * tr$ without reduction for the hole. The suggested ULS stress limit is $0.9 * Fy$.

The capacity check at Section Y is not critical, as the section tension capacity is significantly larger than the corresponding moment capacity, and the initial moment at Section Y is only about 67% of the corresponding moment at Section X.

3.2. Seismic loading combinations

For seismic design, the following ring resistance can be used:

- $Mr = My = 1 / 6 * Fy * B * tr^2$ and $Zr = Zy = Mr / (0.3 * C) = 1/6 * Fy * B * tr^2 / (0.3 * C)$ Eq. (4.2)
- The seismic design requirement will be:
- $Mr \geqslant Mf$ or $Zr \geqslant Zf$
- Mf can be calculated using the design factored tension rod force $Zf = Zel / (Rd * R0)$.
- Zel = elastic diagonal ULS seismic force corresponding to Hel calculated using the applicable building code.
- $\leqslant Ro \leqslant 1.5$, $Ro = 1.5$ is recommended.

The overstrength ring capacity will exceed the tensile strength of the material, Fu and the ring will gain significant post-elastic capacity through shape change. Based on experimental results, the maximum ring overstrength could be between 2.0 and 2.5. The author suggests using an overstrength factor of 2.5 for design of all connections, tension rods, and affected structural bracing elements and foundations. The overstrength factor for rings larger than 210 mm could be reduced to 2.0.

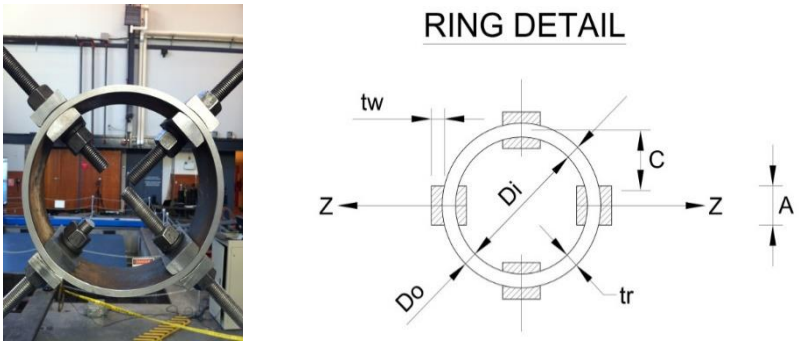

Fig. 2. Ring geometry

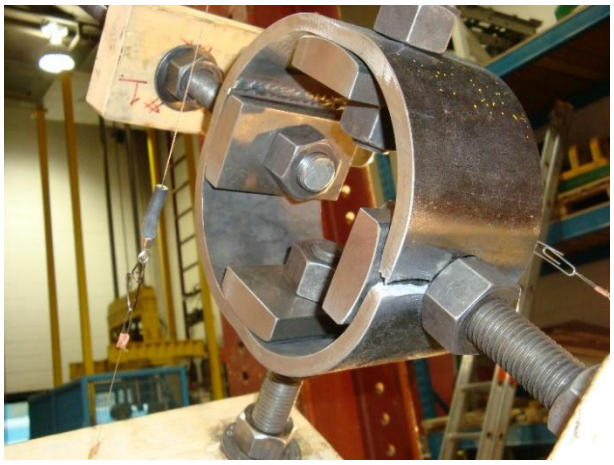

Fig. 3. Ring without double clamp plates.

Fig. 4. Ring with double clamp plates.

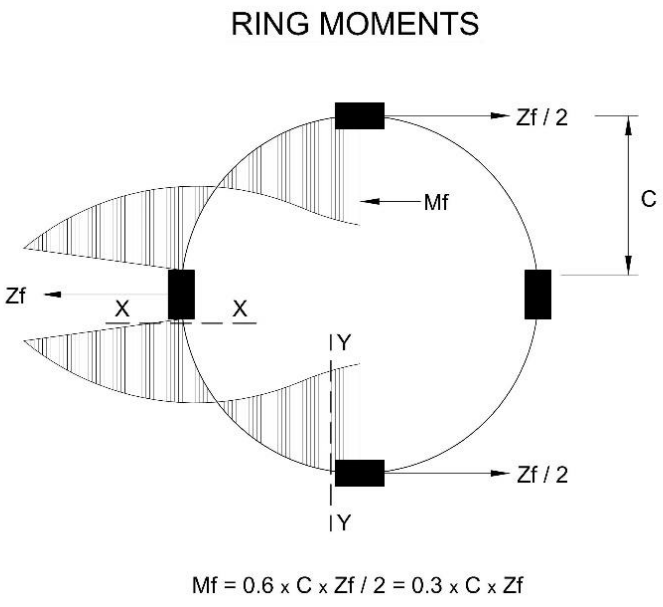

Fig. 5. Ring moments.

3.3. Example and capacity table

Table 1. Ring capacity table.

Ring	*Do* (mm)	*tr* (mm)	*B* (mm)	*Fy* (Mpa)	*A* (mm)	Seismic Capacity *Zr* (kN)
168/8	168	8	100	350	50	21
168/9.5	168	9.5	100	350	50	30
168/11	168	11	100	350	50	40
168/13	168	12.7	100	350	50	54.5
219/8	219	8	100	350	50	14.5
219/9.5	219	9.5	100	350	50	20.5
219/11	219	11	100	350	50	28
219/13	219	12.7	100	350	50	37.5
219/16	219	16	100	350	50	61
219/22	219	22	100	350	50	120
219/25	219	25.4	100	350	50	163
273/8	273	8	100	350	60	11.5
273/9.5	273	9.5	100	350	60	16.5
273/11	273	11	100	350	60	22
273/13	273	12.7	100	350	60	30
273/16	273	16	100	350	60	48
273/22	273	22	100	350	60	94
273/25	273	25.4	100	350	60	127
324/11	324	11	100	350	60	18
324/13	324	12.7	100	350	60	24
324/16	324	16	100	350	60	38.5
324/22	324	22	100	350	60	75
324/25	324	25.4	100	350	60	101
356/13	356	12.7	100	350	75	22.5
356/16	356	16	100	350	75	36
356/22	356	22	100	350	75	70
356/25	356	25.4	100	350	75	94.5

4. Bracing Stiffness

The initial elastic bracing stiffness $K = H / \delta$.

The bracing stiffness is important in estimating the ductility factor *Rd* and should therefore be carefully determined. The bracing should be modeled with one diagonal only and should include the ring.

Alternatively, the ring stiffness *Kr* from Table T2 can be used to calculate the required effective diagonal cross sectional area *Aeq* and to model only the diagonal without the ring using *Aeq*.

$$Aeq = Ar * Ld / (A\,r * E / Kr + Ld - Do) \quad \text{Eq. (5.1)}$$

Example:

- *Ld* = 4500 mm
- *Ar* = 380 mm2 (for 22 mm diameter rod)
- Ring size: 324/25.4
- *Kr* = 55 kN/mm (from Table T2) = 55 000 N/mm
- *E* = 210 000 MPa
- Required equivalent diagonal cross section:
- *Aeq* = 380 * 4500 / (380 * 210000 / 55000 + 4500 - 324)
- *Aeq* = 303 mm2

Or, equivalent rod diameter *Deq* = 19.7 mm.

The bracing should be modeled with one diagonal rod using an equivalent rod diameter of 19.7 mm.

The ring stiffness *Kr* for thicknesses not listed in Table T2 could be estimated using a ring of the same diameter and adjusting the stiffness using the tr^3 ratio.

Example:

For the 219/16 ring, a thinner ring with the same diameter, 219/13 will be used. For the 219/13 ring, from Table T2, *Kr* = 24 kN/mm. Therefore, for the 273/16 ring, $Kr = 24 * 16^3 / 13^3 = 44.7$ kN/mm.

If the designer wishes to increase the bracing stiffness or capacity, it can be done by increasing the rod diameter, or by using multiple rods as shown in Fig. 8, in which case the ring should satisfy the geometric requirements described in Section 3.

5. Energy and RD

5.1. Systems with the first period of oscillation T1 < 0.5(s)

An energy criterion will be used to establish the ductility factor *Rd* as shown in Fig. 9. Test results have verified that diagonal tension-only bracing with a central ring can reach a post-elastic drift limit of at least 1.5 %. In addition, it was also evident that the system overstrength factor is higher than the *Fu* / *Fy* ratio. The overstrength area ΔE1 is larger than the area ΔE2 for $\delta y <$ 0.0075 h, and is used to compensate for the ΔE2 area, and allow for simplification of the formula for E1 shown in Fig. 9.

As a result: $Rd = 2 * K * \delta max / Hel$ Eq. (6.1)

Substituting *Hel* / *δe*l for *K*: $Rd = 2 * \delta max / \delta el$ Eq. (6.2)

Hel = The elastic seismic force calculated using the applicable building code

δel = elastic force displacement

δmax = 0.015 * h = maximum displacement limit

Suggested Rd Limits:

$2.0 \leqslant Rd \leqslant 5.0$

It is important to note that the *Rd* factor can be increased using higher stiffness *K*, and will be reduced for a higher elastic force.

Example:

- *Hel* = 100 kN
- *K* = 5 kN/mm
- *h* = 3000 mm
- *δmax* = 0.015 * 3000 = 45 mm
- *Rd* = 2 * 5 * 45 / 100 = 4.5
- Or using *Rd* = 2 * *δmax* / *δel*
- *δel* = 20 mm
- *Rd* = 2 * 45 / 20 = 4.5

Therefore, if the system is properly modelled and the elastic seismic forces are applied, the factor *Rd* is the ratio between the maximum chosen displacement and the elastic displacement.

5.2. Systems with a first period of oscillation T1>0.5(s)

The generally accepted the equal displacement principle shown in Fig. 10 can be used as an alternative to the previously described approach. Further testing will be required to verify that the equal displacement principle is adequate and to establish a realistic limit to the force reduction factor.

An important limitation of the system in this case is that the elastic force displacement *δel* must be <0.015 * *h*. If the designer decides to use the equal displacement approach, the author suggests limiting the force reduction factor *Rd* to 5.0.

5.3. Multi-storey systems

The force reduction factor, *Rd* can be checked at each storey level using the elastic seismic shear force at that level and corresponding *K* and *δmax* = 0.015 * *hi* at that level. *Rd* can also be determined by calculating the elastic displacements at each level and using Eq. (6.2). See Fig. 11 for more details.

Ring ductility should be used at each floor level and should be designed with respect to design seismic shear force at that level. Further research should be undertaken on the behaviours of the multi-storey system to ensure that the plastic behaviour is not concentrated at the lower storey, but is distributed throughout.

6. Design Procedure for Systems with T1 < 0.5 s

- Design the ring and bracing for non-seismic loading.
- Calculate the first period T1, and system stiffness, K.
- Calculate the elastic seismic force Hel based on the applicable design code.
- Calculate Rd as described in Section 6.
- Calculate the seismic design force *Hf* = *Hel* / (*Rd* * *Ro*).
- Calculate the corresponding diagonal force *Zf.*
- Design the ring as described in Section 4.
- Check the stiffness *K* based on the chosen ring size, and if K is lower than initially assumed, repeat the above procedure. If the chosen ring is stiffer than initially assumed, the system is safe in the case that it does not affect the force *Hel*. The designer can elect to refine the design or not.
- Design tension rods, connections and all affected bracing and foundation elements for overstrength forces *Hov* = 2.5 * *Hy* (2.0 * *Hy* for rings > 210 diameter) but *Hov* < *Hel* / *Ro*.

7. Design Procedure for Systems with T1>0.5 (s) using Equal Displacement Principle

- Design the ring and bracing for non-seismic loading.
- Calculate the first period T1 and system Stiffness *K*.
- Calculate the elastic seismic force Hel based on the applicable design code.
- Assume *Rd* = 5.
- Calculate the seismic design force *Hf* = *Hel* / (*Rd* * *Ro*).
- Calculate the corresponding diagonal force *Zf.*
- Design the ring as described in Section 4.
- Check T1 and *K* based on the chosen ring size.
- *K* must be larger than *Kmin* = *Hel* / *δmax*.
- If T1 is higher than initially calculated, the designer can elect to refine the design or not.

Design the tension rods, connections and all affected bracing and foundation elements for overstrength forces *Hov* = 2.5 * *Hy* (2.0 * *Hy* for rings > 210 diameter) but *Hov* < *Hel* / *Ro*.

8. Installation

It is very important to install the ring exactly at the theoretical diagonal intersection point. A test performed on one braced frame with a ring 100 mm off-centre showed degradation of the hysteresis loops and pinching behaviour. Lock washers should be used. Slight pre-tensioning of the diagonal rods from the snug tight position is recommended. If higher capacity or stiffness is needed, wider rings with multiple diagonal rods as shown in Fig. 8 can be used.

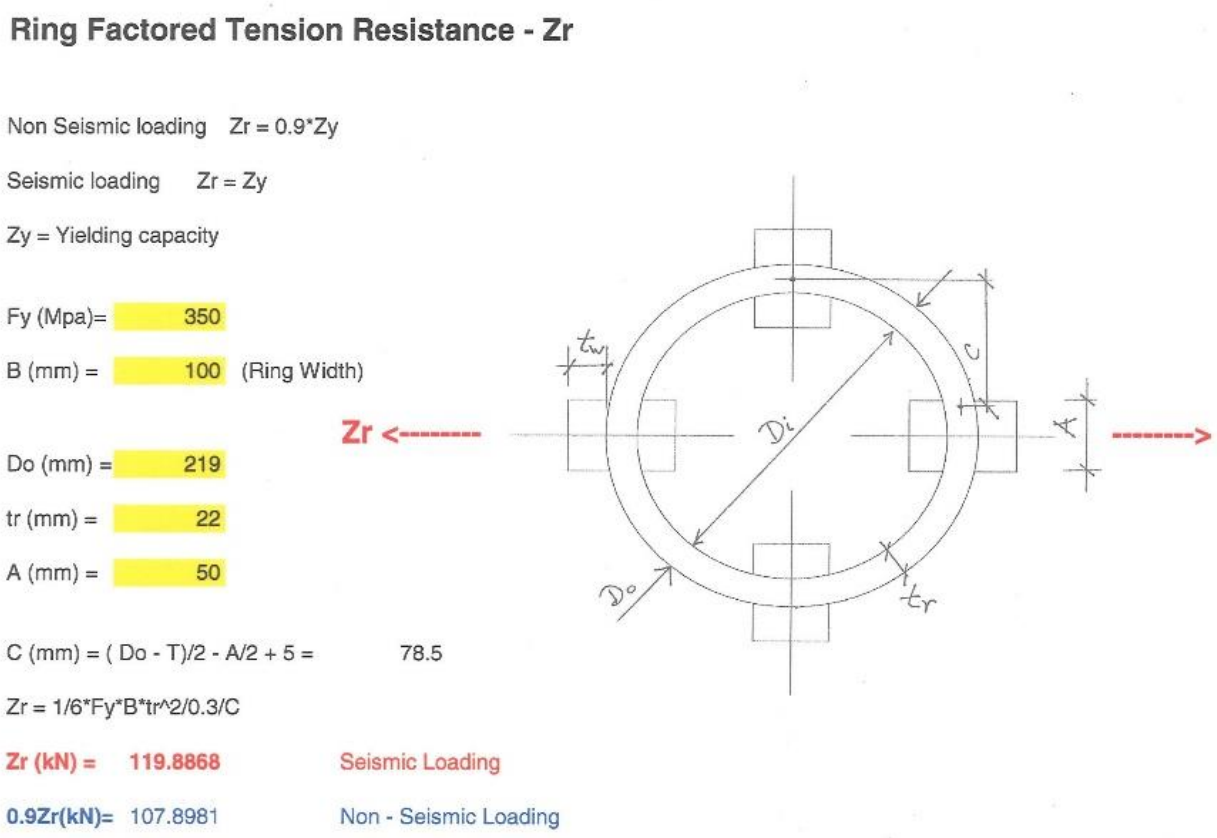

Fig. 6. Ring capacity example.

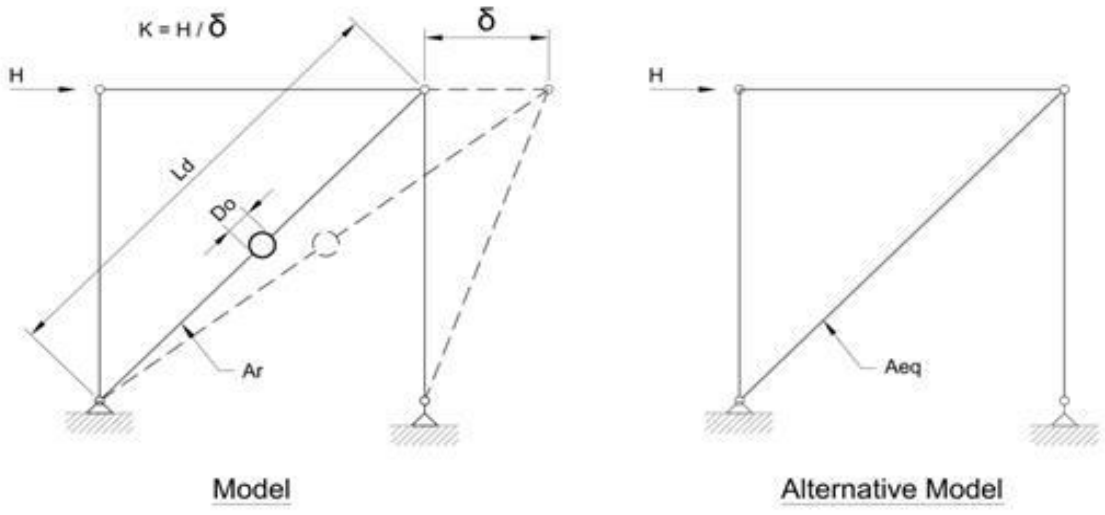

Fig. 7. Bracing stiffness models.

Table 2. Ring stiffness table.

Ring	*Do* (mm)	*tr* (mm)	*B* (mm)	*Kr* (kN/mm)
168/9.5	168	9.5	100	20
168/13	168	12.7	100	50
219/13	219	12.7	100	24
219/22	219	22	100	120
273/13	273	12.7	100	12
273/25	273	25.4	100	95
324/13	324	12.7	100	6.8
324/25	324	25.4	100	55

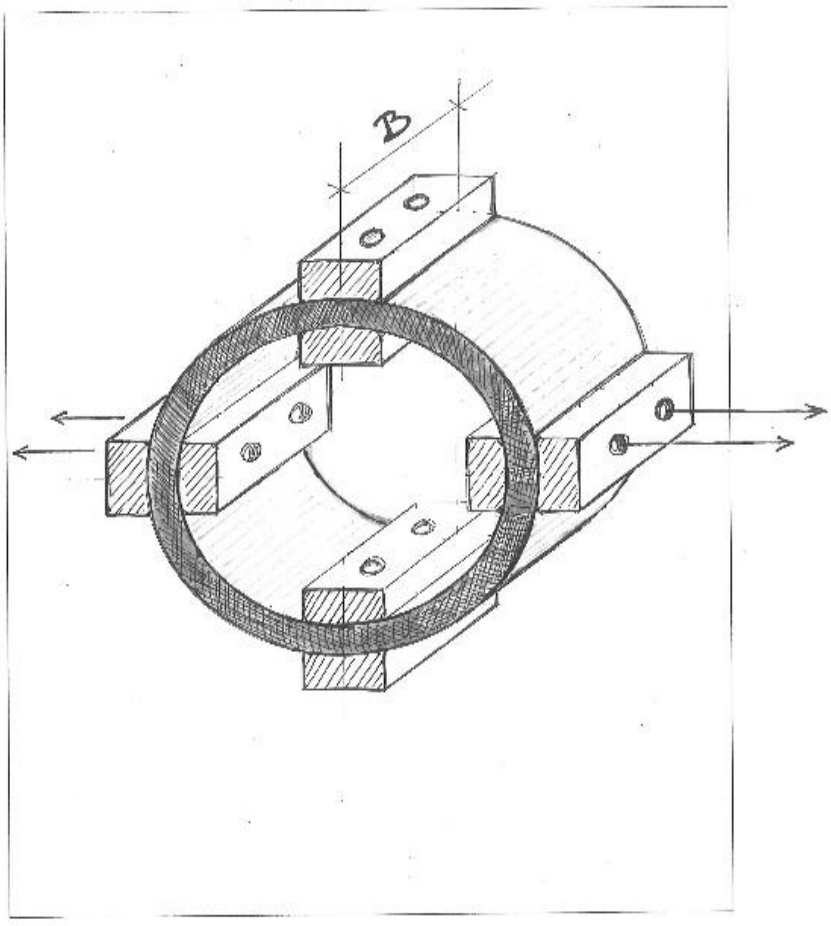

Fig. 8. Ring with multiple rods.

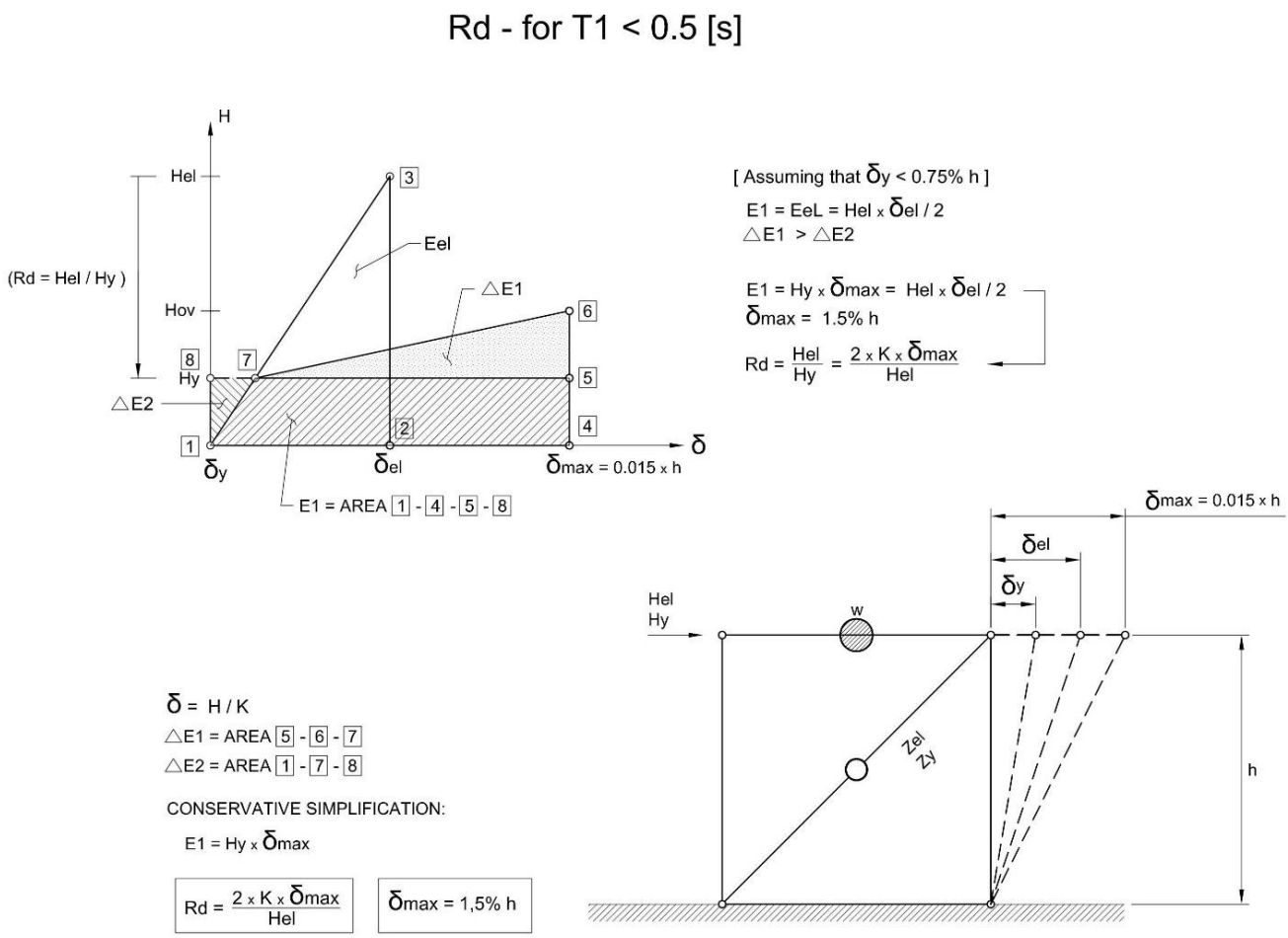

Fig. 9. Energy and drift diagrams.

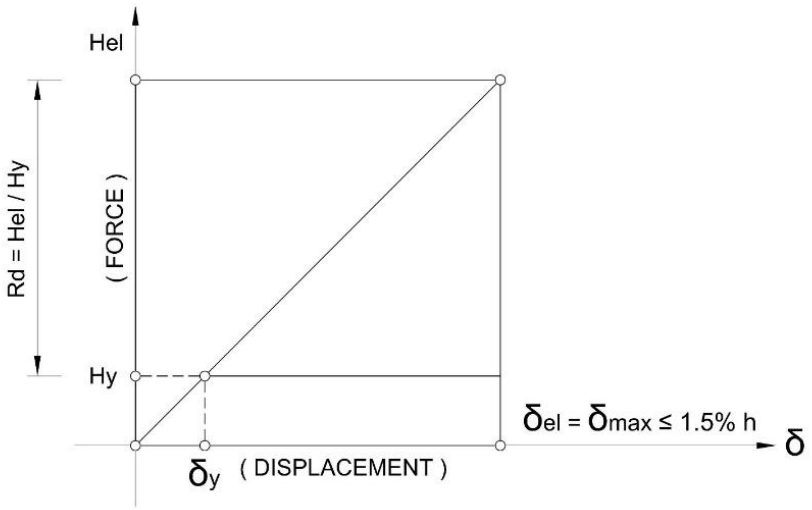

Fig. 10. Equal displacement principle diagram.

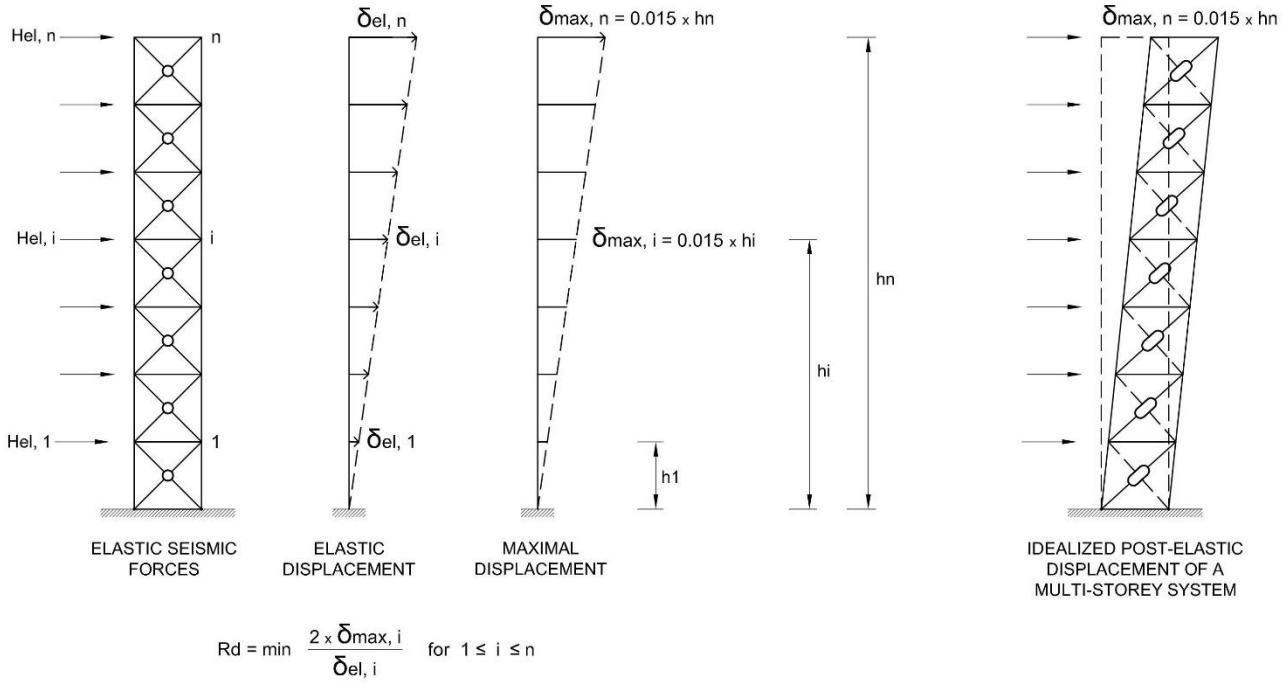

Fig. 11. Multi-storey systems.

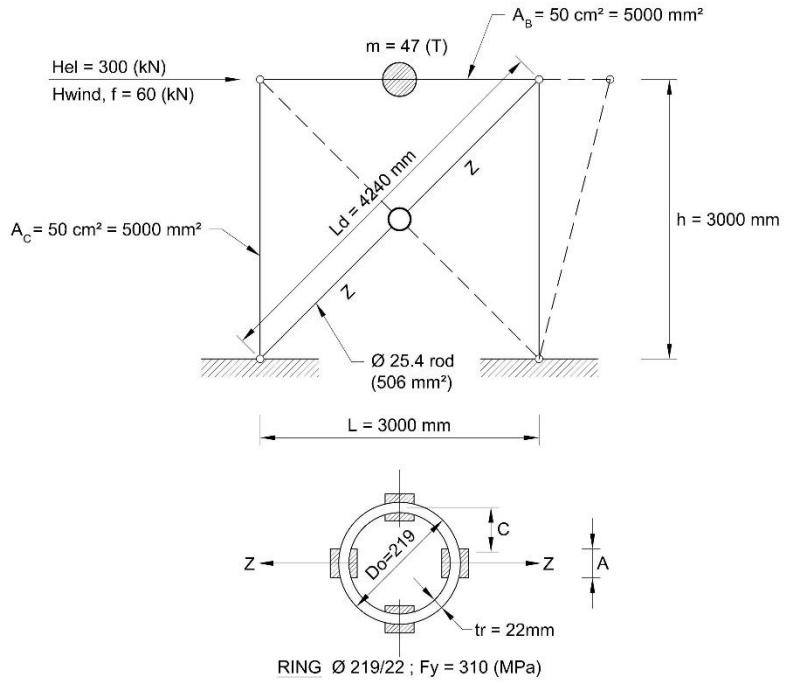

Fig. 12. Design example.

9. Conclusions

The procedure described in this paper allows designers to use a simple and ductile tension-only bracing system. The conservative design methodology described can be refined when the results from multi-storey braced frame tests are available. Larger diameter rings performed better in shake-table testing and can accommodate drift ratios greater than 1.5%.

Appendix A.

Design Example:

- Ring Size: 219/22
- *B* = 100 mm
- *Fy* = 310 MPa
- *A* = 50 mm
- *Ar* = 506 mm2

Wind Load Design

Factored diagonal wind load: *Zf* wind = 1.414 * 60 = 85 kN

Ring factored moment: *Mf* wind = 0.3 * *Zf* wind * *C*

- *C* = (219 - 22) / 2 - (50 / 2 + 5) = 78.5 mm
- *Mf* wind = 0.3 * 85 * 78.5 = 2002 kNmm
- Ring Wind Load Capacity:
- *Mr* wind = 1/6 * 0.9 * 310 * 100 * 222 * 10-3 = 2 250 kNmm

Mr wind > *Mf* wind

or, using *Zr*:

- *Zr* wind = 1/6 * 0.9 * 310 * 100 * 222 / (0.3 * 78.5 * 1000)
- *Zr* wind = 95.6 kN > *Zf* = 85 kN

Or, using *Zr* and Table T1:

- *Zr* wind = 310 / 350 * 0.9 * 120 kN = 95.6 kN > *Zf* = 85 kN (OK)

Seismic Design

- *R0* = 1.50
- *Kr* = 120 kN/mm = 120 000 N/mm (from Table T2)

Equivalent diagonal *Aeq* = *Ar* * *ld* / (*Ar* * *E* / *Kr* + *ld* - *Do*)

- *Aeq* = 506 * 4240 / (506 * 210000 / 120000 + 4240 - 219) = 437 mm2

The bracing is modelled using *Aeq* and a stiffness, K = 10 kN/mm is determined. For a mass *m* = 47 tonnes, the first period T1 = 0.43 < 0.5 (s).

Based on the applicable code, the elastic seismic force, *Hel* = 300 kN and *Zel* = 424 kN

- δmax = 0.015 * 3000 = 45 mm
- *Rd* = 2 * *K* * δmax / *Hel* = 2 * 10 * 45 / 300 = 3.0
- Seismic design force, *Hf* = *Hel* / (*Rd* * *Ro*) = 300 / (3 * 1.5) = 67 kN
- Seismic design diagonal force, *Zf* = 1.414 * 67 = 95 kN
- Ring capacity for seismic loading:
- *Mr* = *My* = 1/6 * *Fy* * *B* * T^2 and *Zr* = *Zy* = *Mr* / (0.3 * *C*)
- *Hy* = 0.707 * *Zy*
- *Mr* = 1/6 * 310 * 100 * 222 * 10-3 = 2500.67 kNmm
- *Zr* = *Zy* = 2500.67 / (0.3 * 78.5) = 106 kN > *Zf* = 95 kN (OK)

Ring Selected: 219/22

- *Hy* = 0.707 * *Zy* = 0.707 * 106 = 75 kN
- Overstrength seismic force for design of the diagonal rods, columns and footings:
- *Hov* = 2.0 * *Hy* < Hel / 1.50
- *Hov* = 2.0 * 75 = 150 kN < 300 / 1.5 = 200 kN

REFERENCES

CSA S16-14 (2014). Design of Steel Structures. CSA Group, Mississauga, Canada.

Djuric M (1973). Stabilnost i Dinamika Konstrukcija. Beogradski Univerzitet, Serbia.

National Building Code of Canada (2010). National Research Council of Canada, Ottawa, Canada.

Ventura CE, Motamedi M, Erdevicki D, Samoru S (2013). Tension-Only brace system for earthquake resistance of low rise buildings. EERF report for Steel Structure Education Foundation.

Challenge Journal of Structural Mechanics

The collapse of WTC 7: A re-examination of the "simple analysis" approach

Robert Korol *, Paul Heerema, Ken Sivakumaran

Department of Civil Engineering, McMaster University, Hamilton, Ontario L8S 4L7, Canada

ABSTRACT

Although the events of that tragic day happened 14 years ago, there remain nagging questions of why the 47 storey WTC 7 steel framed structure collapsed, when it was NOT hit by an airplane. We will review the official rationale of how the collapse events started, and why, in our opinion, the explanation is judged to be wrong. Then, we will proceed with another scenario that says "Okay – let's assume that the two critical storeys did sustain extremely hot fires, so much so that 2/3rds of their columns totally lost axial resistance capability". We then proceed to employ Newton's laws to inquire whether there was sufficient gravitational potential energy due to live and dead loadings in upper and lower floors to overcome the resistance offered by the remaining columns, together with floor slabs known to have been pulverized to reduced particle sizes by surface to surface crushing. Our conclusion suggests that Newton's laws of motion and energy conservation considerations would have had to have been violated to explain that building's total collapse within a debris pile several storeys high.

ARTICLE INFO

Article history:
Received 7 January 2016
Accepted 10 February 2016

Keywords:
Steel framed structures
Extreme fire loadings
Collapse analysis
Energy dissipation aspects
Gravitational potential energy

1. Introduction

Despite the many years that have passed since the horrendous events of 9/11, questions still remain about why such robust, overly-designed and well constructed buildings collapsed on that fateful day in 2001. Of course, airplane strikes and raging fires that purportedly caused the demise of WTC 1 and 2 are one thing, but in the case of the 47 story Building 7, only fires can be blamed. And yet, as engineers we design buildings, steel or reinforced concrete, to resistant such extreme loadings.

Our purpose is to re-examine the evidence and the assumptions employed by others who claim that fires alone can explain why WTC 7 collapsed completely and symmetrically into its own footprint. The official narrative (NIST, 2008a) is that the spread of hot fires from work station to work station, initiated by incendiary debris that catapulted a distance of approximately 100 m, from a collapsing twin tower (WTC 1), was responsible. Their claim is that heavy debris amongst the vast amount of fine dust, broke windows and severed 7 perimeter columns principally on the south face of Building 7. The consequence of that event was that flammable materials within office areas were ignited at various floor levels and subsequently generated sufficient heat in a process known as flash-over, that extended the burning times for nearly 6 hours in some floor levels. According to the government agency known as the National Institute of Standards and Technology (NIST) especially vulnerable was the 13th floor where a girder to interior column connection failed (NIST, 2008b). The hypothesis was that core column 79 lost floor level support, then buckled, resulting in a cascade of failures propagating horizontally. Without an adequate structural support system for the upper block of stories, progressive collapse by gravitational forces alone is claimed to have followed, and therefore was responsible for the outcome – a debris pile a few storeys high, largely within its footprint.

Our recent article (Korol et al., 2015) questions the likelihood that such a scenario could have taken place. However, that said, it may be that some other mechanism of failure may have been at play during this time which NIST may not have recognized. The issue then becomes – what is the probability that the structure would have succumbed to total collapse employing some other scenario of initial failure and subsequent events leading

* *Corresponding author*. Tel.: +1-905-525-9140 ; Fax: +1-905-529-9688 ; E-mail address: korol@mcmaster.ca (R. Korol)
ISSN: 2149-8024 / DOI: http://dx.doi.org/10.20528/cjsmec.2016.02.004

to total progressive collapse? Our approach is one which aims to deliberately avoid answering that question, but rather addresses the very issue at the heart of the matter – i.e. that there was sufficient resistance built into the structure that regardless of a local failure, the structure should not have suffered a total collapse.

2. A Bit of History

Very shortly after the collapse of the twin towers, Bazant and Zhou (2002) published their paper "Why did the World Trade Center collapse? Simple analysis" in the Journal of Engineering Mechanics. Our title highlights "simple analysis" because it is also in that vein that we wish to make the case that a sophisticated analysis is not a prerequisite for verifying or not the rationale for supporting the hypothesis of a gravitational driven collapse. We shall argue that quite the contrary is in fact the case.

Much has been written about whether the gravity driven collapse event itself could have taken place at the speed which was recorded by video cameras. Some analyses claim that the motion of WTC 7 during at least part of the collapse event was too rapid to have happened without the use of explosives (Griffin, 2010) while NIST (2008) and Dunbar and Regan (2006) refute such claims. While such approaches may utilize Newton's laws of motion correctly, they suffer from an inherent weakness – namely, underestimation of the built-in resistance of a steel-framed structure that has floor systems consisting of materials, in particular concrete slabs possessing shrinkage steel which when tallied together will absorb copious amounts of energy. When accounting for such energy absorption potential that is possessed by a structure poised to tumble down into a pile of rubble, we are compelled to ask whether the gravitational potential energy of such a structure will exceed the inherent dissipative capacity. It is in this context about which we wish to make the case of whether there was the likelihood of a total collapse of Building 7 following fires that would have seriously weakened the gravity support system in storeys known to have been compromised because of weakened conditions due to fire.

3. Basic Assumptions

Several floors in WTC 7 were known to have been subject to hot fires during late morning and the afternoon of Sept, 11th, 2001. The most intense of these are reported to have been on floors 12 and 13 (NIST, 2008b). It is unknown whether intense heat occurred simultaneously or if at essentially the same time. We will make the assumption that columns on both floors were compromised at the same time, a conservative estimate. As well, we will ignore the energy associated with floor beams and girders bending or twisting, or steel connections failing, or indeed of filing cabinets, inside partitions, tables and chairs being crushed. Our focus will only be on the 82 steel columns existing from above the 7th floor level, up to the 44th, with 70 in the top 3 storeys, together with pulverizing portions of concrete slabs that would have been subject to crush forces due to steel floor members impacting the floors below.

4. Energy Absorption Capacity of Columns

In their "rapid communication" paper to the Journal of Engineering Mechanics, Bazant and Zhou (2002) state unequivocally in the abstract "The analysis shows that if prolonged heating caused the majority of columns of a single floor to lose their load carrying capacity, the whole tower was doomed". Since they were not privy to the details of the columns at the time of their original version (2 days following the 9/11 events), such a statement without evidence was indeed surprising. While the context pertained to one or both of the twin towers, the "simple analysis" could, and was used by NIST in their final report (2008b) in analyzing the rapid progressive collapse of WTC 7. Unfortunately, despite the many years following 9/11, there was virtually no effort made to postulate a collapse scenario that employed basic principles of mechanics and which considered the real energy dissipative capacity inherent in the columns under the circumstances that occurred, i.e. raging fires that would potentially jeopardize the ability of some structural elements to sustain reasonable intensities of service loading. The Bazant and Zhou model, which formed the basis for collapse of a typical column, assumed plastic hinges at the top, bottom and at mid-height. This may appear at first blink to be a collapse mechanism that over-estimates the energy absorbed during post-buckling because of presumed fixity at floor and ceiling junctions with cross members. However, such a model does not account for the non-recoverable energy associated with axial compression – the attribute about which columns are meant to resist.

At McMaster, a series of experiments was undertaken on H-shaped columns of ductile aluminum possessing stress-strain properties similar to mild structural steel, and which had effective lengths similar to those experienced in building design (Korol and Sivakumaran, 2014) with simply supported ends. That research showed that the energy dissipation was typically 3.5 times that which would be obtained by multiplying the plastic moment by the angle formed at a plastic hinge. However, if single hinges only are assumed (as presumed by NIST (2008b)) the dissipative energy can therefore be conservatively estimated to be increased by the above factor for purposes of computing energy dissipation potential for those columns whose strength was unaffected by the fires at the time of collapse initiation.

5. Energy Absorption by Floor Slab Crushing

In addition to columns subjected to buckling and crushing, there was a great deal of pulverization of concrete involved in the collapse of all three WTC buildings. Several studies suggest that concrete, being a brittle material will pulverize in accordance with its specific fracture energy value, GF (Abdalla and Karihaloo, 2003). However, tensile stresses are the basis for experimentally determining this property, and when a hard body such as a collapsing girder impacts a floor slab below, the applied forces cause both localized crushing of the concrete floor's surface, and lateral displacements that

would typically be resisted by a steel mesh or spandrel beams offering resistance to such movements. In other words, such events do not at all resemble fracture by wedge-splitting or point loading, which are methods used to calculate GF.

Indeed, the energy needed to pulverize a slab by crushing is substantially higher than one would compute using the models proposed by others (Bazant et al., 2008, Greening, 2006). However, researchers in the mining and milling industries have developed empirical relationships that link energy inputs to the type of equipment employed to break-up brittle materials into smaller sizes. For example, grinding and crushing methods are commonly used in those industries for which knowledge of energy inputs is of importance for procuring equipment needed for a given production process. A commonly used equation for determining the energy needed to break up rock-type materials such as by grinding was developed by Bond (1952), while for crushing, Eloranta (1997) amended the Bond equation given below to account for such a method that is much less efficient in pulverizing such materials.

The Bond formula itself is given as

$$E = 10W_i\left(1/\sqrt{x_f} - 1/\sqrt{x_i}\right), \quad (1)$$

in which E is the energy per unit mass to pulverize particle x_i to size x_f expressed in microns (μm), while W_i is the energy required to pulverize a given rock-type material from theoretically infinite size to 100 microns. The factor 10 in Eq. (1) is actually $\sqrt{100}$ μm, thus providing dimensional consistency. Traditionally, E and W_i were both established in units of kilowatt hours per ton (kWh/t), but for our tests, we chose units of J/kg, and as such, have to multiply the right hand side by 3600. Eloranta's modification for crush-type pulverization is simply to multiply the right hand side of Eq. (1) again, by a factor 3.4 which is a very significant amplification of energy needed for reducing brittle materials to smaller particle sizes.

For our research, we undertook penetration load tests on rectangular reduced scale models employing a solid 50 mm square sized steel loading block on both unreinforced (Korol and Sivakumaran, 2012) and shrinkage steel reinforced concrete slabs (Sivakumaran et al., 2014), light weight and normal strength, to better simulate the action of penetration-type loadings from falling debris that is associated with storey-to-storey collapses. To estimate the energy potentially available to be absorbed through a combination of crushing and general breakup of floor slab areas not experiencing a direct impact by a falling girder or beam expected to occur during a collapse event, we used a combination of Bond and Eloranta amended expressions for our slab specimens to compute a work index constant, W_i. Under the patch load of area a, applied to a slab having an overall size, A, it was assumed that Eloranta's 3.4 factor would apply, but for the remaining slab area, A-a, Eq. (1) would be more appropriate.

We therefore obtain a modification of Eq. (1) that retains W_i, given by:

$$E_c = \left\{10 * 3600\left(1/\sqrt{x_f} - 1/\sqrt{x_i}\right)(1 + 2.4a/A)\right\}W_i, \quad (2)$$

where E_c is the energy of combined methods of pulverization expressed in units of Joules/kg. For a/A values of 0.01, 0.04 and 0.16, we obtained values of W_i that averaged 4.0 kWh/t (Sivakumaran et al., 2014), a value that seems reasonable when compared with Doering International's values for blast furnace slag, ranging from 12 to 16, while cement clinker is noted as having a value of 15 kWh/t (Doering, 2011).

6. Floor Slabs to Particle Size Distributions

A major challenge in attempting to employ Eq. (2) is the question of what x_f value(s) to use. In the case of WTC 1 and 2, video recordings clearly showed that a vast amount of very fine dust was produced during their respective collapse events. And, the finer the particle sizes, the higher will be the energy inputs needed to create such dust, through what is known as comminution theory. However, our focus is on WTC 7, the floor areas being of normal weight concrete (2,400 kg/m3), nearly an acre in size, i.e. 3853 m2, denoted as A_f in what follows. Essentially the structure collapsed in its own footprint, so a distribution of particle sizes for the steel mesh reinforced floors has to be a guesstimate, and one which offers a lesser degree of very fine sizes than that which the twin towers experienced. One finding from our slab tests was that the weight of pieces having an average size > 20 mm was somewhat over 50% for the largest slabs tested (a/A < 0.16). Assuming for a typical collapsed floor that 50% would be large chunks, say 100 mm in size, with the remaining x_f bits retained equally in weight on sieves of sizes: 20, 5, 1.25 mm, and 630, 160, 60 and 30 μm, (the standard array in concrete lab test facilities) i.e. 7.1% for each of the seven, we obtain from Eq. (2) and with W_i = 4.0 kWh/t, a value for the energy dissipation potential for confined concrete, ED_c = 4900 J/kg. A detailed description of several scenarios conceived is noted as no.4 in Tables 3 and 4 of an earlier paper (Korol and Sivakumaran, 2014). We will employ the above ED_c value when we tally up the dissipative energy contributions.

7. Energy Considerations for Progressive Collapse

The analysis to be pursued avoids the controversy of the speed of descent of the structure during the collapse event itself. Our focus is only on the potential energy of the live and dead loads existing on the floors and roof above the level of the debris pile (estimated to be the 7th floor), and the built-in energy of the structure itself that is restricted to the columns and the concrete floor slabs. In this determination, we are ignoring any permanent plastic deformation of the girders, floor beams and connections that no doubt would also have played a role in resisting the collapse of the structure.

Firstly, we will consider the potential energy of the block of storeys above the two floors that are claimed to have been the most severely damaged by fire, i.e. levels 12 and 13. We know that WTC 7 remained motionless until late afternoon on that fateful day in September

2001, i.e. more than 6 hours after fires started in lower floors due to burning debris from the collapse of WTC 1. Since structures are designed to have safety factors to account for overload conditions, building codes prescribe load factors that apply to both dead and live loads. A reasonable estimate of safety for the conditions at the time prior to 5:20 pm is that the actual live load is considerably less than the factored design live load by at least a factor of 3. If L is denoted as the live load per unit area, 1.5 L is frequently used in the design of the structure. If D denotes the dead load, then 1.25 D is oftentimes employed in design. An additional factor to consider is the resistance factor which recognizes the possibility that the strength of structural members might be somewhat less than that specified, and as such the nominal resistance of a member or the full structure for our purposes can be given as $(1.5L + 1.25D)/\Phi$, where $\Phi < 1$ is known as the resistance factor, varying from about 0.6 to 0.9 depending on the material. Since the structure was essentially vacant during its collapse, occupancy loading can be assumed to have been virtually zero, but those materials housed within office spaces and untouched by fire would remain as part of the mass contributing to L with the total being < 0.5 L. Meanwhile, dead loads D would generally be reduced only slightly due to combustion of some materials such as permanent partitions. A reasonable estimate, then, is to assume that in- service loads per floor in a fire scenario would be $M = 0.5\ L + D$. Accounting for the Φ factor, suggests that an overall factor of safety of 3 might be reasonable.

The consequence of a factor of 3, therefore suggests that one would require slightly more than the equivalent of two-thirds of the 82 columns (below floor 45) to have to totally fail while slightly fewer than 1/3 would be left resisting the loads above. At the instant that the building was about to collapse, therefore, we assume that 27 remained unscathed on each of floors 12 and 13 while the other 55 would have succumbed. Of course, such a scenario would be based on all columns having the same size and loading, which was not the case in reality. However, we make a not unreasonable assumption that if all the column sizes are known, an average size within the series of H-shapes that were employed in WTC 7's construction, could be selected that meets the same overall strength capacity on each floor as those that comprised the assemblage of columns existing at the time.

8. Potential Energy Portions

To be consistent with Bazant and Zhou's theory (2002) of crush-down followed by crush-up, we postulate three distinct contributions to gravitational potential energy at the time that the structure was poised to collapse. These we compute as follows:

- There exists an upper block of 35 floor levels (14th floor up to and including the roof) that will move downwards as a rigid block and which stops its motion at level 7 . It is represented as Block A in Fig. 1 with a height of 7 H_i above floor 7, where H_i is a single storey height = 3.89m (12'9"). Each floor, with the exception of those associated with storeys 21, 22 and 23, has a prescribed mass $M_i = \{(D + 0.5\ L)\ A_f\}/g$ = [3.6 + 0.5 (2.4)](3853)(1000)/9.81 = 1,885,000 kg while the three noted above have values of D and L of 4.3 and 3.6 kPa respectively, thus raising the mass value on those floors to be 2,396,000 kg, which we denote as M_j. Note that the above mass values were obtained from Cantor information sheets (1985), and confirmed by NIST's draft for public comment report, chapter 2, "WTC 7 Building Description" (NIST 2008c). These mass totals and are presumed not to include the self-weight of the columns to be addressed below.
- Then, there is the group of floors that drop one upon the other in a series of collisions that involve impact energy losses as computed by the conservation of momentum principle. Each impact in turn, involves a slightly lesser amount of energy loss. For example, the first impact involves a drop in velocity that's dependent on the mass ratio of 35 levels melding into floor 13 to give a reduction in kinetic energy of 5.5%. However, for the case of five added floors impacting the 8th level, the ratio is dependent on the 40 floors above merging with the one below, with the result that the kinetic energy is reduced by 4.8%. On average then, we can assume a 5% drop in potential energy during such collisions for the Block B group of floors (8th to 13th inclusive). Such an assemblage, ending the crush-down phase of collapse, drops on average 3.5 H_i while the mass of colliding storeys is 6 M_i. Fig. 2(a) shows the final crush-down collapse state with all floors above storey 13 having toppled onto floor 7.
- Finally, there is the assemblage of floors above the 14th whose potential energy is related to the crush-up phase of collapse. Since there are no floor collisions during this collapse phase, we need only multiply the total mass of 35 levels with the centroidal height above the 14th floor (resting at level 7) taken as 17 H_j, a value slightly below the mid-height value of 17.5 H_j. The Cantor drawings indicate a range of storey heights of 3.89m (12.75') to 4.52m (14.83'), with the average value of H_j = 4.4 m (14.4'). An additional mass to consider is that due to the totality of column self-weights for Block A (Fig. 1(a)), m_{Acol} . From the column schedule for WTC 7, the total mass tallies up to a total of 6,530,000 kg, a value that is 9.7% of the value calculated as Σ (0.5 L + D) for the 35 levels.

9. Total Gravitational Potential Energy

a) Crush-down

At the start of crush-down, Block A will drop H_i , collides with floor 13, which then adds floor mass level with some slowdown in velocity, and continues its motion down to our presumed debris pile level at floor 7. The total potential energy for Block A to move downward from level 14 to level 7 is: $[(32\ M_i + 3\ M_j) + m_{Acol}]\ g \cdot 7\ H_i$ = 19.78 x 10^9 Joules. For convenience, we denote the term in square brackets as M_A which computes as 74,038,000 kg.

In addition, storeys 13 to 8, noted as Block B in Fig. 1(a) could potentially displace downwards to level 7 and which would involve collisions when impacts occur. Those assoiciated floors will also contribute to crush-down potential energy. As noted they drop on average an amount of 3.5 H_i , and when accounting for losses of

about 5% due to impacts of Block A with floors 13, 12, 11, 10, 9 and 8, the result is a contribution of [6 M_i + m_{Bcol}] g · 3.5 H_i (1- 0.05), where m_{Bcol} for those 6 storeys = 836,600 kg. Again for convenience we will refer to the Block B masses as $M_B = 6M_i + m_{Bcol}$, equal to 12,147,000 kg, with its potential energy computed to be 1.541 x 10^9 Joules.

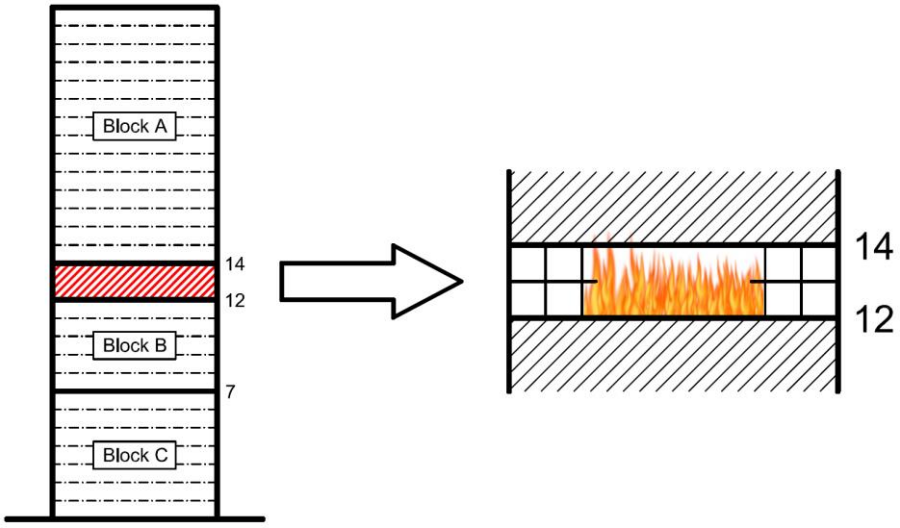

Fig. 1. Structure poised to collapse.

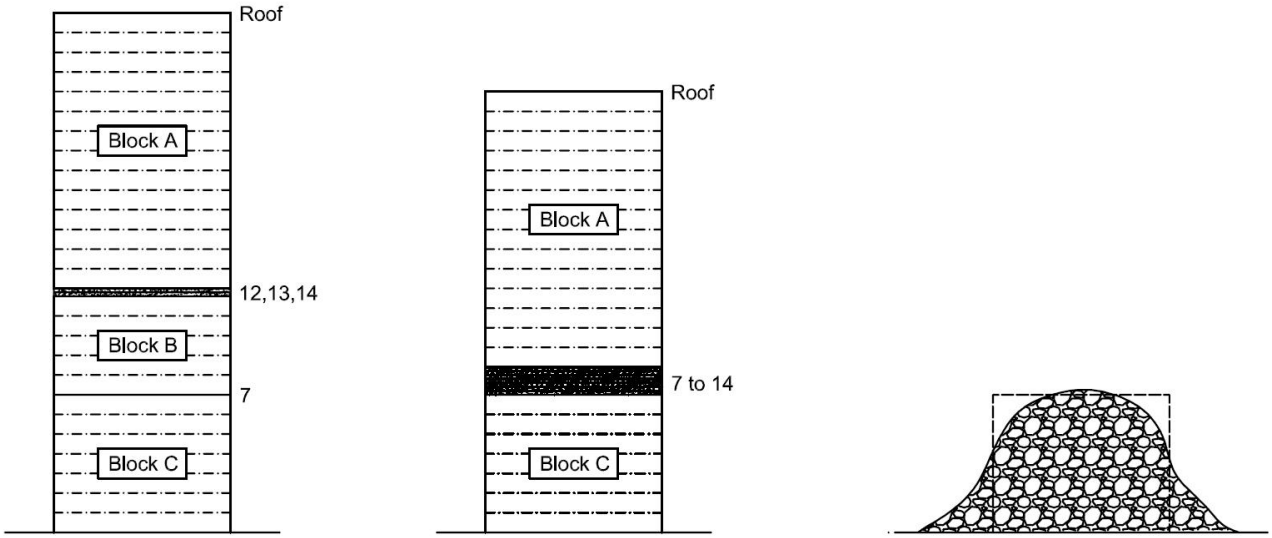

Fig. 2. Theoretically possible collapse states: a) Crush-down to Floor 12; b) End of crush-down phase; c) Debris pile idealized.

b) Crush-up

As noted in subsection (3), this potential energy contribution is simply the product of floor masses comprising Block A with the gravitational constant and the centroidal distance above the debris pile. As noted earlier, the total mass including the column self weights is given as M_A, while its centroidal distance is approximately 17 H_j. The product that includes the gravitational constant g = 9.81 m/sec^2, results in a loss of potential energy of 54.3 x 10^9 Joules.

Summing up all the potential energy contributions results in a value of 75.7 x 10^9 Joules. The question to be answered, then is: How does this value compare with the total potential dissipative energy that's available from the compressed H-shaped WF columns and concrete floors possessing shrinkage steel mesh? We will address this issue in the next section.

10. Energy Dissipation Considerations

a) Crush-down

We begin our analysis considering only the absorptive energy capacity of the structure during the crush-down phase of collapse. Due to the large number of columns existing at any floor level and the variety of sizes within the W360 section class, we identified an average size that suits resistance under axial compression for individual storeys. Information pertinent for the lower storeys subjected to crush-down is provided in Table 1.

Considering all the columns in the storeys noted as having the same cross sectional properties (due to the rolled shape size limitations), we obtain for the total of 464 columns with plastic section modulus values, Z_y (col. 5) (noted in column 5 of Table 1) = 10,700 x 10^3 mm^3, a plastic hinge rotation of 0.9 π, together with an average

yield stress of F_y = 276 MPa, we obtain a total column energy dissipation value of $\sum$ [(464 x 0.9 π x 10,700 x 10^3 x 276)(3.5)], where the 3.5 factor was determined from tests performed at our structural laboratory at McMaster University (Korol and Sivakumaran 2014). The total then computes as 13.56 x 10^9 Joules.

Table 1. Average core and perimeter column values (Block B).

Storeys in Crush-Down Collapse	No. of Columns Resisting Load	Avg. Weight in kN/m (lbs/ft)	Column Size to Suit	Plastic Section Modulus Z_y 10^3 mm^3 (in^3)
13	27	8.15 (562)	W360x900 (14W605)	10,700 (652)
12	27	8.44 (581)	"	"
11	82	"	"	"
9-10	82	8.57 (590)	"	"
7-8	82	8.60 (592)	"	"

Considering all the columns in the storeys noted as having the same cross sectional properties (due to the rolled shape size limitations), we obtain for the total of 464 columns with plastic section modulus values, Z_y (col. 5) (noted in column 5 of Table 1) = 10,700 x 10^3 mm^3, a plastic hinge rotation of 0.9 π , together with an average yield stress of F_y = 276 MPa, we obtain a total column energy dissipation value of $\sum$ [(464 x 0.9 π x 10,700 x 10^3 x 276)(3.5)], where the 3.5 factor was determined from tests performed at our structural laboratory at McMaster University (Korol and Sivakumaran 2014). The total then computes as 13.56 x 10^9 Joules.

Regarding concrete pulverization, we'll assume that fires were so hot on floors 12 and 13 that the concrete would have been weakened sufficiently from the heat that their ability to absorb energy would have been fully compromised. Including then, only floors 7 to 11 inclusive, and assuming normal concrete with an average thickness of 101.6 mm (4") we get for the 5 floors a total amount of energy equal to 32.01 x 10^9 Joules. The total amount of energy dissipation during crush-down therefore is the sum of the two which is 45.57 x 10^9 Joules.

b) Crush-up

For those storeys above the 14th floor, we only need to undertake a rough calculation about equivalent column sizes, since our computations indicate that 60% of the total potential energy has already been accounted for, and there are 35 levels (34 storeys) that will involve both plastic hinge buckling of columns and pulverization of concrete slabs. It is clear with only rough computations that the energy dissipation far exceeds that of the gravitational potential energy of the building collapsing into a debris pile at floor level 7. As such, we assume that storey 31 (half way up Block A) is representative for that assemblage of columns.

An average size *W* section at storey 31 (Cantor 1985) results in selecting a W360x551 possessing a plastic section modulus of 6,050x10^3 mm^3 about the weak axis of bending. For the 2752 columns (82 and 70 respectively for storeys 14-44 and 45- 47) in Block A, the total amount of column energy potential works out to be 45.5 x 10^9 Joules. Meanwhile, the crushing of 34 floor slabs in Block A computes as an energy dissipation of 218 x 10^9 Joules, resulting in a total of 263.5 x 10^9 Joules for this upper block of storeys.

Then, when we add in the value for Block B's crush-down total of 45.6 x 10^9 we get a grand total amount of energy dissipation of 309.1 x 10^9 Joules. This value, therefore, is 309.1/75.7 or 4 times the gravitational potential energy associated with a full collapse of the structure. However, it's of interest to carry this analysis one step further.

11. Where Does the Motion Stop?

We begin with the energy balance equation for computing the velocity of Block A after a one storey drop to floor level 13. The only energy dissipation will involve the 27 columns that were almost sufficient to support the loading above. Since the initial energy state has zero velocity the following equation applies:

$$1/2\,(M_A)\left(v_A^f\right)^2 = M_A g H_i - 27 * 0.9\pi Z_y F_y * \alpha_{hfac}\,, \qquad (3)$$

in which v_A^f is the velocity of Block A at impact with floor 13 and α_{hfac} is the plastic hinge correction factor that accounts for axial compression taken to be 3.5 as noted earlier from our McMaster tests. As Table 1 indicates, the equivalent column size needed to offer the same or slightly higher resistance than the actual average size is a W360x900. Substituting appropriate values into Eq, (3) in which M_A = 74.0 x 106 kg and H_i = 3.89 m results in a value of v_A^f of 7.42 m/sec.

The next stage involves conservation of linear momentum that accounts for a reduced velocity during motion Block A plus one floor in storey 12. The initial storey velocity of the moving front is therefore 35/36 times 7.42 to give the initial velocity of v_{A+1}^i of 7.21 m/sec. (Note that the subscript "*A+1*" denotes Block A plus an

added storey). Our equation for the 12th storey must include both potential and kinetic energy inputs to evaluate to determine that storey's final velocity. And so, in this case, we have:

$$1/2\,(M_{A+1})\left(v_{A+1}^{f}\right)^{2} = 1/2\,(M_{A+1})(7.21)^{2} + M_{A+1}gH_i - 27 * 0.9\pi Z_y F_y * \alpha_{hfac}\,. \quad (4)$$

Solving for the 12th storey final velocity gives a value of v_{A+1}^{f} = 10.37 m/sec

Moving now to the 11th storey, conservation of momentum gives v_{A+2}^{i} a value of (37/38) times 10.37 = 10.097 m/sec. In this case we have 82 columns offering resistance and a concrete floor area, A_f, that is subject to pulverization. The equation that applies in this case is:

$$1/2\,(M_{A+2})\left(v_{A+2}^{f}\right)^{2} = 1/2\,(M_{A+2})(10.097)^{2} + M_{A+2}gH_i - \left[82 * 0.9\pi Z_y F_y * 3.5 + ED_c A_f d_c \rho_c\right], \quad (5)$$

where ED_c is the pulverization value or 4900 J/kg, d_c is the slab depth of 101.4 mm (4"), and ρ_c is the concrete density of 2400 kg/m^3. The floor area A_f = 3853 m^2 as noted earlier.

Substituting the appropriate values results in the right hand side ends up as a negative value. The conclusion, therefore, is that the structure's collapse is arrested in the 11th storey. Indeed, it is the pulverization component that is responsible, being about twice the energy dissipater compared to the steel columns. This result would mean that Block A, with two floors added, is stopped when impacting the 11th storey floor. The structure then is restricted to collapsing to 3 storeys.

12. Conclusions

Our objective at the beginning of the study was to simply investigate whether there was enough energy dissipative capacity in the 47 storey WTC 7 high rise steel frame structure to offset its gravitational potential energy for the case of an extreme fire loading event. As noted by NIST in their NCSTAR 1-9 report, very hot fires are claimed to have been present in the 12th and 13th floors for several hours during the late morning and afternoon of 9/11 sufficient in fact to cause the total collapse of the building. The authors decided to revisit the problem to ascertain for ourselves whether the structure's demise could have happened under conditions of two storeys being substantially weakened by the heat.

Regarding our focus on gravitational potential energy versus the dissipative energy possessed by the structure, we found that the former was insufficient to cause a total collapse scenario to occur by a factor of 4. The question then morphed into a more detailed analysis whereby we wanted to know the extent of a partial collapse. Indeed, our assumptions and analysis based on Newtonian mechanics clearly show that a very limited partial collapse would have been possible but that it would have been restricted to the storeys in which the fires occurred and to the one below. Some might argue that an upper storey would have been more vulnerable, however, the column sizes involved were so little different, we decided to adopt the Bazant hypothesis that crush-down would take precedence over crush-up. As noted, our progressive collapse investigation involved a storey-by-storey analysis that was initiated with Block A, the base of which was presumed to be the 14th floor. It was presumed that a crush-down descent would begin with the equivalent of only 27 columns capable of resisting the column and service loadings that the design engineering firm, Irwin Castor, prescribed in their loading schedule for dead and live loads. This number was based on the design possessing an overall factor of safety of 3, a not unreasonable factor that is consistent with building code standards in general. As well, we treated perimeter and core columns as being equally loaded across floor areas that were vulnerable, since WTC 7 is known to have come straight down as observed by video cameras.

References

Abdalla HM, Karihaloo BL (2003). Determination of size-independent specific fracture energy of concrete from three-point bend and wedge splitting tests. *Magazine of Concrete Research*, 55, 133-141.

Bazant Z, Zhou Y (2002). Why did the world trade center collapse? – Simple analysis. *Journal of Engineering Mechanics*, ASCE, 128(1), 2-6; Addendum, 128(3), 369-370.

Bazant ZP, Le J-P, Greening FR, Benson DB (2008). What did and did not cause collapse of the WTC twin towers in New York. *Journal of Engineering Mechanics*, 134(10) 892-903.

Bond FC (1952). The third theory of comminution. *Mining Engineering Journal*, 193, 484-494.

Cantor IG, Structural Engineers (1985). Structural Drawings of 7 World Trade Center.

Doering International Corporation (2011). Grinding Media Size Formula – Work Index for Different Materials According to Bond. Sinn, Germany.

Dunbar D, Regan B (2006). Debunking 9/11 Myths – Why Conspiracy Theories Can't Stand Up to the Facts: An In-Depth investigation by Popular Mechanics. New York Hearst Books.

Eloranta J (1997). The efficiency of blasting versus crushing and grinding. *Proceedings of the 23rd Conference of Explosives and Blsting Technique*, Las Vegas, Nevada, 1-7.

Greening FR (2006). Energy Transfer in the WTC Collapse. WTC Report.

Griffin DR (2010). The Mysterious Collapse of World Trade Center 7. Olive Branch Press, Chapter 6, 125-144.

Korol RM, Sivakumaran KS (2012). Energy absorption potential of light weight concrete floors. *Canadian Journal of Civil Engineering*, 39, 1193- 1201.

Korol RM, Greening F, Heerema P (2015). Performance-based fire protection of office buildings: A case study based on the collapse of WTC 7. *Challenge Journal of Structural Mechanics*, 1(3), 96-105.

Korol RM, Sivakumaran KS (2014). Reassessing the Plastic Hinge Model for Energy Dissipation of Axially Loaded Columns. *Journal of Structures*, 2014, 795257.

NIST (2008a). Final Report on the Collapse of World Trade Center Building 7. NIST-NCSTAR 1A, National Institute of Standards and Technology, Gaithersburg, Md.

NIST (2008b). Structural Fire Response and Probable Collapse Sequence of World Trade Center Building 7, NCSTAR 1-9, National Institute of Standards and Technology, Gaithersburg, Md.

NIST (2008c). Draft for Public Comment, WTC Investigation, NCSTAR 1-9.

Sivakumaran K, Korol R, Fan X (2014). Energy absorption potential of concrete floors containing secondary (shrinkage and temperature) reinforcements. *Frontiers of Structural and Civil Engineering*, 8(3), 282-291.

Challenge Journal of Structural Mechanics

Seismic performance of a pre-cast concrete arch system

Amaia Martinez [a,*], Martin E. Turek [a], Carlos E. Ventura [a], Jay Drew [b]

[a] *Department of Civil Engineering, University of British Columbia, Vancouver V6T 1Z4, Canada*
[b] *Lock-Block Ltd., Richmond V6V 1M7, Canada*

ABSTRACT

Lock Block Ltd of Vancouver, Canada produces pre-cast concrete products, including their name-sake retaining wall system which uses recycled materials. More recently they have adapted these products to create a system of easy to assemble dome and arch structures. This study aims to evaluate the behavior of these systems when subjected to seismic loading. A program of experimental shake-table testing was undertaken using a small scale arch models. For the tests, a suite of six earthquake records were chosen, including Tohoku 2011, Loma Prieta 1989 and Kobe 1995. The records were time scaled to increase the applied frequencies to the tested models; the accelerations were applied full-scale. For each model, they were tested with increasing intensity until failure occurred; this determined the failure level for each earthquake. For all the cases, the failure mode exhibited the typical four-hinge mechanism. The failure intensity varied with type of earthquake, with impulses being the dominant factor. The study also explored a method of reinforcing the arches, using a steel band over the structure to withstand the tension force, anchored at both ends of the arch. This method performed well to all applied earthquakes.

ARTICLE INFO

Article history:
Received 12 January 2016
Accepted 16 February 2016

Keywords:
Arch
Pre-cast concrete
Earthquake
Scaling
Blocks

1. Introduction

Lock Block Ltd is the manufacturer of pre-cast concrete products, including their name-sake retaining wall system. They have developed a system of arches and domes using these blocks, using special forms to create angular shapes required for these systems. While arches are a well established structural system for gravity loads, there are potential issues for an unreinforced arch subjected to seismic loads. This project attempts to define the seismic response of the arch by means of shake table testing of scale models and looks at effective methods of reinforcement.

Lock Block creates scale models of their products, which allows them to experiment with new geometric configurations. The models are cast using grout at $1/25^{th}$ scale. A series of shake-table tests were performed on scale model 6m arches. The weight of the blocks is proportionate to their size and this allows for useful response of the models the shaking. The test time histories were chosen to represent the current design in BC, and also choosing a selection of significant earthquakes from around the world. For each test, the record is applied at a reduced intensity, and then incrementally increased until failure. This establishes the failure level for each model to each applied earthquake.

For the external reinforcement, a steel band is attached along the outer edge of the arch. The band was instrumented with strain gauges and tested on the shake table to determine the forces in the band due to the same records.

This paper presents the background to this project, results of the unreinforced system and preliminary results with the reinforced system.

2. Background

The Lock Block (TM) is a pre-cast concrete unit designed for use in retaining wall systems. It is made by Lock Block Ltd., of Vancouver, BC, in their material recycling plant located in the Lower Mainland. The recycling plant reclaims material to make new concrete,

* *Corresponding author*. Tel.: +1-778-558-6179 ; E-mail address: amaiamar2@gmail.com (A. Martinez)
ISSN: 2149-8024 / DOI: http://dx.doi.org/10.20528/cjsmec.2016.02.005

which can obtain strengths of 20MPa. Over the last several years they have been experimenting with various shapes of forms to create arch and dome structures. Several demonstration structures have been built, including 3m and 6m arches. The arches can be built in relatively short time using chains and a few extra blocks, and a single excavator. Once all the blocks are in place the keystone is placed and the chains are loosened to bring the structure into place.

Much research has been done on the seismic performance of masonry arch and dome structures, primarily to study existing, historically significant architecture. A significant work was done by DeLorenzis et al (2007) which proposed an analytical model for masonry arches. The model assumed fixed hinging points and is based on rigid-body geometry. It describes the collapse of the arch based on the 'four-link' mechanism. The arrangement of the four-link mechanism is shown in Fig. 1; this mechanism requires the formation of three hinges which precedes collapse.

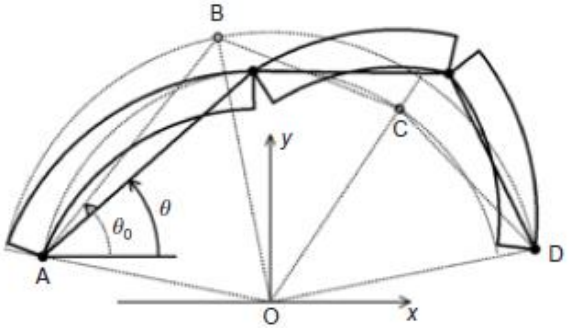

Fig. 1. 'Four-link' mechanism described by DeLorenzis et al. (2007).

A complimentary work by DeJong et al (2008,2010) performs shake-table testing on scale models of arches, while applying the analytical model to each tested arch. For the experimental program, the excitation was applied as (a) harmonic motions and (b) as one of five earthquake ground motions. The authors chose to deliberately select five very different ground motions to observe a range of behaviours in the arch. It was found that the arch was sensitive to the first large impulse in each record; some of the records would fail the arch on the first half cycle of the impulse but many failed the arch on the second half cycle. It was clear in nearly all of the tests that the four-link mechanism was observed before collapse. The important results that came from this work included

- rocking-type failure based on the four-link mechanism governs
- elastic resonance does not occur due to its high frequency (>300Hz) relative to the earthquake input motions
- the analytical model provided accurate failure prediction when using the 'primary' impulse from the earthquake record
- the arches are also more vulnerable to impulse-type ground excitations v) a suite of failure curves was created to identify the failure acceleration for a variety of arch geometries (which was part of the development of an assessment criterion to evaluate safety).

3. Methodology

The methodology adopted for this study has two main parts: first, to characterize the behaviour of an unreinforced arch, and second, to explore options for reinforcing the arch and develop a design guideline for that reinforcement. To achieve the objective of creating the guideline, both experimental and analytical studies will be undertaken; this paper focuses on the first phase which includes shake-table testing of scale models of the arches.

The scale of the models is pre-selected due to the availability of 1/25 scale models created by Lock-Block. Several models were tested, including a 3m and 6m arch, a 6m and 12m dome. This paper deals with the 6m arch. A suite of earthquake records was developed with three criteria:

- to match those used in DeJong et al (2008) for direct comparison,
- from the suite of records used for the BC Seismic Retrofit Guidelines by Pina et al (2013) and
- a selection of worldwide significant events. The records were appropriately scaled for the models used.

The testing is done uni-directionally in the weak direction of the arch. The objective is to identify which parameters they are sensitive to, including but not limited to frequency, displacement, impulses, directionality etc. Each model is tested with each earthquake, at varying levels of intensity until failure is observed. At the failure level the test is repeated at least 3 times to ensure consistency.

A method of externally reinforcing the arch is applied using a tension member. This member is placed along the outer perimeter of the arch, which acts to hold it together during the lateral loading through tension. For these tests, a steel band is used, anchored at either end. The band is instrumented with strain gauges to measure the forces during the shaking. The earthquakes are reapplied to the reinforced model at the previously determined failure level. The recorded force is then said to be proportional to the inertial load that causes the collapse of the unreinforced arch when subjected to the given earthquake. This force can then be used for design by stating it as a fraction of the weight of the arch.

4. Shake-Table Testing

Shake-table tests were performed using a long stroke electrodynamic APS shaker, with a plywood platform attached to the top used as the base for the models. The first course of blocks in the model was fixed at the base. The shaking was in the weak direction of the arch. A high speed camera was used with targets on the model.

4.1. Models

The models are made from 1/25 scale blocks (see Fig. 2). Each block is 6x3x3cm and weighs 85 g, made from Rockite Cement, which is used for patching and is very strong. The advantage of this type of material is that it has a similar density to real concrete, which makes it useful for seismic testing. The Lock-Block products have

a cross-shaped shear key at the top of each block, that fits into the bottom of the above block as seen in the figure.

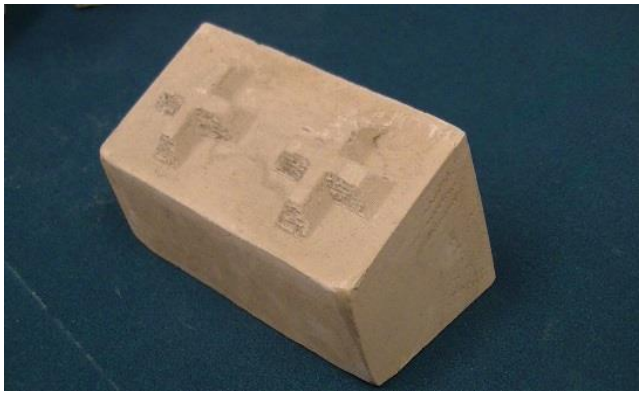

Fig. 2. Small-scale lock block used for the model.

Several models were tested, but the focus of this paper is on the 6m arch, shown in Fig. 3. This model weighs 7kg, is 18cm high and 12cm deep (which uses four full blocks). The interior diameter is 24cm. The first course of blocks was oriented at 90 degrees to the rest of the courses; it was found that this gave the most stable base and allowed for easier assembly of the arch. The first course was held in place on either side by a piece of wood attached to the plywood base.

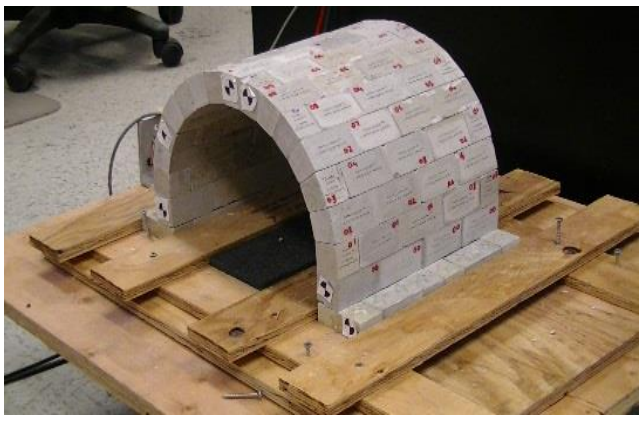

Fig. 3. Shake table testing set up.

4.2. Selected time histories

The total suite of records was approximately 20, which included the study done by DeJong et al (2008), the seismic retrofit guideline records and others. For this first phase 6 records were used. One governing factor in selection of the records was in the physical limitations of the shaker used, particularly with displacements.

Crustal, subcrustal and subduction earthquakes were considered for the selection. Several records, with a considerable difference in their frequency content, maximum acceleration amplitude, maximum displacement amplitude and impulses, are chosen from Pina et al (2013) and PEER Strong Motion database. Table 1 lists the records used. Included is the name, location, year, station name and peak acceleration from that station.

4.3. Scaling of time histories

Time scaling of the records was implemented to account for scale effects between the model and the represented structure. The scaling of this ground motions, as well as, the rest of dimensions involved in this small-scale testing, are based on dimensional analysis described in several studies : Jha (2004), Noam et al (2010), Stojadinovic (2012) and Petry et al. (2012). Following that approach and using the length scale factor of 1/25, the scaling factors are determined as shown in Table 2.

A time scale factor of 1/5 was applied, reducing the duration of the time histories to one fifth of the original durations and increasing the frequencies five times. The accelerations are unscaled.

4.4. Testing procedure

A range of six selected scaled ground motions, calibrated for different intensity levels, are applied to the model in one horizontal direction. The records were repeatedly applied at increasing levels, as a fraction of the record full-scale (referred to in this paper as "Test Level") starting from 40%. Once a failure of the model was observed, the test was repeated three times at the same test level. This was done to check for repeatability.

A total of 80 tests for the unreinforced and reinforced models were run. All tests were recorded with a high-speed video camera at 400 frames per second. A set of targets are attached to the model which allows for the tracking of displacements with the camera software.

4.5. Unreinforced model results

Table 3 summarizes the results of the shake table tests on the unreinforced model. The table shows each applied earthquake and test level; an "O" represents a test where the arch did not collapse, whereas the "X" shows the cases in which collapse occurred. For Tokachi-Oki, Loma Prieta and Tohoku earthquakes tests beyond the failure level were performed.

These tests establish the TL at failure for each earthquake. A study of several relevant parameters was made in an effort to identify the sensitivities of the arch to the different earthquakes. These included peak ground acceleration, velocity and displacement; intensity and duration among others. It was found that in most cases there was not direct correlation or trend to the failures and these parameters. The most consistent result agrees with the work done by DeJong et al (2008, 2010) in that the impulse-type ground motion has the strongest effect; this was observed with the least impulse-like record (Nisqually) having the least effect on the arch.

The rocking type failure based on the four-link mechanism typical of arch structure, as described in (Anshuman, 2004), was seen in all of the tests. A typical collapse of the arch taken from the high speed camera footage is shown in Fig. 4. The hinges were created at the same points for all the earthquakes with the only variation of the collapse direction. One interesting observation from analysis of the collapse videos is that the arch tends to behave in a base-isolated manner with the ground moving much faster than the arch itself; the collapse occurs in a much slower rate once the critical displacement is reached.

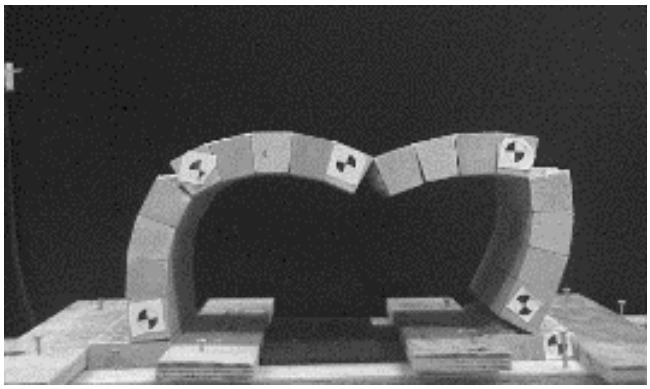

Fig. 4. Typical four-link failure mechanism taken from the high-speed camera footage.

Table 1. Suite of time history records used for the shake table testing.

EARTHQUAKE NAME	LOCATION	YEAR	STATION NAME	PEAK ACC (g)
NISQUALLY	Washington	2001	Seattle (BHD) Z	0.16
TOKACHI-OKI	Japan	2003	Noya (HKD107) EW	0.48
LOMA PRIETA	California	1989	CDMG 57007 Corralitos	0.64
KOBE	Japan	1995	CUE 99999 Nishi-Akashi	0.51
TOHOKU	Japan	2011	TH2011_FKS031_NS	0.42
PARKFIELD	California	1966	CDMG STATION 1014	0.44

Table 2. Scale factors based on dimensional analysis.

	LENGTH SL	TIME St	FREQUENCY Sf	ACCELERATION Sa
Dimension	L	T	T-1	LT-2
Relation to length factor	N/A	$\sqrt{1/S_L}$	$\sqrt{S_L}$	$S_L * \left(\sqrt{1/S_L}\right)^2$
Value	1/25	1/5	5	1

Table 3. Summary of performed shake-table tests on unreinforced model.

EARTHQUAKE	TEST LEVEL (TL)							
	40%	50%	60%	70%	80%	90%	100%	120%
NISQUALLY			O	O	O	O	O	X
TOKACHI-OKI	O	O	O		O	X	X	
LOMA PRIETA	X	X	X					
KOBE	X							
TOHOKU	X		X					
PARKFIELD	O		O	O	X			

5. Externally Reinforced Model

From the tests on the unreinforced model, it was clear that the model would not survive most earthquakes. There was however, significant variability in the failure level, from very low, to almost 100% of the design level. There are many possible ways to stabilize the model, but the simplest and most reliable is add an external tension reinforcement around the arch.

From the unreinforced tests, it was apparent that the arch tends to fail in the same location each test, with three hinges opening in the arch (plus two at the base). The collapse occurs once the hinges open to a critical displacement level. It then leads that preventing the hinge from opening will prevent the collapse; this can be done is several ways:

- Application of epoxy between the blocks – this would likely present a failure in tension of the concrete since the epoxy strength is quite high.
- Use an externally bonded type reinforcement (such as FRP's) that can be placed at each of the hinge locations – care must be taken to select locations in order to prevent other hinges from opening.
- Use a continuos non-bonded tension reinforcement anchored at the ends.

The second is possibly the most effective, since it allows reinforcement at the hinge locations directly, however the third is the simplest to apply and was used in this study.

For these tests, a steel strap was added to the outside of the arch, anchored at each end (which capability to tighten at one end) and positioned at the midpoint of the depth of the arch. In the full scale application, a variety of materials, dimensions and arrangements can be used. For the scale model tests, the material and dimensions were specifically chosen in order to achieve a measureable strain based on the expected levels of force.

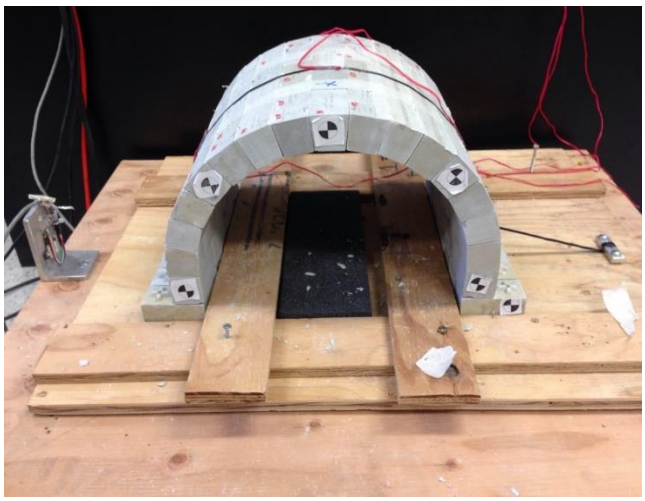

Fig. 5. Instrumented steel band reinforcing the arch model.

The material for the reinforcement was a 1095 spring steel strap, 6.35mm wide and 0.127mm thick. These dimensions provided the smallest cross sectional area for the strap out of the available materials. The strain gauges had the ability to register changes in strain of 1με and the estimated applied force of the model was 1-2lbs. Material calibration was performed by adding 1kg masses to the steel strap which was oriented in a vertical position. Additional 1kg masses were attached to increase the applied strain linearly. Approximate strain due to 1kg was 66με. The elastic modulus of the material was calculated to be approximately 212.2Mpa.

5.1. Reinforced arch model results

From a qualitative point of view, the steel band reinforcement prevented failure in any of the applied tests. This is expected and in itself is not conclusive since a single band may not perform as well with multi-directional shaking; however, it does prove the concept in principle. The applied tests are shown in Table 4.

Two main observations can be made from the results of the reinforced arch tests. First, hinges can be observed by a slight separation between the blocks at the same location as the unreinforced model. This effect is shown in Fig. 6 with the circles showing the hinges. It is worth noting that the appearance of the hinge on the outer edge is dependent on the tension of the band (ie. the more tension the smaller the hinge) and that the inner hinge cannot be easily controlled by the tension band, which brings into consideration the earlier point of using bonded reinforcement at the location of the hinges.

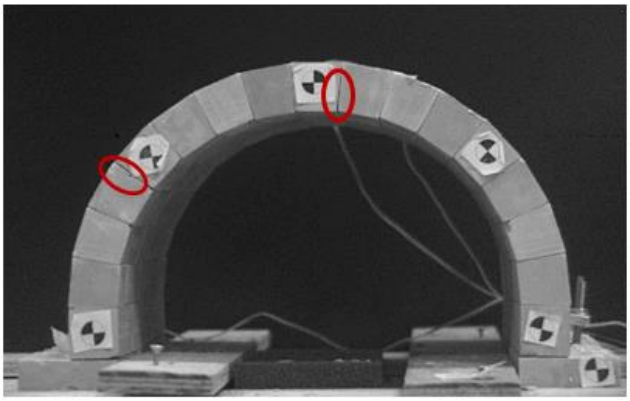

Fig. 6. Reinforced arch with hinges shown taken from the high speed camera footage.

The second observation was that the recorded forces appeared to be consistently lower than what was expected, by as much as 50% (approximately 1lb maximum). It was expected that the tension band would take a majority of the inertial force that results in the collapse of the arch. One possible explanation is that by holding the arch together during shaking, the arch maintains much of its primary load paths in compression for the additional lateral load. Additional shake table tests will be done including multi-directional; and an analytical model will be created to further study the load paths and their effects.

6. Conclusions

Lock Block Ltd. has created arch and dome structures based on their patented interlocking block system. This study examines the seismic performance of the arch structures by shake-table testing of scale models of the arches.

A suite of six time-scaled records was used and applied to a scaled 6m arch. The records were applied at increasing levels of intensity until collapse occurred. It was seen that the collapse followed the typical four-link mechanism with the hinges opening at the same location in each case.

A steel band was attached to the model to act as external tension reinforcement. The band was instrumented with three strain gauges. All of the tests applied to the unreinforced model were applied at the failure level were applied to the reinforced model; in each case the model survived.

Small openings between blocks were observed in the reinforced model which indicated that the same hinges were formed and that the arch maintained the four-link mechanism even without failure. The tension forces in the band were very low and typically about half of what was expected.

Further studies will be done, including using larger models, expanding the suite of records used, and creation of an analytical model to study the load paths in detail and to examine various factors including multi-directional loading and boundary conditions.

Table 4. Summary of performed shake-table tests with reinforced model.

EARTHQUAKE	TEST LEVEL (TL)							
	40%	50%	60%	70%	80%	90%	100%	120%
NISQUALLY							O	O
TOKACHI-OKI					O	O		
LOMA PRIETA	O							
KOBE	O							
TOHOKU	O							
PARKFIELD					O			

Acknowledgements

The authors would like to thank the contribution of Mr. Scott Jackson and Mr. Jermin Dela Cruz of UBC for setup and running the shake-table tests; and Mr. Bryn Wong for helping with the data analysis and experimental testing. The authors would also like to thank Mr. Brent Wallace and Mr. Arley Drew from Lock-Block Ltd for their assistance with the project.

References

Anshuman JHA (2004). Dynamic Testing of Structures Using Scale Models. Thesis in The Department of Mechanical and Industrial Engineering at Concordia University, Montreal.

Dejong MJ, Delorenzis L, Adams S, Ochsendorf JA (2008). Rocking stability of masonry arches in seismic regions. *Earthquake Spectra*, 24(4), 847-865.

Dejong MJ, Ochsendorf JA (2010). Dynamics of in-plane arch rocking: an energy approach. In: *Proceedings of the Institution of Civil Engineers*, 179-186.

Delorenzis L, Dejong MJ, Ochsendorf JA (2007). Failure of masonry arches under impulse base motion. *Earthquake Engineering & Structural Dynamics*, 36, 2119-2136.

Noam T, Dolinski M, Rittel D (2010). Scaling Dynamic Failure: A Numerical Study. Faculty of Mechanical Engineering, Technion, Israel.

PEER (2011). Pacific Earthquake Engineering Research Center, *http://peer.berkeley.edu*.

Petry S, Beyer K (2012). Testing unreinforced masonry structures at reduced scale. *Proceedings of 15th WCEE*. Lisboa.

Pina FE, Ventura CE, Taylor G, Liam Finn WD (2013). Selection of Ground Motions for the Seismic Risk Assessment of Low-Rise School Buildings in South-Western British Columbia, Canada. Seismic Retrofit Guidelines 2nd Edition. Manual Volume 5, Appendix F.

Shapiro EE (2012). Collapse Mechanism of Small-Scale Unreinforced Masonry Vaults. Massachusetts Institute of Technology.

Stojadinovic B (2012). Hybrid Simulation: Basics and Similitude. Workshop slides. University of California, Berkeley.

Challenge Journal of Structural Mechanics

Vertical and lateral horizontal forces of walking area running pedestrians

Shota Urushadze *, Miroš Pirner

Institute of Theoretical and Applied Mechanics, Academy of Sciences of Czech Republic, v.v.i.Prosecka 76, 190 00 Prague, Czech Republic

ABSTRACT

The authors have noticed the newest observations and few analysis of excitation mechanism. Therefore they prepared the series of vertical and lateral forces measurements due to steps of walking, running persons on horizontal plane, on inclined plane and on stairway. They suppose that the import knowledge of the forces frequencies of step or strides for different walking velocities is the most important for the further analysis and analysis of the mechanisms. The time histories of lateral forces of a pedestrian were registered and statistical analyzed: the authors received the lateral force dependence on the walking velocity, on stride length an on the weight of pedestrian. The new research step is focused on lateral horizontal forces.

ARTICLE INFO

Article history:
Received 12 February 2016
Accepted 2 March 2016

Keywords:
Stride strength
Stride frequency
Step frequency
Dynamic coefficient
Effects of striding velocity

1. Introduction

ITAM investigated a large number of footbridges and asserted that these constructions were very sensitive to pedestrians' movements as their Eigen frequencies were close to the step frequencies of pedestrians due to the light weight of the footbridges investigated.

The older research focused on the magnitude of the vertical component of the stride strength and its dependence on various speeds of movement and step lengths.

2. Dynamic Load

The dynamic load has at least three components – one vertical, two horizontal and in the case of a curved pedestrian movement, one torsion component (Harper, 1962).

2.1. Vertical dynamic load

At first we deal with the most important one, i.e. the vertical. The dynamic load is expressed by the dynamic coefficient for a single person

$$\delta_p = \frac{max F_{dyn} + F_{stat}}{F_{stat}}, \quad (1)$$

and for a group of people

$$\delta_{pc} = \frac{max \sum F_{dyn} + \sum F_{stat}}{\sum F_{stat}}, \quad (2)$$

where

F denotes strength.

The sum $\sum$ runs over all the strengths at a given time t which is chosen in such a way that δpc is maximal.

We have also denoted by *stat*, respectively *dyn* the static, respectively dynamic parts of strengths.

2.1.1. A single pedestrian

a) A pedestrian on a horizontal plane

The vertical component of the strength reaches its maximum if the center of mass of the pedestrian is at its maximum over the horizontal plane. The so-called saddle point between two peaks (see Fig. 1) is the occasion when the center of mass is at its minimum, i.e. the pedestrian's two legs pass each other. If the pedestrian walks fast or runs, the saddle point does not occur and the two peaks merge (see Fig. 2).

In the figure, time is on the horizontal axis and the dynamic coefficient δ_p is on the vertical axis. We denote the duration of stride by t_k and duration of step by t_s. The speed of walking is 1.1 ms^{-1}. The intersection of the

* *Corresponding author*. Tel.: +420-222-363-071 ; Fax: +420-286-884-634 ; E-mail address: urushadze@itam.cas.cz (S. Urushadze)
ISSN: 2149-8024 / DOI: http://dx.doi.org/10.20528/cjsmec.2016.03.006

pressure functions (of time) of the left and right leg is the moment when both legs are touching the plane.

According to our measurements, the borderline between walking and running lies somewhere between 1.4 and 1.8 ms^{-1}; according to (Footbridge, 2002) and (Bachmann and Ammann, 1987) between 1.5 and 2.35 ms^{-1}. It appears in the series of subsequent strides in the way that the end of one stride and the beginning of the next one merge at one point (in the graph).

We have measured the walking of ten men and two women and can confirm that every individual has its own characteristic "handwriting" of walking.

In Fig. 3 we see the dependence of the dynamic coefficient δ_p on the step frequency $f_s = 1/t_s$ and stride frequency $f_k = 1/t_k$. The datasets are interpolated by polynoms through their means (dashed line) and through their maxima (full line).

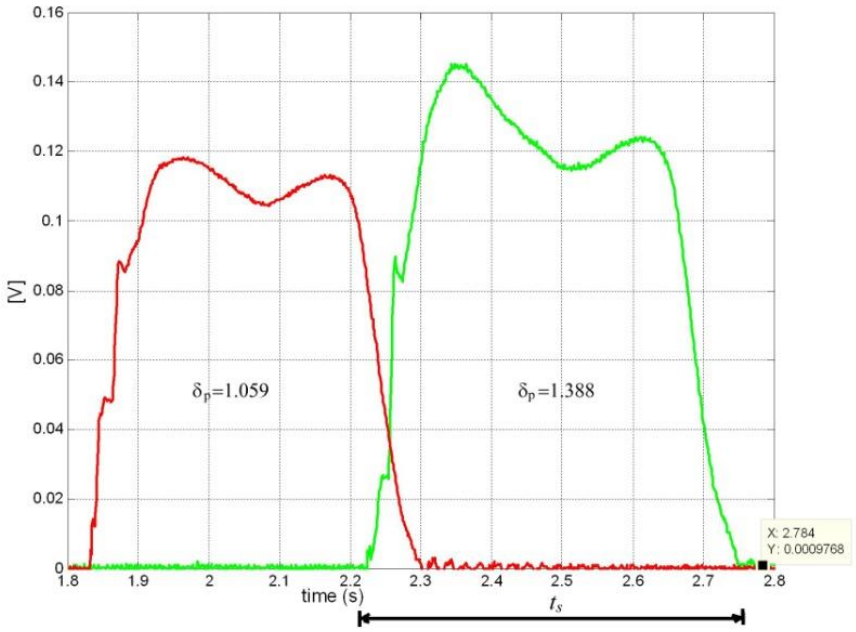

Fig. 1. Time histories of the left and right leg.

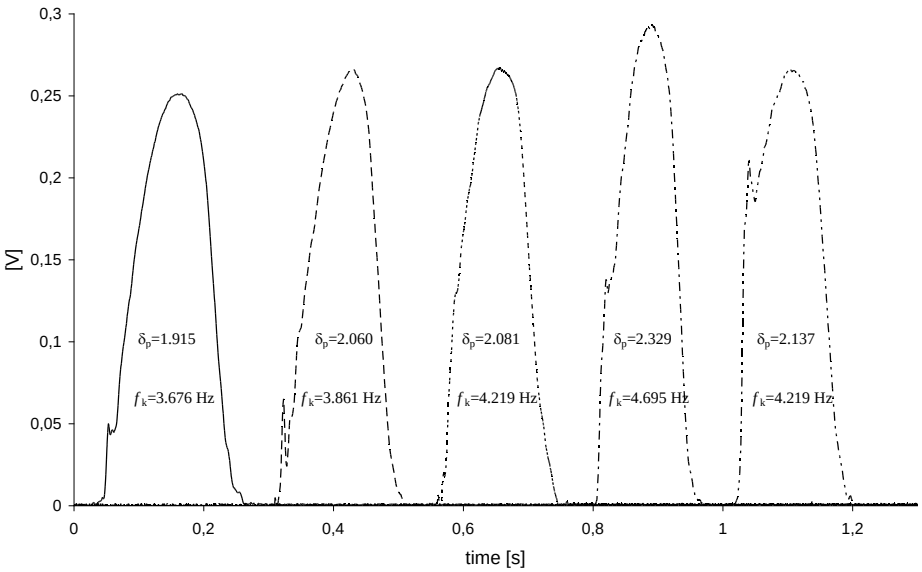

Fig. 2. An example of 5 strides when running (speed 3.4 ms^{-1}).

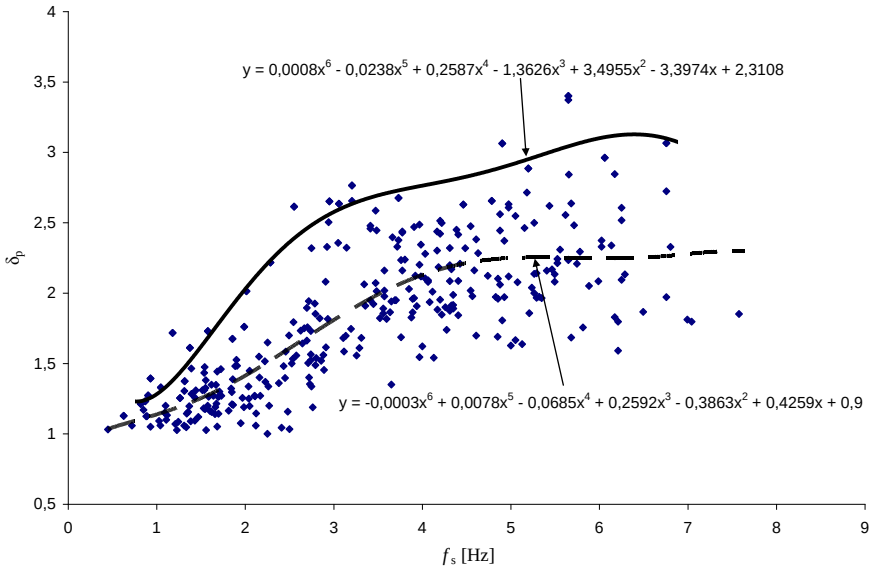

Fig. 4. The dynamic coefficient δ_p versus step frequency f_s.

In Fig. 4 we see the dependence of the step frequency f_s and the stride length l_k on the stride frequency f_k. From this dependence we can derive an approximate relation between f_s and f_k

$$f_s \doteq 1{,}28 f_k \,. \tag{3}$$

Furthermore, the relation between the stride length l_k and f_k can be derived from that dependence.

In Fig. 5 we see the dependence of the dynamic coefficient δ_p and the striding velocity on stride frequency. It is apparent from this figure, which contains all the records of the individuals tested, that the aforementioned dependencies have a large variance; in spite of that it was possible to establish an approximate relation between the striding velocity $\dot{v}$ [m/s] and the step and stride frequencies

$$\dot{v} \doteq l_k * f_k \,, \tag{4a}$$

$$\dot{v} \doteq 0{,}8 f_k \doteq 0{,}6 f_s \,. \tag{4b}$$

The relations (3) and (4) do not capture any differences between men and women due to their approximate nature.

The relations (3) and (4) do not capture any differences between men and women due to their approximate nature.

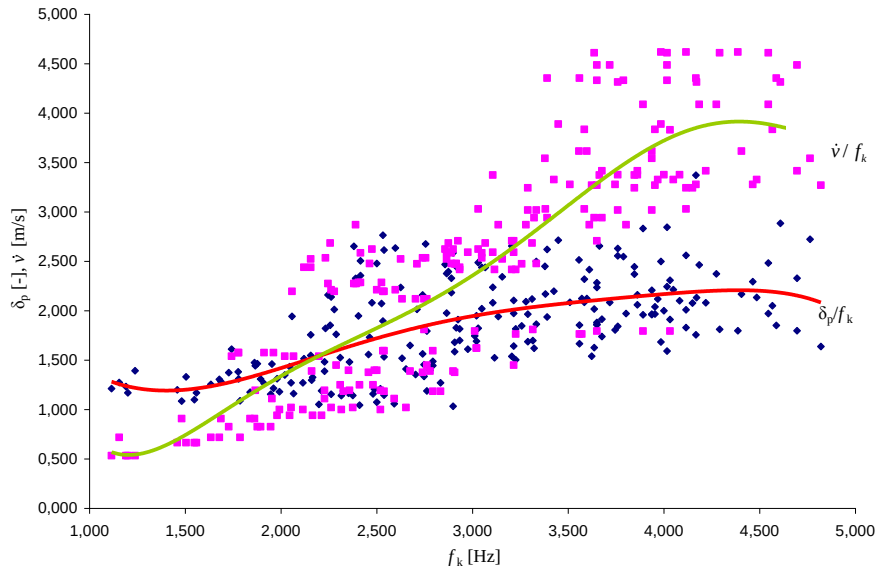

Fig. 5. The dependence of dynamic coefficient δ_p on stride frequency f_k and striding velocity $\dot{v}$ on stride frequency f_k.

b) A pedestrian on an inclined plane

The next part of the experimental investigation was a measurement of the dynamic characteristics (δ_p, f_s, f_k, l_k) for walking on an inclined plane. The selected slopes for experiments were (in percentage) 16%, 21.2%, and 33%.

In Fig. 6 we see the dependence of dynamic coefficient δ_p on the step frequency fs when the length of one step is 80 cm; it is obvious that if the slope is more than 16% the pedestrian is more careful, i.e., her dynamic load is smaller. Polynomial curves represent probable dependencies of the quantities involved.

Some of the results obtained:

- The vertical component of the strength as a function of time is roughly similar to the corresponding function in the case of the horizontal plane, i.e., they have two peaks for striding velocities $\dot{v} = 0.8 \div 1.5$ ms^{-1} (the first one is usually higher than the second one when walking down and other way round when walking up), if the pedestrian walks quickly or runs they merge into one peak.
- "Decrease" of the dependence δ_p / f_s at $f_s \cong 3.5$ Hz occurs only if the slope is equal to 16%.
- The rate of frequencies f_s, and f_k, is more complicated – it differs from the formula (4b) which is valid for the horizontal plane only. The results of measurement are shown in table 1. It is apparent that the rate is higher when walking up. The slope and stride length have only minor effects.
- The rate of $\dot{v}$ and $\oslash f_s$ is $\dot{v} / \oslash f_s = 0.59 \div 0.86$ [m]; it was impossible to obtain more precise information from the measured values.

Note: The striding velocity of the pedestrian $\dot{v}$ is measured in direction of the inclined plane.

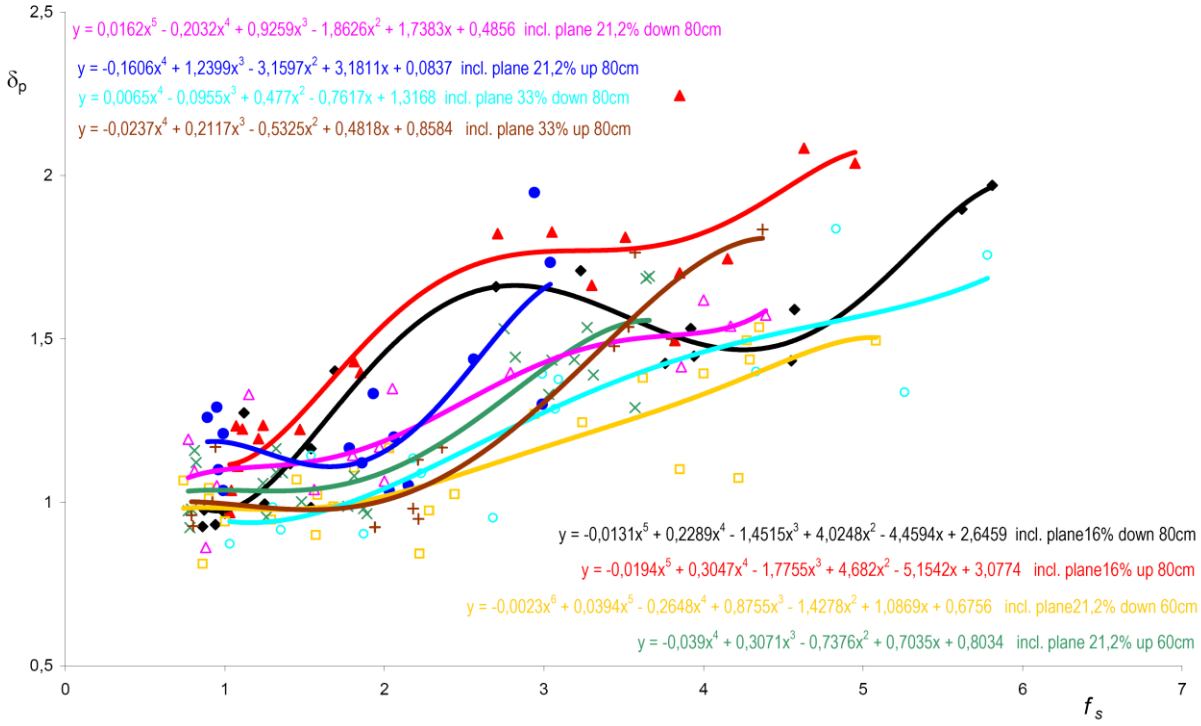

Fig. 6. The dynamic coefficient δ_p versus frequency f_s – inclined plane.

Table 1. Rate $\oslash f_s / \oslash f_k$ as a function of stride length, slope of the ground, and walking direction.

stride length 80 cm slope 16%		stride length 60 cm slope 21.2%		stride length 80 cm slope 21.2%		stride length 80 cm slope 33%	
up	down	up	down	up	down	Up	down
0.935	1.040	0.809	0.907	0.856	0.921	0.893	1.053

c) A pedestrian on a staircase

A staircase can be a part of a footbridge. This is why we have measured dynamic effects of a pedestrian on stairs when he or she moves up and down.

In Fig. 7 we depicted the dependence of the dynamic coefficient δ_p on the step frequency f_s.

From the measurement results it follows:

- men cause more dynamic effects when walking downstairs than upstairs
- women are more careful and when they walk downstairs they cause less dynamic effects than when they walk upstairs
- no effects of the height of heels (worn by women) were observed.

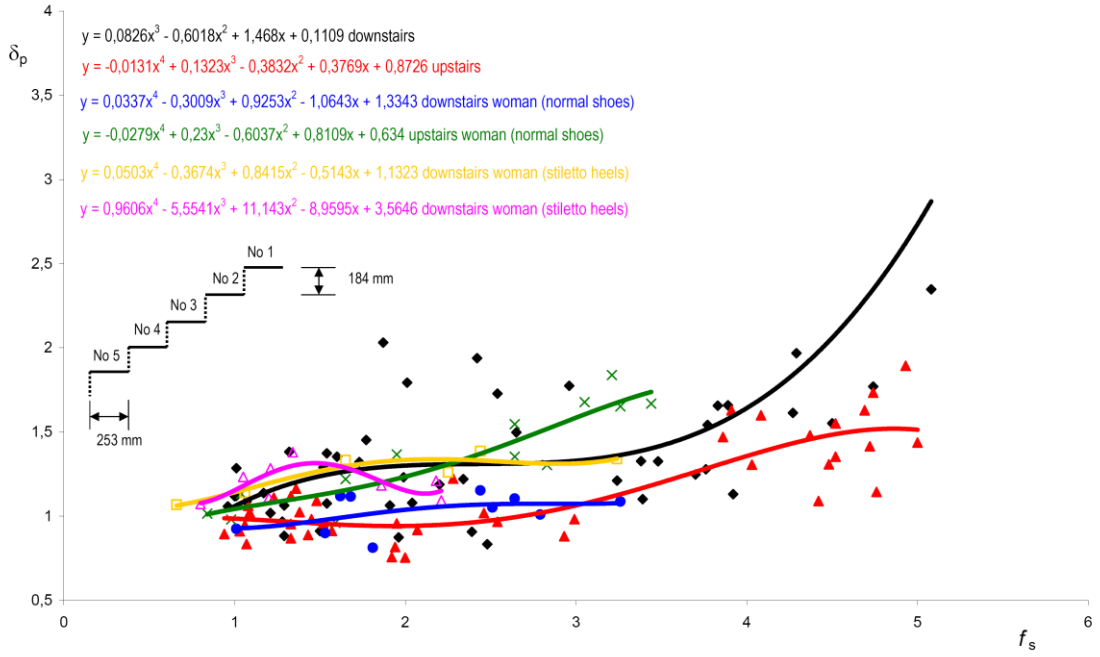

Fig. 7. The dynamic coefficient δ_p versus frequency f_s .

The bar chart for slow walking has a similar shape as seen in Fig. 1 for footsteps on a horizontal plane. For fast walking, the two peaks in the bar chart merge.

Some of the results:

- the rate of frequencies f_s, and f_k for striding velocities $0.25 \div 0.8$ ms^{-1} is

$$\varnothing f_s / \varnothing f_k = 0.77 \; to \; 1.19 \; . \qquad (5)$$

- the rate of striding velocities ($0.25 \div 0.8$ ms^{-1}) to the average step frequency f_s is $\dot{v} / \varnothing f_s = 0.24 \div 0.8$ m.

2.1.2. A group of pedestrians on a horizontal plane

We have investigated the vertical components of the strength exerted by a group of pedestrians because of our search for a theoretical expression of load and response of a footbridge in both synchronous and asynchronous cases. We have used five pedestrians walking side by side and in a variant setting three pedestrian side by side and two behind them (Fig. 11b showing the horizontal projection of sensors).

In both cases the distance between two outer sensors was 2 m, corresponding to the width of the footbridge between guardrails of 3 m. The "density" of pedestrians was 0.9 [person/m^2].

The Fig. 8a contains the record of vertical components of strengths exerted by five pedestrians when they walk with the velocity $\dot{v}$ =1.4 ms^{-1} (the latter variant with 3 pedestrians in front and 2 behind them; Fig. 11b).

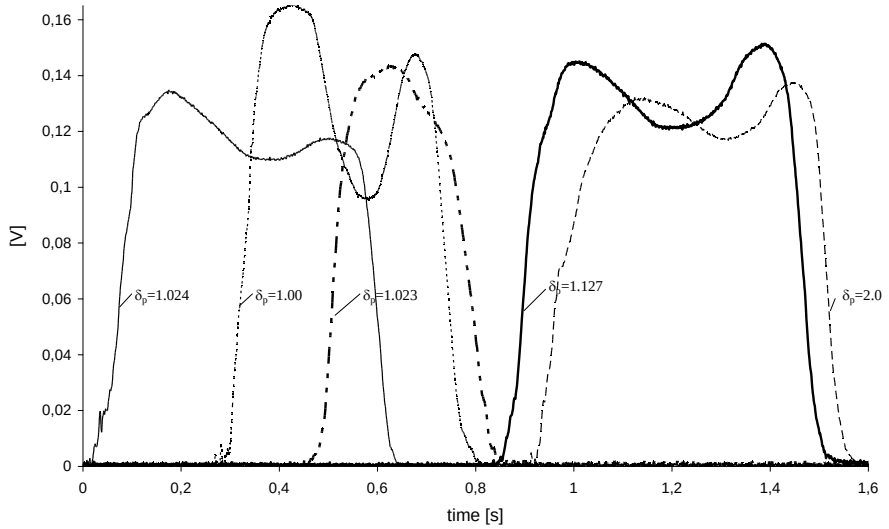

Fig. 8a. The vertical forces of five persons; $\dot{v} = 1.4 \; m/s$; the sensors were located as in Fig. 11b.

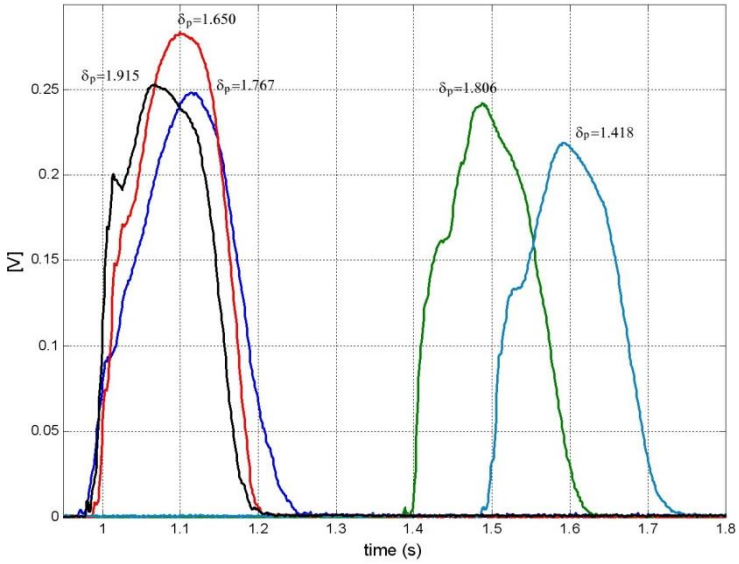

Fig. 8b. The vertical forces of five persons; $\dot{v} = 2.85\ m/s$; the sensors were located as in Fig. 11b.

The Fig. 8b shows the record of vertical components of strengths exerted by five pedestrians when they walk with the velocity $\dot{v} = 2.85$ ms-1 (the latter variant with 3 pedestrians in front and 2 behind them; Fig. 11b).

The Fig. 9a shows the record of vertical components of strengths exerted by five pedestrians when they walk with the velocity $\dot{v} = 1.5$ ms^{-1}, the Fig. 9b shows the situation with the velocity $\dot{v} = 3.2$ = 3.2 ms^{-1}. The setting of sensors was in agreement with the situation depicted in the Fig. 11c.

The dependencies of the dynamic coefficient δpc on the step frequency fs for 2, 3, 4 and 5 people side by side, respectively is shown in the Fig. 10a.

A decrease of δpc with the number of pedestrians reveals the Fig. 10b

Note: Due to the absence of a simultaneous stride in the situation with many pedestrians walking under normal conditions (in our case 5) the dynamic coefficient $\delta pc < \delta p$; the evidence of that is seen in Fig. 3 (mean values) and Fig. 10b.

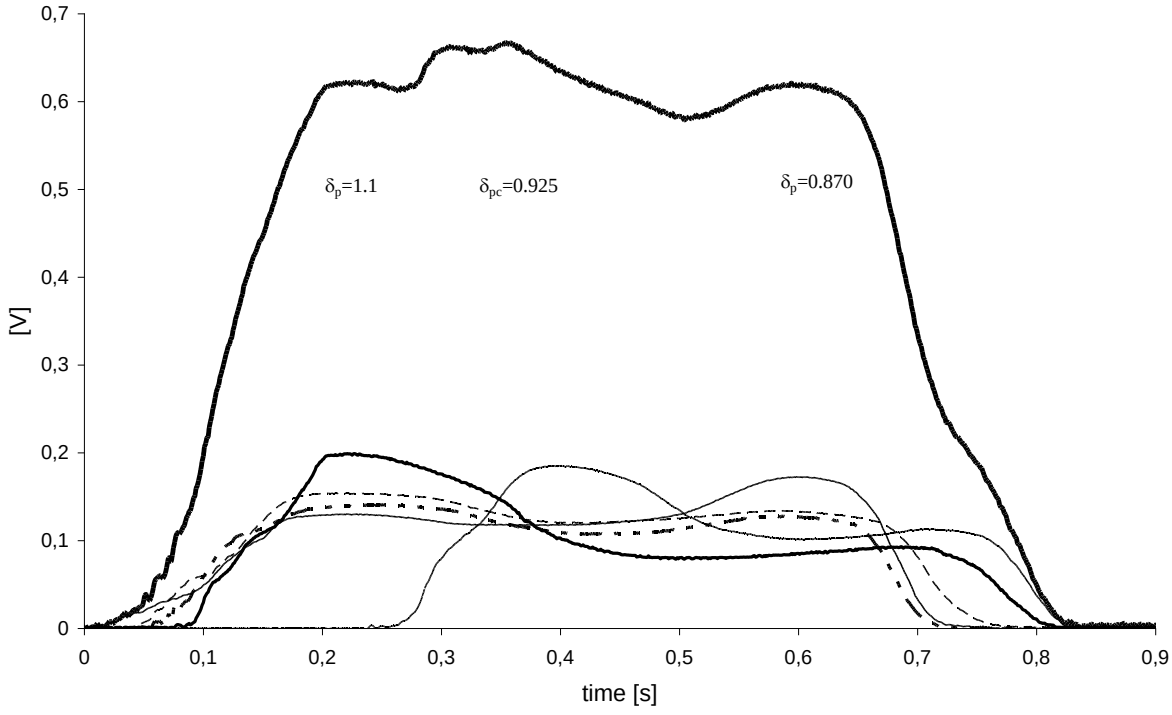

Fig. 9a. The vertical forces of five persons; $\dot{v} = 1.5\ m/s$; the sensors were located as in Fig. 11c. The symbol δ_{pc} = dynamic coefficient of all persons.

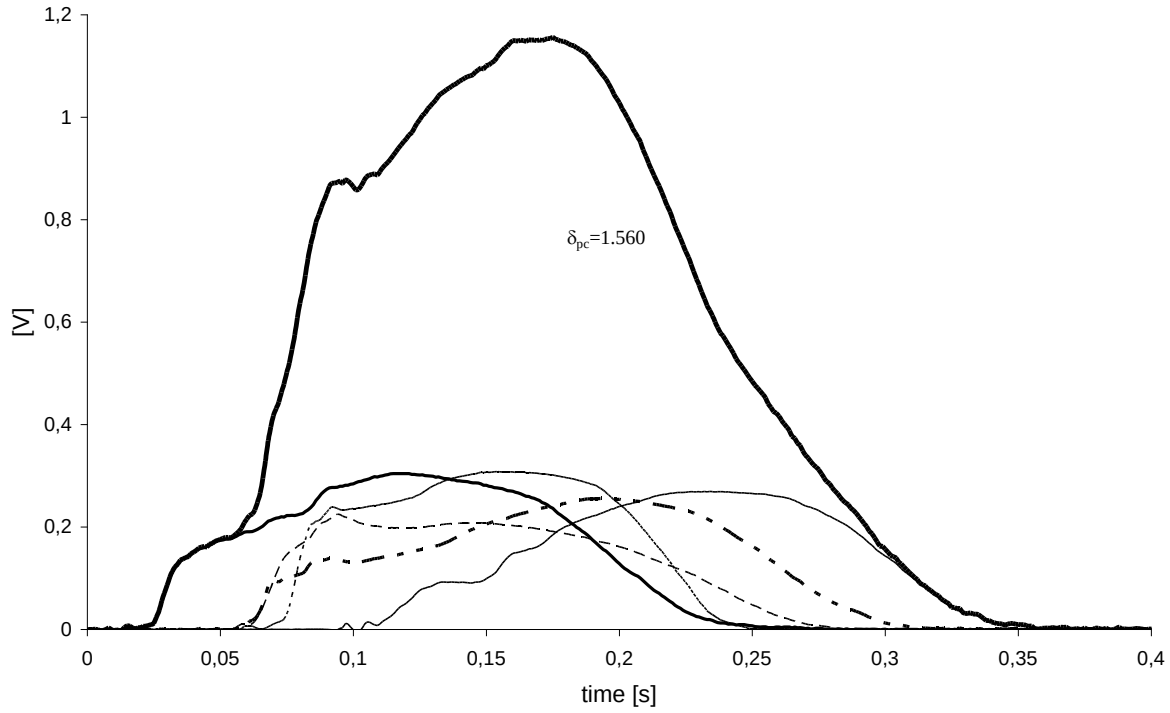

Fig. 9b. The same conditions as in Fig. 11c, but$\dot{v} = 3.2\ m/s$.

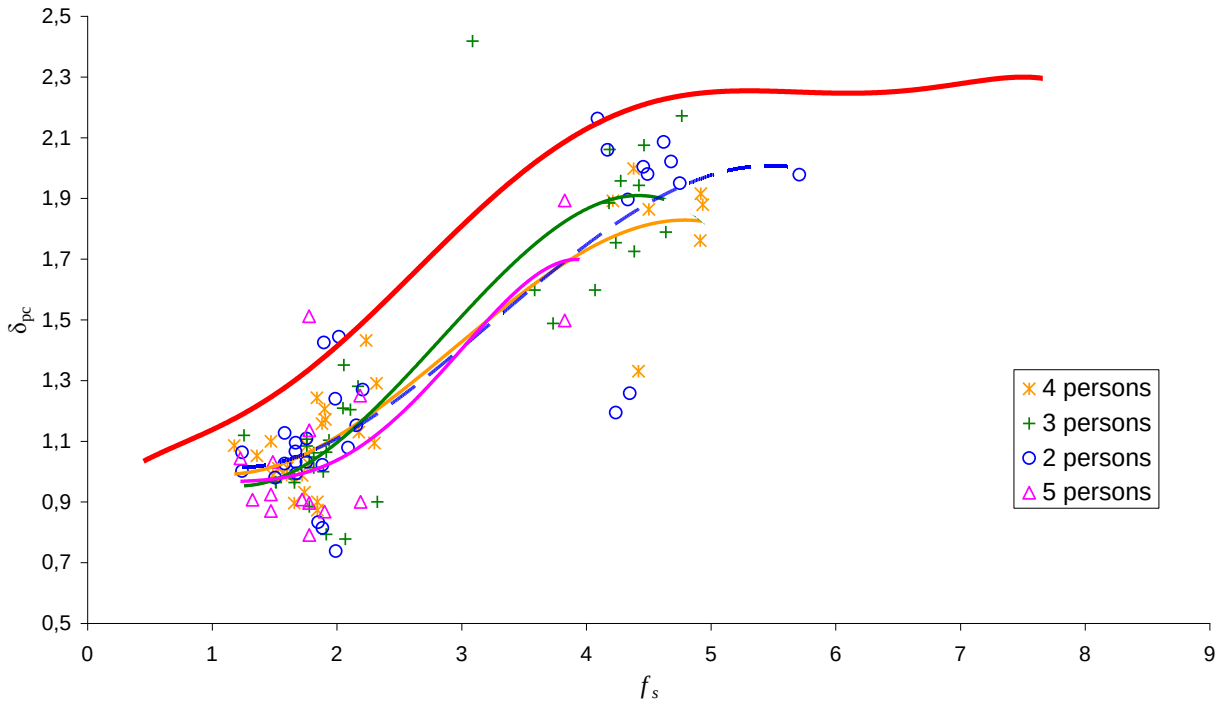

Fig. 10a. The dependencies of the dynamic coefficient δ_{pc} on the step frequency f_s for 2, 3, 4 and 5 people side by side, respectively.

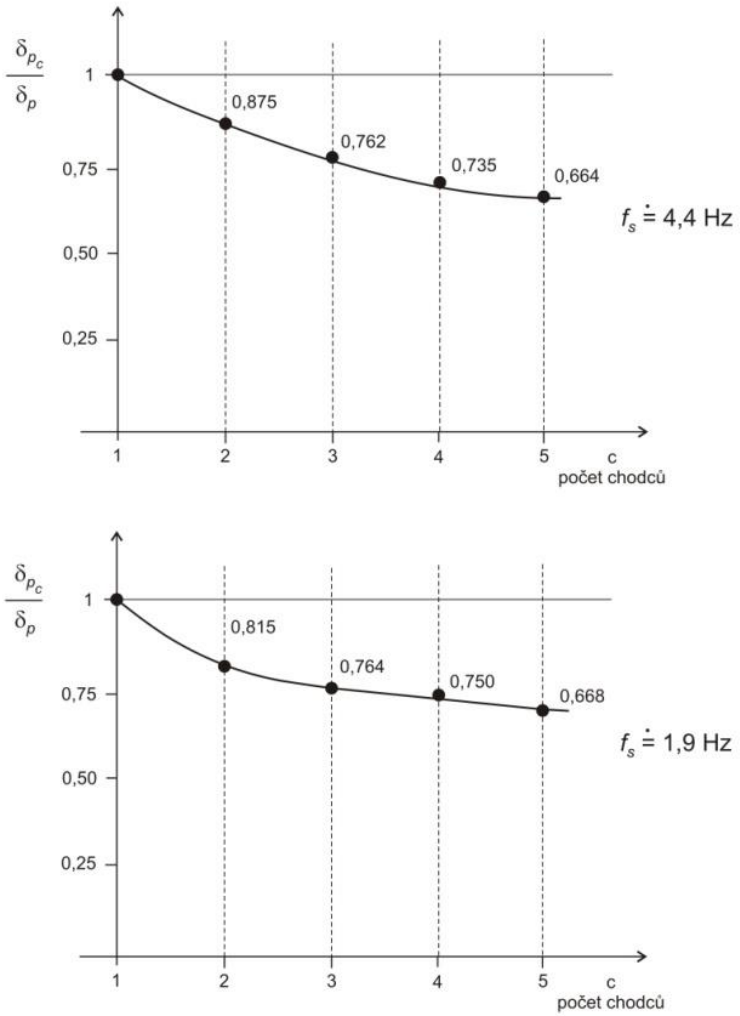

Fig. 10b. The dependence of the dynamic coefficient δ_{pc} on the number of pedestrians.

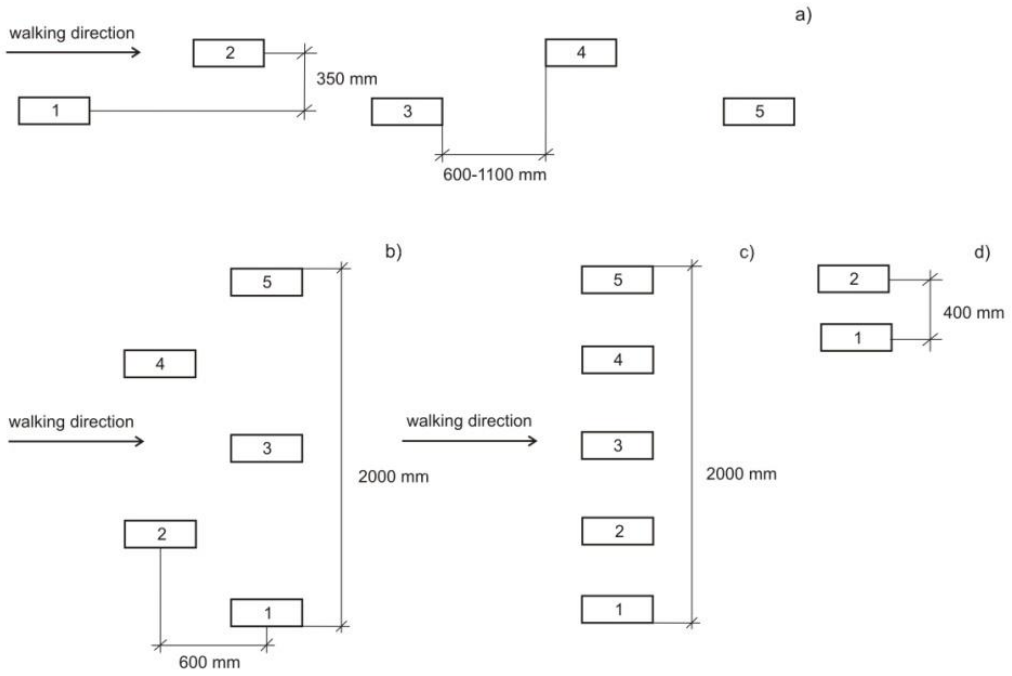

Fig. 11. The positions of sensors; (a) in the case of a single-person-walk; (b) and (c) in the case of five people walking; (d) for a vandal.

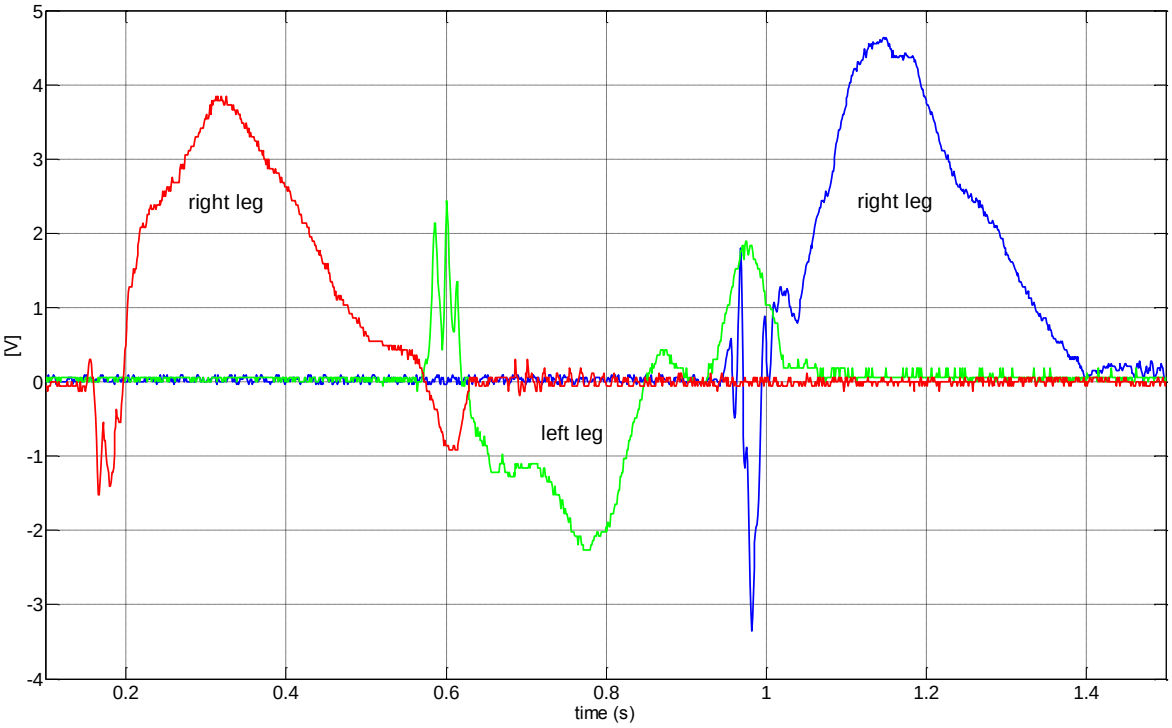

Fig. 12. Typical time histories of horizontal lateral loads.

2.1.3. Sensors of the vertical stride strength

The sensor is a steel plate, 5 mm thick, 395 mm long and 150 mm wide, supported on short sides as a simple beam. The deflection stress was measured by a strain gauges. The eigenfrequency of an unloaded sensor is 143 Hz and the logarithmic decrement of amplitude is $\vartheta \doteq 0.3$; also its eigenfrequency is sufficiently different from a step frequency. The deflection stress did not exceed 120 MPa. The positions of sensors are depicted in the Fig. 11.

2.2. Lateral horizontal load

The lateral horizontal force depends on the weight of pedestrian on the speed of the walking and on the length of the stride.

On Fig. 12 are typical time histories of horizontal lateral loads (right, left, right leg); Harper described the shape with two peaks in (Footbridge, 2002).

2.3. Sensors of the lateral horizontal load

The sensor is the series of three steel strips, 370 mm long, 30 mm wide, supported by boundary box. The defection stress of steel strips was measured by strain gauges. On the top of steel strips is the plate from soft material, which guarantees the participation of all strips. On the Fig. 13 is the relation between Volts and the lateral horizontal load. The sensor is shown on Fig. 14. On Fig. 15 is the position of sensors.

In Fig. 16 are results of our experiments. The weights of pedestrians was from 700 N up to 1125 N and the walking speed from 0,45 m/s up to 1,44 m/s (from 1,6 km/h up to 5,1 km/h)

3. Theory and Empirical Formula

3.1. The dynamic load in the vertical direction

3.1.1. Load exerted by a single pedestrian deterministically expressed

There is a reliable formula for the dynamic increment (Footbridge, 2002) for $N = 20 \div 25$

$$F_{dyn} = c_z * N * \alpha * m_p * g\,, \tag{6}$$

where c_z is the correlation coefficient (≈ 0.2) expressing the synchronization of steps with footbridge movements,

N – the number of pedestrians

α – the dynamic coefficient of steps (α = 0.2÷0.5 for walking, α = 0.6 ÷ 1.4 for running)

m_p*g = gravity force of a pedestrian.

3.1.2. Load exerted by a continuous stream of pedestrians deterministically expressed

Measurements of the vertical response have confirmed that the vertical components of the strengths have themselves two components in time: nonstationary and a stationary one. In case of the damping value $\xi = 0.015$ (a common value) and the stride frequency $f_k = 2$ Hz, the maximal amplitude of the response occurs only after 60 steps (i.e., about 30 seconds after entering the footbridge), while 60% of the response occurs after 10 steps and 85% after 20 steps. Consequently, the nonstationary component is not important for long footbridges (Stoyanoff, 2002).

Let us assume that the continuous stream of pedestrians is formed by rows of 5 pedestrians (across the footbridge deck 3500 mm wide) which are $d = 0.6 \div 1$ m apart (it may be even more according to the step velocities). Let us moreover assume in agreement with Fig. 9a and 9b that pedestrians' strides in a row are simultaneous. Time shifts of six rows are expressed by a phase shift φ, which may be chosen for example as six multiples of 30 degrees between 0 and 180 degrees randomly attributed while the phase shifts of the first six-pack are denoted by φ_1 to φ_6, of the next one φ_7 to φ_{12} etc.; the next rows of pedestrians follow till they fill up the whole footbridge deck. A scheme of the loading by six rows of pedestrians in time is drawn in Fig. 17; for better comprehension we have used an axonometric projection and time functions are plotted in coordinate systems with time axes perpendicular to the axis of the footbridge – we have limited ourselves to three such functions, only.

The vertical component of the strengths can be computed as

$$F_i(t) = F_i * \delta_{pc}|sin(\omega_i t + \varphi_i)| \ , \tag{7}$$

where ω_i is an angular step frequency of the i^{th} row of pedestrians.

Eq. (7) means that we deal with a standing system of varying loads instead of a continuous moving stream of pedestrians.

Then solving the response of a footbridge is a matter of routine.

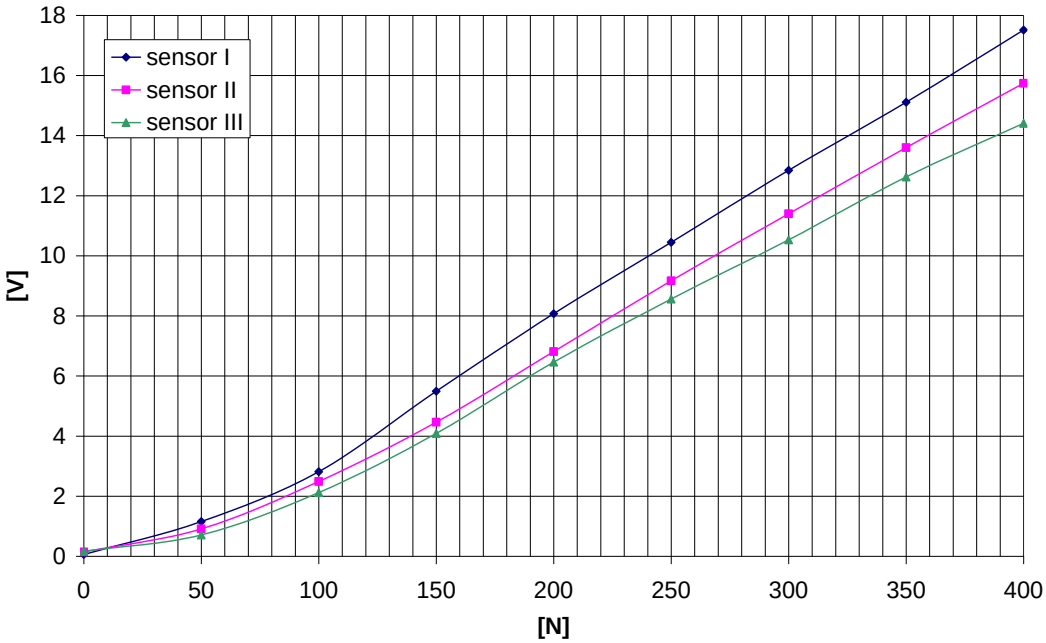

Fig. 13. Relation between Volts and the lateral horizontal load.

Fig. 14. The sensor.

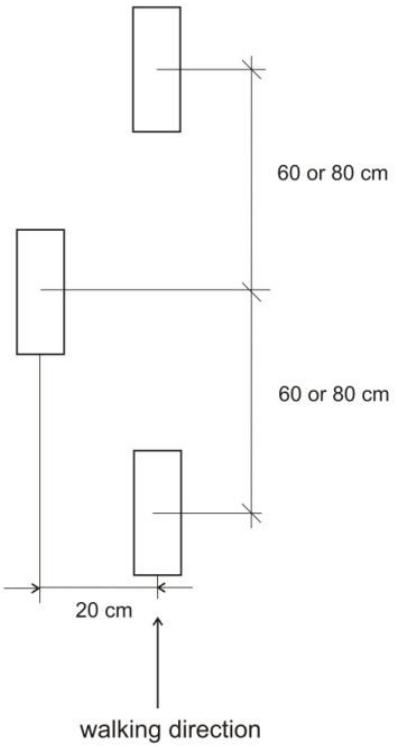

Fig. 15. Sensors positions for lateral horizontal loads.

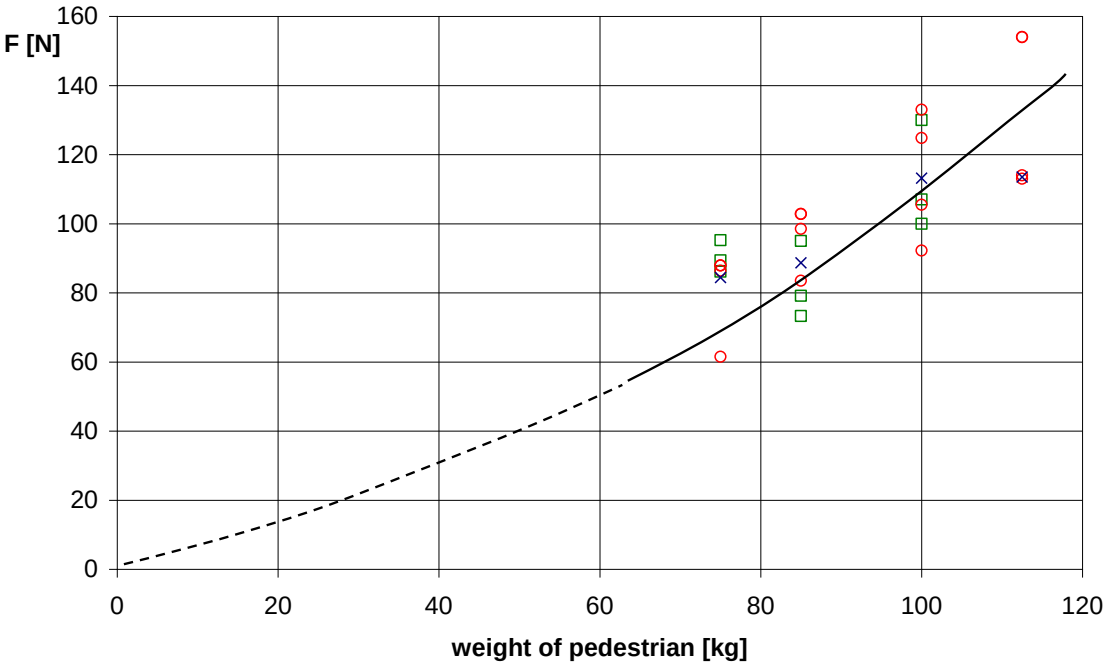

Fig. 16. Relation between weight of pedestrian and lateral horizontal load.
○ – *stride length 60cm,* □ – *stride length 80cm,* × – *the mean value*

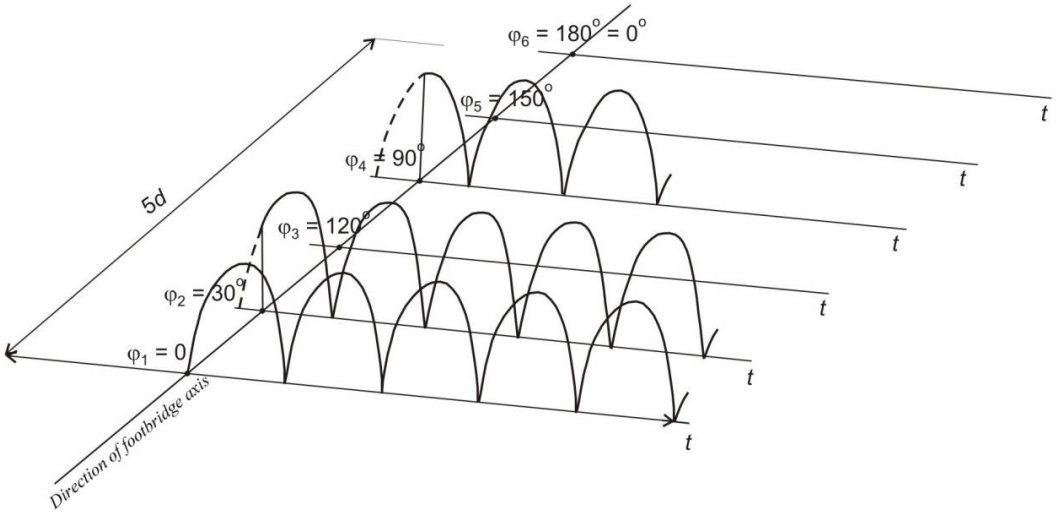

Fig. 17. Six rows of pedestrians.

3.1.3. Vandals

Footbridges, due to their small bending resistance in the vertical direction, tempt vandals to cause them to vibrate abnormally. The region of the lowest bending eigenfrequencies contributes to it, as they can be easily achieved by knee bends. Nevertheless, there is no danger of vibrations caused by a larger number of people, since it has been tested that they could not keep their knee bends in phase; but if there are just three to five of them they can succeed in coordinating their movements so that the load causing its response can exceed the acceptable vibration rates of other pedestrians; in exceptional cases the construction can be damaged.

Tests with sensors, described in section 2.3, have been conducted in the laboratory of the ITAM; loads have been represented by one test person (a subtle vandal, respectively a heavy one) who repeated knee bends in the frequency range 0.6 ÷ 4.5 Hz. In the case of frequencies under 0.6 Hz the dynamic coefficient of a vandal δ_v is small and the frequencies over 4.5 Hz cannot be achieved by human knee bends.

The dependence of the dynamic coefficient of a vandal δ_v on the knee bending frequency f_v with an idealized time function $F_{vandal}(t)$ is plotted in the Fig. 18.

Assuming that the movement connected with a knee bend is very close to a harmonic movement, the load in a suitably chosen spot on the footbridge can be computed as

$$F_{vandal}(t) = F_{stat} * \delta_v * sin(2\pi f_v) * t \ , \quad (8)$$

if f_v is substituted with a bending frequency of the footbridge, e.g. $f_{(1)}$.

3.2. The dynamic load in the horizontal lateral direction

Stoyanoff (2002) gave the formula for the load

$$F(t) = c_R * N * \alpha * w_P * cos\, \Omega t \ *, \quad (9)$$

where
- c_R (correlation coefficient ≈ 1)
- N number of pedestrians (20 ? 25 persons)
- $\propto$ dynamic coefficient (0,125)
- w_P weight of the pedestrian
- Ω dominant walking circular frequency (commonly f = 1 Hz)

According to Matsumoto (Footbridge, 2002) the force per unit length $f_P(x,t)$ can be expressed as

$$f_P(x,t) = \frac{\sqrt{N}*\alpha*w_p}{L} * cos\, \Omega t \ , \quad (10)$$

where
- $\propto$ = 0.04 (the footbridge without motion)
- L = the footbridge length
- Ω dominant walking circular frequency

4. Conclusions

The important results of measurements done in the ITAM laboratory and on the footbridges of various supportive systems follow:
- Mutual relations among the stride frequency, step frequency, step length, dynamic coefficient and the striding velocity depend on individual body characteristics of a pedestrian.
- The dynamic coefficient for a given pedestrian can be larger than for a group of pedestrians, if they do not move in a synchronous way.
- The obtained dynamic coefficients are of use for computations of load exerted by a single pedestrian, a group of pedestrians, a connected stream of pedestrians, and vandals, and for the computation of responses of footbridges with different supportive systems.
- Lateral horizontal forces of a pedestrian.

Acknowledgements

The support of the Grant Agency of the Czech Republic - grant No. 15-01035S and RVO 6837829 research plan are gratefully acknowledged.

REFERENCES

AASHTO (1997). Guide Specifications for Design of Pedestrien Bridges, American Association of State Highway and Transportation Officials.

Bachmann H, Ammann W (1987). Vibration in Structures Induced by Man and Machines; IABSE.

Barker C (2002). Some observations on the nature of the mechanism that drives the self-excited lateral response of footbridges, *International Conference, Footbridge 2002*, IABSE, Paris.CEB (1993). CEB-FIP Model Code 90. CEB Bulletin D'information, Comite Euro-International du beton, No. 213/214.

Footbridge (2002). International Conference, Paris, 2002.

Harper FC (1962). The mechanics of walking. *Research App. in Industry*, 15(1).

Koloušek V et al. (1967). Dynamics of Civil Engineering Structures (in Slovak), SVTL, Bratislava.

Pirner M, Urushadze S (2007). Pedestrian dynamics – footbridge loads, *Acta Technica CSAV*, 52, 269-283.

Stoyanoff S (2002). Human-induced vibrations on footbridges. *International Conference, Footbridge 2002*, IABSE, Paris.

Sviss Norm SIA 160 (1989). Effects of Loads on Structures.

Challenge Journal of Structural Mechanics

The boundary integral equation based method for damages detection in multilayered elastic structures

Arcady N. Soloviev [a,b], Alexander O. Vatulyan [a], Sergey N. Shevtsov [a,c,*], Alexander S. Spogakin [b]

[a] *Southern Federal University, Milchakov str., 8A, 344090 Rostov-on-Don, Russia*
[b] *Don State Technical University, Gagarin sq., 1, 344000 Rostov-on-Don, Russia*
[c] *South Center of Russian Academy, Tchekhov str., 41, SSC RAS, 344006 Rostov-on-Don, Russia*

ABSTRACT

For two kinds of defects – delamination and transversal failure in the multilayer composite the damages detection method is proposed. The inverse geometrical problems of crack's parameters reconstruction were formulated as a sequence of boundary integral equations (BIE). These boundary integral equations were derived on the basis of the principle of works mutuality applied to the problem of the composite specimen stationary oscillations. To solve the integral equations the finite element method, the boundary element method, and the Tikhonov regularization method were used. As complementary information for inverse problems solving the displacement field measured on a mechanical stress free area of the specimen's surface was served. The numerical examples of the interfacial cracks and transversal failure of the internal layers in the multilayered composite were considered in the framework of two-dimensional elasticity.

ARTICLE INFO

Article history:
Received 17 February 2016
Accepted 9 March 2016

Keywords:
Multilayered elastic structures
Damage identification
Delamination
Transversal fracture
Frequency scanning
Boundary integral equation

1. Introduction

The model of linear elastic body with cut and negligible interaction between cut's coasts can be successfully used for describing the solid bodies with cracks. Then boundary conditions for stress on the both flaw sides must be set as zero stress condition. In the framework of such linear model a problem of body stationary oscillations can be formulated. Solution of this problem makes possible use of a measured vibration displacement field on the free surface of body for damage parameters identification. The most natural statement of these problems is implemented for the cases when the section, which contains a defect is known; in a common case this section may be non planar. For plane cross-section the problem of defect parameters identification was considered in (Bannour et all., 1997). The problem of plane flaws identification at the harmonic excitation of elastic body was resolved by authors early (Vatulyan and Soloviev, 2003). Analytical methods developed in the mentioned works, require of measuring both stress and displacements on the whole body surface. An identification of interfacial flaws on the internal boundaries of compound elastic body refers to the same kind. Some methods of such inverse problems resolve have been developed. So, in (Vatulyan, 2003; Vatulyan et al., 2000) the method of non-classical BIE was proposed. W. Weikl with coauthors (Weikl et al., 2001) were used the iterative algorithm based on the approach proposed in (Kozlov et al., 1991). Applying to the problem of planar cracks reconstruction a semi-explicit algorithm for Laplase equation has been developed by T. Bannour with coauthors (Bannour et al., 1997).

In order to use of these methods in practical applications it is necessary to provide the measuring of displacement fields not on the whole boundary, but on its free part only. On the base of such a statement we propose three BIE-based approaches to the problem of defects identification. First approach uses statement of BIE relative to displacement jumps on the cracks, and second one use stress jump on internal boundaries containing

* *Corresponding author*. Tel.: +7-903-4013385 ; E-mail address: sergnshevtsov@gmail.com (S. N. Shevtsov)
ISSN: 2149-8024 / DOI: http://dx.doi.org/10.20528/cjsmec.2016.03.007

interlayer delaminations and transversal fractures. Defects reconstruction is conducted step-by-step, sequentially from the first external layer to the next one moving into the body's depth from the boundary on which the measurements are made. Next we derive the BIE system by application of mutuality theorems for bodies with defects and without it, which reconstruction is implemented on the previous steps. All constructed equations are the 1st kind Fredholm integral equations with smooth kernel, and therefore their resolving requires the regularization techniques. Here we use a combination of a Finite Element Method (FEM), Boundary Element Method (BEM), the known Tikhonov's regularization techniques (Tikhonov and Arsenin, 1979), and also approaches that has been proposed in (Vatulyan and Soloviev, 2004).

2. Inverse Problem Statement

In the Cartesian coordinate system $Ox_1x_2x_3(\underline{x} = (x_1, x_2, x_3))$ consider a laminated body located in the area $= \cup_{k=1}^{K} * V_k$. This body is bounded by a surface S and divided by interfacial surfaces S_{int} into k subdomains V_k . Onto surface S a partition $S = S_U \cup S_t \cup S_{fr}$ is defined, and $S_U \cap S_t = S_U \cap S_{fr} = S_t \cap S_{fr} = \theta$ (i.e. all subsets not disjointed). An acting stress vector p is defined on the surface S_t, and surface S_{fr} is free from the external stress. On the surface S_0 a subset $S_0 \subset S_{fr}$ is available for measurement of displacement vector . Let considered body, which contains several separated cracks $\Gamma = \cup_{q=1}^{M} \Gamma_q$, $\left(\Gamma_q = \Gamma_q^{(+)} \cup \Gamma_q^{(-)}\right)$ that are located between the nearest layers S_{int} - delaminations case (see. Fig.1).

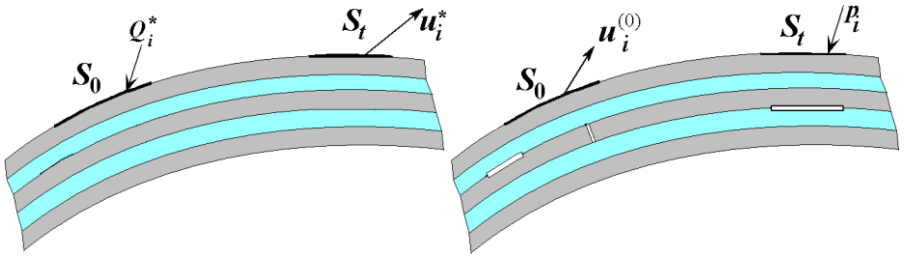

Fig. 1. Defects free (left) and defected (right) bodies.

At the stationary harmonic oscillations the boundary value problem for determination of stress-strain state and geometry of the cracks is formulated using the equations of linear elasticity (Nowacki, 1970).

$$\sigma_{ij,j}^{(k)} = -\rho\omega^2 u_i^{(k)} , k = 1,2, \dots, K \quad \underline{x} \epsilon V_k , \tag{1}$$

$$\sigma_{ij}^{(k)} = c_{ijml}^{(k)} u_{m,l}^{(k)} , \tag{2}$$

the boundary conditions for the forward problem

$$u_i^{(k)}|S_u = 0, t_i^{(k)}|S_t = \sigma_{ij}^{(k)} n_j|S_t = p_i, t_i^{(k)}|S_{fr} = 0 , \tag{3}$$

the definition of continuity constraints on

$$u_i^{(k)}|S_{int} \setminus \Gamma = u_i^{(k+1)}|S_{int} \setminus \Gamma, \quad t_i^{(k)}|S_{int} \setminus \Gamma = t_i^{(k+1)}|S_{int} \setminus \Gamma , \tag{4}$$

conditions on the cracks sides

$$t_i^{(k)}|\Gamma_q^{\pm} = 0, \ q = 1,2, \dots, M , \tag{5}$$

and supplementary conditions, corresponded to measuring of displacement vector on S_0

$$u_i^{(k)}|S_0 = u_i^0 . \tag{6}$$

In the expressions (1) - (6) $\sigma_{ij}^{(k)} = c_{ijml}^{(k)}$, are the stress and elastic constant tensors components respectively, $u_i^{(k)}$ are displacement vector components, $\rho^{(k)}$ is material density, ω is an angular frequency, n_j are components of unit normal vector to the corresponding surfaces, and $t_i^{(k)}$ are i-th components of stress vector applied to the surface.

Remark 1. In experimental applications the displacement vector distribution is defined most often not everywhere onto S_0, but on some discrete set of points. These points corresponds to the locations of the sensors, so, Eq. (5) must be replaced by

$$u_i^{(k)}(\underline{x}_m) = u_{im}^0, x_m \in S_0, \ m = 1,2, \dots, M . \tag{7}$$

3. The Auxiliary Problems

3.1. *Problem I*

Let us consider the problem I for defects free body V^0. Then boundary conditions on the inner surface S_{int} correspond to the continuity of displacements and stress vectors. The problem statement consists of differential Eq. (1), (2) for $u_i^{(k)*}$, $\underline{x} \in V_k$, the boundary conditions

$$u_i^{(k)*}|S_u = 0, \ t_i^{(k)*}|S_t = \sigma_{ij}^{(k)*} n_j|S_t = 0 , \tag{8}$$

$$t_i^{(k)*}|S_0 = \sigma_{ij}^{(k)*} n_j|S_0 = Q_i^*\left(\underline{x}, \underline{\xi}\right), \quad \underline{x}, \underline{\xi} \in S_0 , \tag{9}$$

and continuity constraints on S_{int}

$$u_i^{(k)}|S_{int} = u_i^{(k+1)*}|S_{int}, \ t_i^{(k)*}|S_{int} = t_i^{(k+1)*}|S_{int} . \tag{10}$$

3.2. *Problem II*

Next consider the boundary value problem II for body $V^2 = \bigcup_{k=1}^{K_1} * V_k$ at $K_1 < K$ the same load acting on S_0; and surface $S_{int}^{K_1}$ of last layer is stress free. At first we study this problem assuming the defects free body V^2.

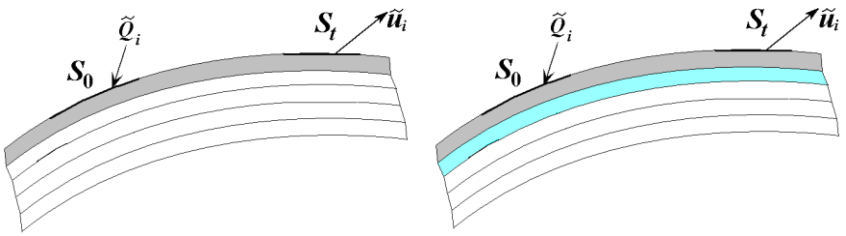

Fig. 2. The sequence of auxiliary problems for $K_1 = 1$ (left), and for $K_1 = 2$ (right).

The problem statement consists of differential Eq. (1), (2) for $\tilde{u}_i$, , $\underline{x} \in V^2$ the boundary conditions

$$\tilde{u}_i|S_u = 0,\ \tilde{t}_i|S_t = \tilde{\sigma}_{ij} n_j|S_t = 0\ , \tag{11}$$

$$\tilde{t}_i|S_u = 0,\ t_i|S_t = \tilde{\sigma}_{ij} n_j \Big|S_0 = \tilde{Q}_i\left(\underline{x}, \underline{\xi}\right),\ \ \underline{x}, \underline{\xi} \in S_0\ , \tag{12}$$

and $S_{int}^{K_1}$ condition when is stress free

$$t_i|S_{int}^{K_1} = 0\ . \tag{13}$$

3.3. *Problem III*

This boundary value problem is considered for a body $V^3 = \bigcup_{k=1}^{K_1-1} V_k \cup \hat{V}_{K_1}$, $K_1 < K$ which undergoes the same loads on the surface S_0. The surface $S_{int}^{K_1}$ (see Fig. 3, right) is wholly belongs to the K_1-th layer. Three types of conditions can be set on this surface: 1*st* – fixed surface, 2*nd* – sliding contact (restricted normal displacements and zero tangential stress), and 3*rd* – restricted tangential displacements and zero normal stress. At first we study this problem assuming the free defects body V^3.

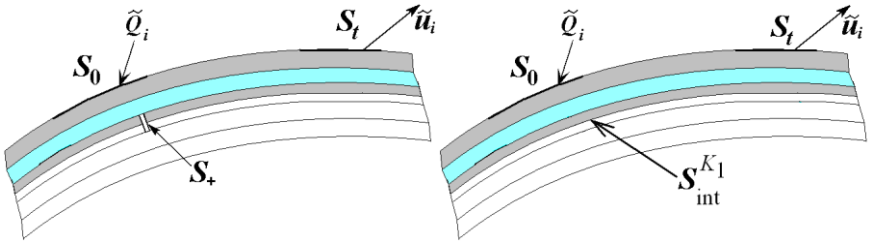

Fig. 3. The 3*rd* auxiliary problem (right K_1=3).

The problem statement consists of differential equations (1), (2) for $\hat{u}_i$, $\underline{x} \in V^3$, the boundary conditions

$$\hat{u}_i|S_u = 0,\ \hat{t}_i|S_t = \hat{\sigma}_{ij} n_j|S_t = 0\ , \tag{14}$$

$$\hat{t}_i|S_0 = \hat{\sigma}_{ij} n_j|S_0 = \hat{Q}_i\left(\underline{x}, \underline{\xi}\right),\ \ \underline{x}, \underline{\xi} \in S_0\ , \tag{15}$$

and also one from three boundary conditions types $S_{int}^{K_1}$, e.g. for 1*st* type of boundary conditions

$$\hat{u}_i|S_{int}^{K_1} = 0\,. \tag{16}$$

Remark 2. Here we assume that ξ dependence of functions $Q_i^*\left(\underline{x}, \underline{\xi}\right)$, $\tilde{Q}_i\left(\underline{x}, \underline{\xi}\right)$ can be considered as one parameter set

$$Q_i^*\left(\underline{x}, \underline{\xi}\right) = P_i^* \delta\left(\underline{x} - \underline{\xi}\right) \quad \tilde{Q}_i\left(\underline{x}, \underline{\xi}\right) = \tilde{P}_i\left(\underline{x} - \underline{\xi}\right). \tag{17}$$

Remark 3. The technique of BIE design with the aid of the problem II or problem III does not changed if the bodies V^2 and V^3 contain known imperfections (possibly identified on the previous step).

4. Derivation of BIE on the Basis of Auxiliary Problems Solution

4.1. Derivation of BIE on the basis of problem I solution

Let's consider the multilayered material with the presence of some delaminations and absence of any transversal failures. Assuming that the problem I is resolved denote

$u^{(k)*}|S_t = \phi^*\left(\underline{x},\underline{\xi}\right),\ \underline{x}\in S_t,\ \ \underline{\xi}\in S_0$.

Regarding an operator

$$G\left(\underline{u}^0,\underline{p},\underline{\phi^*},\underline{Q^*}\right) = \int_{S_0} u_i^0(\underline{x})Q_i^*\left(\underline{x},\underline{\xi}\right)dS_x - \int_{S_t}\phi_i^*\left(\underline{x},\underline{\xi}\right)p_i(\underline{x})dS_x = G_1\left(\underline{\xi}\right), \quad (18)$$

we apply the theorem of works mutuality (Nowacki, 1970) to the bodies V and V^1. Taking into account the continuity conditions (4) on $S_{int}\backslash\Gamma$ and (10) on the S_{int}, such equation can be obtained

$$\int_\Gamma t_i^{(k)*}\left(\underline{x},\underline{\xi}\right)X_i(\underline{x})dS_x = G_1\left(\underline{\xi}\right), \quad (19)$$

where $X_i(\underline{x})$ - the jumps of displacement vector on the cracks. It is important to mark that on $S_{int}\backslash\Gamma$ these jumps have zero value. Entering a designation

$$X_i(\underline{x}) = \begin{cases} X_i & at\ \ \underline{x}\in\Gamma \\ 0 & at\ \ \underline{x}\in S\backslash\Gamma \end{cases},$$

into relationship (19) transform it to the system of integral equations for functions $X_i(\underline{x})$, which are defined on $\underline{x}\in S_{int}$.

$$\int_{S_{int}} t_i^{(k)*}\left(\underline{x},\underline{\xi}\right)X_i\left(\underline{x}\right)dS_x = G_1\left(\underline{\xi}\right), \xi\in S_0, \quad (20)$$

where integration spread over the known surface . It is clear that last equation can be used for the cracks shape reconstruction at variation of excitation frequency and load distribution.

4.2. Derivation of BIE on the basis of problem II solution end examine the integral operator

As well as in the previous section we consider the multilayered material with the presence of some delaminations and absence of any transversal failures. Let auxiliary problem II is resolved. Then denote

$$\tilde{u}^{(k)}|S_t = \tilde{\phi}\left(\underline{x},\underline{\xi}\right), \underline{x}\in S_t,\ \ \underline{\xi}\in S_0,$$

and examine the integral operator

$$F\left(\underline{u}^0,\underline{p},\underline{\phi^*},\underline{Q^*}\right) = \int_{S_0} u_i^0(\underline{x})Q_i^*\left(\underline{x},\underline{\xi}\right)dS_x - \int_{S_t}\phi_i^*\left(\underline{x},\underline{\xi}\right)p_i(\underline{x})dS_x = F_1\left(\underline{\xi}\right). \quad (21)$$

Applying the theorem of works mutuality (Nowacki, 1970) to the body, which occupy the subdomain V^2 we can obtain

$$\int_{S_{int}^{K_1}\backslash\Gamma}\left(\underline{x},\underline{\xi}\right)t_i^{(K_1)}\left(\underline{x}\right)dS_x = F_1\left(\underline{\xi}\right). \quad (22)$$

Taking into account that multipliers under integral (22) are defined everywhere on $S_{int}^{K_1}$, and because of (5)

$$t_i^{(K_1)}|\Gamma = 0\ , \quad (23)$$

the relationship (22) can be treated as BIE system on the known boundary S

$$\int_{S_{int}^{K_1}}\left(\underline{x},\underline{\xi}\right)t_i^{(K_1)}\left(\underline{x}\right)dS_x = F_1\left(\underline{\xi}\right);\ \ \xi\in S_0\ , \quad (24)$$

It is necessary to mark herein an important difference between the system (20) and (24). Identification based on the Eq. (20) use that searched variables are not zero inside the cracks area. Unlike the previous case the crack reconstruction using Eq. (24) assume zero value of stress vector components on the crack's coasts, and also their singular behavior at come to the crack coast out of intact area. This singularity appears numerically as a rapid growth of these components.

4.3. Derivation of BIE on the basis of problem III solution

Now consider the multilayered material with the presence of some transversal fracture and absence of any delaminations. Let auxiliary problem III is resolved. Then denote

$$F\left(\underline{u}^0,\underline{p},\underline{\phi^*},\underline{Q^*}\right)\hat{u}^{(k)}|S_t = \hat{\phi}\left(\underline{x},\underline{\xi}\right),\ \underline{x}\in S_t,\ \underline{\xi}\in S_0$$

Considering operator

$$T\left(\underline{u}^0,\underline{p},\underline{\phi^*},\underline{Q^*}\right) = \int_{S_0} u_i^0(\underline{x})Q_i^*\left(\underline{x},\underline{\xi}\right)dS_x - \int_{S_t}\phi_i^*\left(\underline{x},\underline{\xi}\right)p_i(\underline{x})dS_x = T_1\left(\underline{\xi}\right), \quad (25)$$

and applying the mutuality theorem [9] to the body, which locates in a subdomain V^3, we shall obtain

$$\int_{S_{int}^{K_1}}\hat{t}_i^{(k)}\left(\underline{x},\underline{\xi}\right)u_i\left(\underline{x}\right)dS_x + \int_{S_+}^{\hat{t}_i^{(k)}}\left(\underline{x},\underline{\xi}\right)X_i\left(\underline{x}\right)dS_x = T_1\left(\underline{\xi}\right), \quad (26)$$

where $X_i(\underline{x})$ - jumps of displacement vectors on the transversal cracks (ply fracture). However, in practice, using of Eq. (26) is impossible because of unknown boundary S_+. Therefore we use a surface $S_{int}^{K_1}$, which is located in adjacency to the boundary separating the layers K_1-1 and K_1. As S_+ is a small quantity we can neglect second summand in Eq. (26) in the first time. Then Eq. (26) is substituted by

$$\int_{S_{int}^{K_1}}\hat{t}_i\left(\underline{x},\underline{\xi}\right)u_i^{(1)}\left(\underline{x}\right)dS_x = T_1\left(\underline{\xi}\right). \quad (27)$$

It is worth to notice that at presence of transversal fractures and at successfully selected oscillation frequency the functions $u_i^{(1)}$ are piecewise continuous, and the points of discontinuity coincide with surfaces intersection. So, it is possible to use of Eq. (26) at the second stage with variation of S_+ position relative to its initial position founded on the first stage.

5. Frequency Scanning and Cracks Identification

If a used experimental setup and tested structure do not restrict of the scanning frequency range, it is desirable to expand this range so that it includes as much as possible of structure's eigenfrequencies. Then functions in eq. (20) and (24) will be defined in the following frequency domain

$$\omega \in \Omega = \cup_{n=1}^{N} \Omega_n, \ \Omega_n = \left[\omega_n^{(b)}, \omega_n^{(e)}\right],$$

where intervals Ω_n can be chosen after the preliminary modal analysis of defects free structure. The selected frequency intervals should include those vibration modes, at which there is an intensive opening of cracks. Usually, it is the tensile-compression or shear deformations modes in a neighborhood of a surface S_{int}, while the flexural modes are less sensitive to existence of the crack-like imperfections.

Now the system (20) can be rewritten in the form

$$\int_{S_{int}} t_i^{(k)*}\left(\underline{x}, \underline{\xi}, \omega\right) X_i\left(\underline{x}, \omega\right) dS_x = G_1\left(\underline{\xi}, \omega\right), \ \xi \in S_0, \quad \omega \in \Omega. \tag{28}$$

As the carrier (crack's geometry) of functions $X_i(\underline{x}, \omega)$ does not depend on ω, the solution of the equation (28) in a frequency set Ω allows achieving a high accuracy of the cracks numerical reconstruction. Let's mark here that function $G_1(\xi, \omega)$ equal to zero everywhere in Ω if the body has no cracks. This circumstance gives a simple means of cracks detection even if the surface S_{int} is a priory unknown. For this purpose it is enough to choose any scheme of loading in a problem I, for instance, scheme (9) at $\underline{\xi} = \underline{\xi_k}$ and to construct a frequency response

$$G_2(\omega) = G_1\left(\underline{\xi_k}, \omega\right), \quad \omega \in \Omega.$$

At known precision of the displacement field u_i^0 (see Eq. 6) measurements, and known exactitude of integrals (15) calculation one can conclude a crack's occurrence by form of this frequency response.

At the frequency scanning the system (28) is replaced by the following system

$$\int_{S_i^{K_1}} \tilde{u}_i^{(k)}\left(\underline{x}, \underline{\xi}, \omega\right) t_i^{(K_1)}\left(\underline{x}, \omega\right) dS_x = F_1\left(\underline{\xi}, \omega\right), \ \xi \in S_0, \quad \omega \in \Omega, \tag{29}$$

where the principle of geometry Γ reconstruction does not depend on frequency ω, as well as for (28).

Remark 4. As the functions $\underline{Q^*}$, $\underline{\widetilde{Q}}$ are defined on a discrete set of measuring points x_m, the integrals in (18) and (21) can be calculated explicitly.

6. Numerical Examples of Cracks Parameters Reconstruction

6.1. Example 1

At first consider the problem of identification of two longitudinal cracks Γ_1 =KL and Γ_2 =MN located between two layers of semi-passive bimorph that has a rectangular shape AOBCED [A(0;-0.03), O(0;0), B(0;0.03), C(0,1;0.03), E(0.1;0), D(0.1;-0.03), K(0.03;0), L(0.05,0), M(0.065;0), N(0.08;0)]– all dimensions in meters. The upper layer OBCE is made of Cu, and lower layer AOED – made of piezoelectric ceramic PZT-4. The present resolving scheme leads to Eq. (21), which is resolved in the framework of plane strain. The forced oscillations at frequency $f = \left(\omega/(2\pi)\right) = 20$ kHz are excited by alternating voltage $V_0 = 1000$ V applied to electrodes located on the sides OE and AD. The boundary AB is fixed; the remaining exterior boundaries are stress free.

All numerical simulations were implemented using FEM package ACELAN (Belokon, 2000). The cracks were modeled by holes which transversal size is sufficiently short comparing to their length (~ 10-7). It was supposed that the crack walls do not interact. Near the crack tip a FEM mesh was essentially condensed. The side BC was accessible to measurements of the displacement vector, and on this side 39 interior equidistant nodes were selected, in which displacements were calculated. The excitation frequency was chosen from reasons of intensive crack opening, but it should differ from the natural frequencies of a boundary value problem II. These natural frequencies are shown in Table 1.

Table 1. The first eigenfrequencies of the studied semi-passive bimorph (kHz).

Eigenfrequency No	Free of defects	Boundary problem II
1	2.851	1.721
2	9.194	7.946
3	9.858	9.575
4	19.01	17.51
5	22.32	27.18
6	24.16	27.88

BIE (24) was resolved on the basis of the Boundary Element method. For discretization of Eq. (24), a piecewise constant and piecewise linear continuous approximation of unknown depending variables was used. However, our numerical experiments have shown that the first scheme is more preferable. The discrete analog of Eq. (24) was resolved by the Tikhonov regularization method (Tikhonov and Arsenin, 1979) and regularization parameter for n=40 was accepted 2·10-14 (n- number of points, in which displacements were "measured").

Some obtained results are present in Figs. 4 and 5. Fig. 4 demonstrates the stress amplitude distributions along

a sample with one crack KL. Two extremes of stress there correspond to coordinates of the crack's tips. The diagrams of a stress distribution in a specimen with two cracks are present on a Fig. 4, where for comparison the graphs created by the solution of the problem (24) and FEM solution results are displayed. The tips of both cracks also easily identified.

In the performed numerical experiment the influence of the number n "measured" points, which provide the input information, on the precision of crack reconstruction was also studied. Relative errors of the crack tips determination at different number of the "measured" points on a side BC at distance 0.25 mm between adjacent points are present in Table 2.

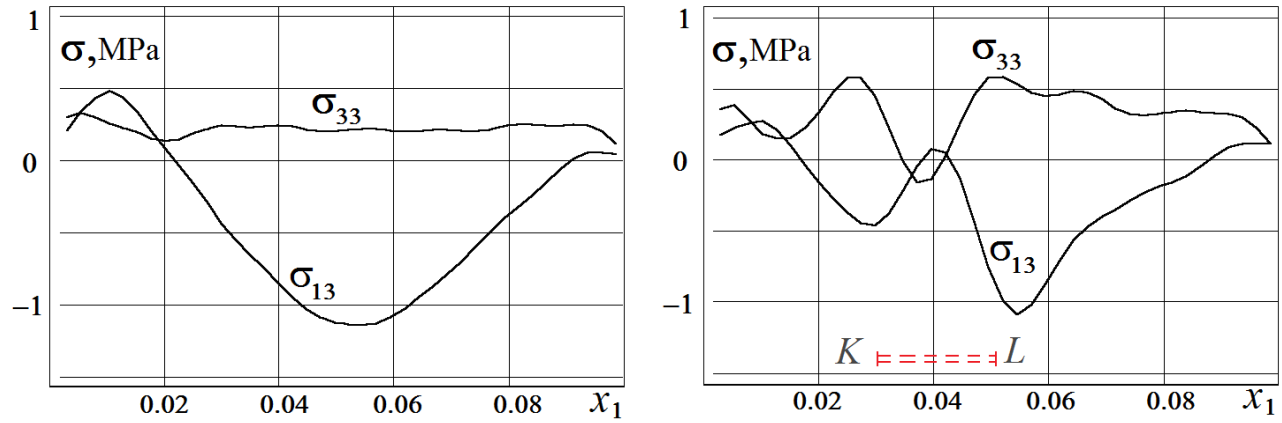

Fig. 4. The stress distributions in the intact specimen (left diagram) and in the specimen with interfacial crack KL (results of the inverse problem (24) solution).

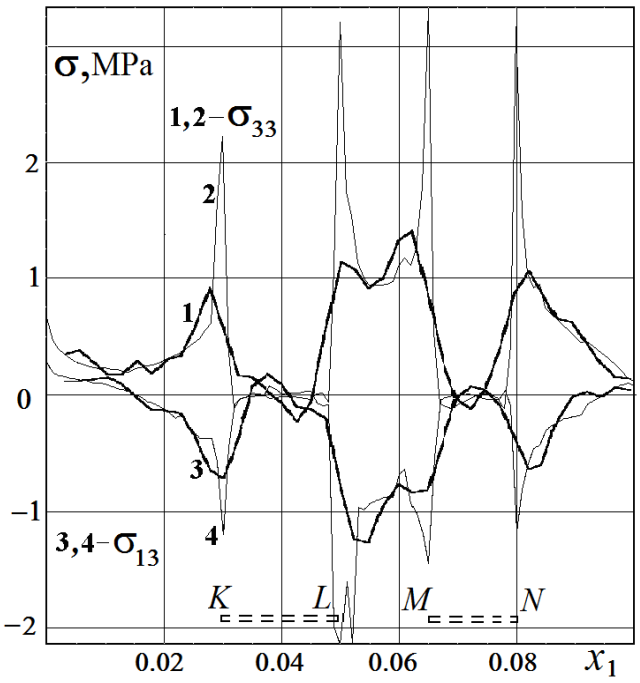

Fig. 5. The stress distributions in a specimen with two interfacial cracks KL and MN
(bold lines – FEM solution results; subtle line – BIE solution result).

Table 2. Relative tolerance of crack's tip coordinate identification (in percents).

Number of points n	x_K	x_L	x_M	x_N
10	5.0	6.4	3.8	5.5
20	4.2	3.6	2.0	3.3
30	4.2	2.5	1.9	3.1
40	4.2	2.5	1.9	3.1

6.2. Example 2

In this example the interface delamination in free bimorph (Fe, Cu) plate (0.3x0.04 м) is identified. From the Table 3, where the first three natural frequencies and vibration modes are shown, one can see that the frequency near the first flexural mode is not suitable for the efficient crack reconstruction. On the second eigenfrequency the principal role a horizontal displacement of crack's side is played, and on the third mode – crack opening along a vertical direction. For this crack identification the Eq. (20) was used. The discretization of the searched functions - discontinuities of the crack's coasts displacements by 10 piecewise constant elements was implemented. Fig. 6 demonstrates the found jumps of horizontal displacements (left graph) near the second eigenfrequency (16000 rad/s), and vertical displacement (right graph) near the third eigenfrequency.

Table 3. Eigenfrequencies and natural oscillation modes, which are used for the longitudinal crack (local delamination) identification in the bimorph plate.

Eigenfrequency, kHz		Natural oscillation mode shape
1.82	Vertical displacements	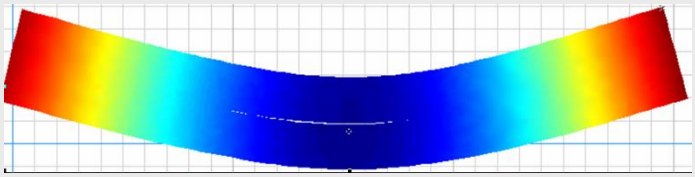
2.57	Horizontal displacement	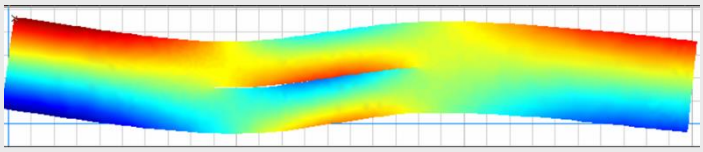
5.97	Vertical displacements	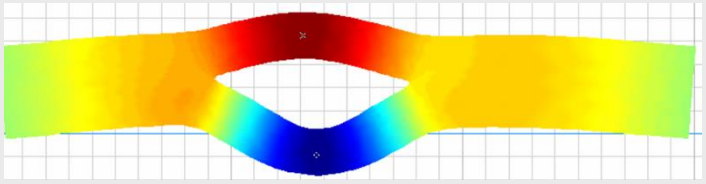

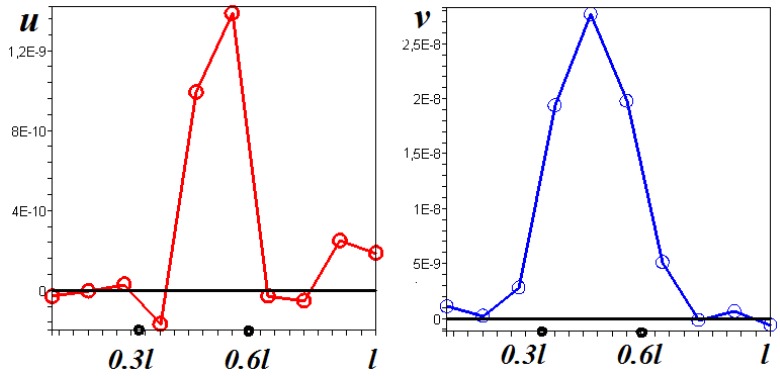

Fig. 6. The jumps of horizontal (left) and vertical (right) displacements on the crack's coasts (explanation in text).

6.3. Example 3

Next example illustrates an application of BIE derived in sub-section 4.3 for reconstruction of two separated transversal fractures in intermediate layer of three-ply laminate. Coordinates of fractures are x=0.02 and x=0.05 (see Table 4). Preliminary FEM analysis has shown that on the natural frequency 20.59 kHz, which provides the major amplitude of horizontal displacements, there an intensive opening of cracks is. Fig. 8 demonstrates the charts of horizontal displacement on a center line of interior layer at harmonic oscillation near to eigenfrequency. Observed displacements discontinuities on the charts are caused by the presence of two cracks. On both charts the continuous bold lines present the solution obtained using finite element method, whereas the light lines with small circles – solutions obtained by Boundary Element method implemented using GMRES algorithm (Rjasanow and Steinbach, 2007). The left plot in Fig. 7 demonstrates solution of the Eq. (27), and right plot - specified solution of the Eq. (26). BEM based solutions are implemented by using of piecewise continuous approximation, which is the most preferable for discontinuous solutions. One can see that location of both cracks is reconstructed with the satisfied precision.

Table 4. Eigenfrequencies and natural oscillation modes, which are used for two transversal crack identification in the in the three-layered plate.

Eigenfrequency, kHz	Natural oscillation mode shape
7.11 Horizontal displacement	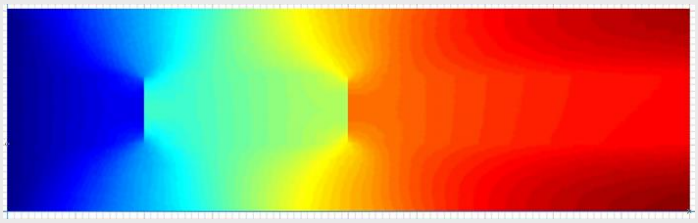
20.59	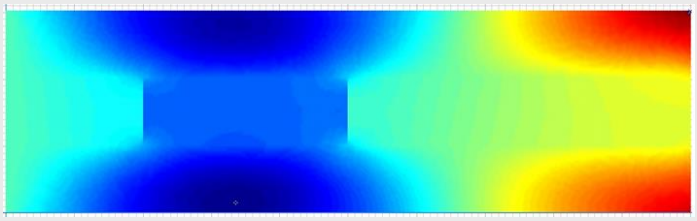

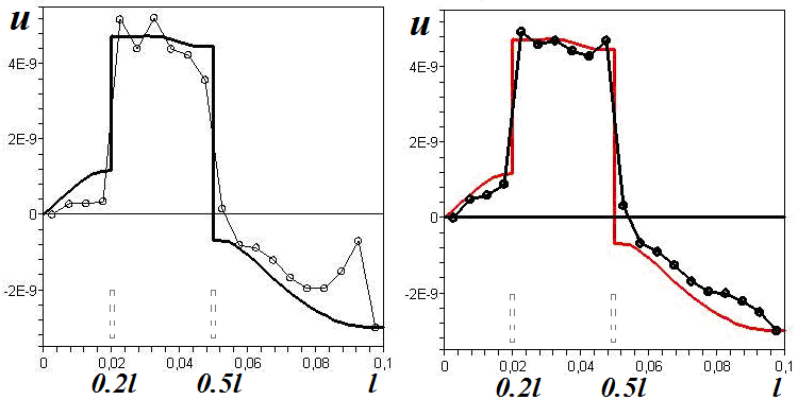

Fig. 7. The results of two transversal fracture reconstructions in the intermediate layer of three-ply laminate (explanation in text).

7. Conclusions

The boundary integral equation method is proposed and effectively used to solve the problem of longitudinal and transversal crack identification in multilayered elastic structures. These boundary integral equations were derived using the principle of works mutuality applied to the problem of stationary oscillations of the multilayered elastic structures. In order to excite these oscillations into a broad frequency range, which contains some eigenfrequencies of the studied structure, the local sources of harmonical excitation are provided. These sources can be disposed on some part of tested structure's surface. As input information for the defects identification problem the displacements, which are measured on the discrete set of points belonging to the stress free area of the tested specimen's surface is used.

- Precision of the crack's tips coordinates determination essentially depends on location of the displacement field measurements area. Therefore at the use of discrete set of points for measuring of displacement field (the positional probe) their location should be extended on the overall accessible area. The obtained overdetermined equations system can be resolved by application of some regularization scheme.
- If the choice of oscillation frequencies is not restricted by a measuring apparatus and by specificity of a tested structure, it is necessary to perform the preliminary numerical modal analysis with the purpose of operational frequencies selection. It is necessary to select those frequencies, which cause intensive motions of a material close to guessed imperfections. It is possible also to expand the resolving linear equation system by scanning in a broad frequencies band (frequency scanning).
- To increase the reliability of the identification results in the areas with high gradients of the solution, the iterative reconstruction scheme with sequentially finer finite element mesh is desirable.
- Use of the step by step reconstruction scheme allows identifying multiple imperfections located in the different layers of a multilayered composite material.

REFERENCES

Bannour T, Ben Abda A, Jaoua M (1997). A semi-explicit algorithm for the reconstruction of 3D planar cracks. *Inverse Problem*, 13, 899-917.

Belokon AV, Eremeev VA, Nasedkin AV, Soloviev AN (2000). The block schemes of a finite element method for dynamic problems of acousto-electro-elasticity. *Applied Mathematics & Mechanics*, 64(3), 381-393 (in Russian).

Kozlov VA, Mazya VG, Fomin, VG (1991). Iterative method for cauchi problem resolving for elliptic equations. *Computational Mathematics and Mathematical Physics*, 31, 45-52 (in Russian).

Nowacki W (1970). Teoria Sprezystosci. Panstwowe Wydawnictwo Naukowe, Warszawa (in Polish).

Rjasanow S, Steinbach O (2007). The Fast Solution of Boundary Integral Equations. Springer ed., 284.

Soloviev AN (2002). Identification of interfacial flaws. *Proceedings on the VIII International Scientific Conference "Modern Problems of Continuum Media Mechanics"*, Rostov-on-Don, 1, 163-169.

Tikhonov AN, Arsenin VY (1979). Methods for Non-Correct Problems Resolving. Science ed., Moscow (in Russian).

Vatulyan AO, Soloviev AN (2003). Determination of plane flaws orientation in elastic body. *Theoretical an Applied Mechanics*, (37), 141-145 (in Russian).

Vatulyan AO, Soloviev AN (2004). On the defects determination in composite elastic body. *Defectoscopy*, 5, 15-23 (in Russian).

Vatulyan AO, Vorovich II, Soloviev AN (2000). On the one kind of boundary problems in the dynamical elasticity. *Applied Mathematics and Mechanics*, 64(3), 373-380 (in Russian).

Weikl W, Andra H, Schnack E (2001). An alternating iterative algorithm for the reconstruction of internal cracks in a three-dimensional solid body. *Inverse Problem*, 17, 1957-1975.

Challenge Journal of Structural Mechanics

Seismic response of a ten story concrete building subjected to different earthquakes

Amaia Martinez *, Carlos E. Ventura

Department of Civil Engineering, University of British Columbia, Vancouver V6T 1Z4, Canada

ABSTRACT

The purpose of this paper is to compare the response of a ten story concrete building in San Jose, California, under three different earthquakes. The strong-motion records of the instrumented building obtained during the 1984 Morgan Hill earthquake were used to calibrate a finite element model. Soil-structure interaction was included in the model by adding some translational springs to the foundation. The same model was subjected to 1986 Mount Lewis and 1989 Loma Prieta earthquakes. While for the first case a good match between the recorded data and analytical results was obtained, for the second one the match was not as good as expected. A modal identification analysis of the building was conducted for the three ground motions using both just output operational modal analysis (OMA) and input-output experimental modal analysis (EMA). It was demonstrated that for Loma Prieta, which presents higher amplitude shaking than the other two ground motions, the fundamental period for the transversal mode of the structure was higher than that obtained using the other two earthquakes. Consequently, the springs of the finite element model needed to be updated for Loma Prieta in order to capture the more flexible response of the building. After this adjustment, there was a good match between the recorded motions and analytical results. This study proves that the effects of soil-structure interaction becomes very important when a building is subjected to high levels of shaking. In some cases, a single model of a building with concrete shear walls may not be suitable to predict properly the behavior of the building under different ground motions.

ARTICLE INFO

Article history:
Received 12 January 2016
Accepted 11 March 2016

Keywords:
Operational modal analysis
Finite element analysis
Validation
Ambient vibration

1. Introduction

The recorded response data from instrumented buildings can be especially helpful for a better understanding of the true behavior of the structures. The ground motion data obtained by sensors located in several different points of a building is used for the calibration and validation of its finite element model.

The dynamic response of a permanently instrumented ten-story commercial concrete shear wall building located in San Jose, California is studied. The building was instrumented in the 70's by the California Division of Mines and Geology – Strong Motion Instrumentation Program (CSMIP) in order to obtain strong motion and building response data. The instruments installed in several locations of the building recorded valuable data during April 24th 1984 Morgan Hill, March 31st 1986 Mount Lewis and 17th October 1989 Loma Prieta earthquakes. The recorded motions have been used to calibrate and update a computer finite element model of the structure.

This study comprises the following parts: investigation of the building's structural system, modal identification using the strong motion data collected at the building, calibration and updating of a computer model of the building, and comparison of the response of the building model subjected to the three different ground motions. This paper summarizes the important results obtained from a previous study by Martinez et al (2015) and focus on the additional results.

* *Corresponding author*. Tel.: +1-778-558-6179 ; E-mail address: amaiamar2@gmail.com (A. Martinez)
ISSN: 2149-8024 / DOI: http://dx.doi.org/10.20528/cjsmec.2016.03.008

2. Description of the Building and Instrumentation

2.1. Description of the building

The 10-story Great Western Saving building was built in 1964 and is located in San Jose, California. Its dimensions are 82 ft by 190 ft for its rectangular base (equal for every floor) and 102 ft for the elevation. Story heights are typically 12 ft, except from the ground floor and underground floor, which are 16 ft and 17 ft high respectively. The building is settled on a 90'x194'x5' reinforced concrete spread footing. The geology of the site is mainly alluvium, but parameters of the soil profile were not available for this study.

The lateral force resisting systems of the structure consists of moment frames in the longitudinal direction (NS-direction) and two concrete shear walls in the transversal direction (EW-direction). The building includes two elevator cores in the middle of the base plan, stairs joined to the shear-walls in both sides and two interior openings. An exterior view of the building is presented in Fig. 1.

Fig. 1. Ten story instrumented great western saving building in San Jose, California (adapted from CESMD).

2.2. Instrumentation of the building

The structure has 13 permanent force-balanced accelerometers which record accelerations at different locations of the building in different directions (vertical, longitudinal (SN) and transversal (EW)). Table 1 and Fig. 2 show the location of each sensor and the direction of the recorded data.

2.3. Recorded motions

The recorded motions for all the sensors during Morgan Hill, Mount Lewis and Loma Prieta earthquakes were obtained from CESMD (Center for Engineering Strong-Motion Data). Free field data in the vicinity of the building for the same ground motions was not available. Consequently, the mean of the channels of the basement for each direction is calculated and used as input ground motion for all the analysis performed in this study.

Acceleration time histories and the 5%damping acceleration spectra comparison of the three ground motions considered for this study are shown in Fig. 3 and 4 respectively. Mount Lewis presents the lowest peak accelerations (34 cm/sec^2) among the earthquakes, followed by Morgan Hill (59 cm/sec^2) and finally by Loma Prieta (97 cm/sec^2). Moreover, the acceleration spectra confirms that Loma Prieta produced significantly stronger ground shaking than the other two earthquakes, resulting in higher demands in the building. In addition, Loma Prieta has longer duration.

3. Modal Identification of the Structure

Modal identification of the structure was performed in Martinez et al. (2015) using ARTeMIS® computer program. Operational modal analysis (OMA) was conducted with the recorded ground motion data in different locations of the building as outputs. In addition, for this study input-output experimental modal analysis (EMA) for the three earthquakes is investigated and compared to the results obtained from the OMA.

This EMA uses as inputs (I) the recorded motions at the base and as outputs (O) the recorded motions at the fifth floor and at the roof. The measurements are converted from time domain to frequency domain using Fast Fourier transform algorithm and the transfer function (TF) is calculated as output divided by the input.

Transfer functions of the 5th floor and the roof for longitudinal and transversal direction are obtained for each of the seismic events. The obtained input-output EMA results for each of the events are compared in frequency domain to the spectral density results obtained from OMA. Fig. 5, 6 and 7 show in red and pink the TF-s obtained for the roof and 5th floor in transverse direction, and in dark and light blue in the longitudinal direction. These EMA results are plotted together with the OMA results, in which the identified natural frequencies are highlight as a black line.

The frequencies at which the first peaks occur in both longitudinal and transversal directions using EMA show good agreement with the natural frequencies obtained from ARTeMIS. The maximum deviation between the two different modal identification approaches is shown to happen during Mount Lewis event for the transversal direction with a 6% of error. It is also proved that the peaks of the TF-s at the two different levels of the building (5th floor and roof) for each direction occur at the same frequencies but with a higher amplitudes for the upper level.

For all of the earthquakes the first natural frequency representing the longitudinal direction of the building is

around 1 Hz. However, the second natural frequency, which represents the first transversal mode, for Loma Prieta earthquake is lower than for Morgan Hill and Mount Lewis. The results of the comparison of both modal analysis approaches confirm that the dynamic characteristics of the building change depending on the ground motion. For Loma Prieta, the highest intensity earthquake, the structure behaves more flexible in the transversal direction.

	TIME DOMAIN		FREQUENCY DOMAIN	
INPUT	I (t)	→	I (w)	TF (w) = O(w) / I (w)
OUTPUT	O (t)	→	O (w)	

Table 1. Sensor number, location in the building and recorded direction of each accelerometer.

SENSOR NUMBER	LOCATION		MEASURED DIRECTION
	FLOOR	POSITION	
1	Basement	South West	Vertical
2	Basement	South East	Vertical
3	Roof	South Center	Transversal (EW)
4	Roof	North Center	Transversal (EW)
5	Roof	South Center	Longitudinal (SN)
6	5th Floor	South Center	Transversal (EW)
7	5th Floor	In the middle	Transversal (EW)
8	5th Floor	North Center	Transversal (EW)
9	5th Floor	South Center	Longitudinal (SN)
10	2nd Floor	South Center	Longitudinal (SN)
11	Basement	South Center	Transversal (EW)
12	Basement	North Center	Longitudinal (SN)
13	Basement	South Center	Longitudinal (SN)

4. Finite Element Modeling, Validation and Updating

4.1. Finite element model description

The design drawings of the building were used to develop a finite element model of the building using ETABS 2013 software. A linear elastic model of the structure supported by a flexible base was created. The base was designed as spreading concrete slab footing over a series of springs of finite stiffness. The foundation springs were modeled using the soil and foundation information available as specified in Gazetas (1983). The model includes structural, as well as, non-structural elements. Gravity frames, lateral load resisting frames, shear walls, interior core walls, openings and stairs were modeled too. For the reinforced concrete elements 80% of the modulus of elasticity, un-cracked moment of inertia and linear stress-strain reinforcement relationship was used. All the beam-column connection were designed as moment connections. A three dimensional view of the ETABS model is shown in Fig. 8.

4.2. Calibration of the model

A first manual calibration was performed using one of the low level of shaking earthquake (Morgan Hill).Structural properties and masses were modified manually until a “best match” between experimental and analytical results was obtained. The obtained first natural frequencies of the calibrated finite element in each direction were similar to the ones obtained through OMA and input-output EMA. In addition, recorded and analytical acceleration time histories and velocities and relative

displacements (obtained by integration of accelerations) in all the channels during Morgan Hill event were compared. The calibration of the model was considered acceptable once a good correlation coefficient between the experimental and analytical results was obtained. However, a more accurate calibration could be performed using automatic modal updating tools.

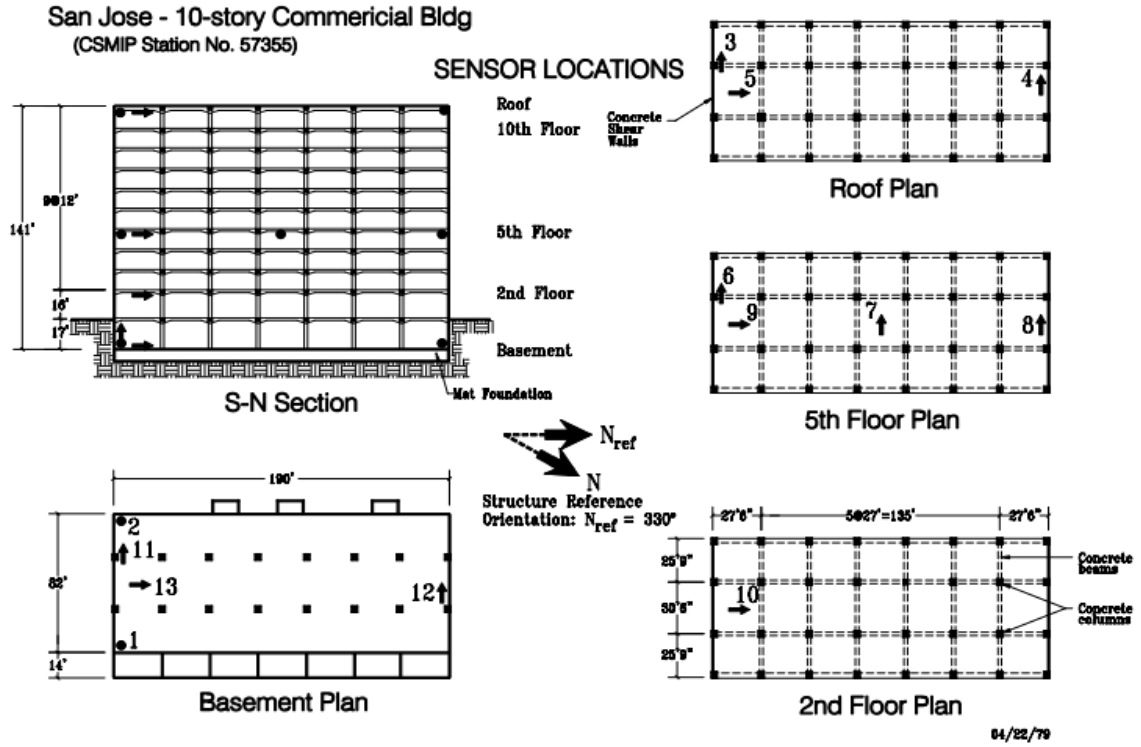

Fig. 2. Schematic map of instrumentation of the building (adapted from CESMD).

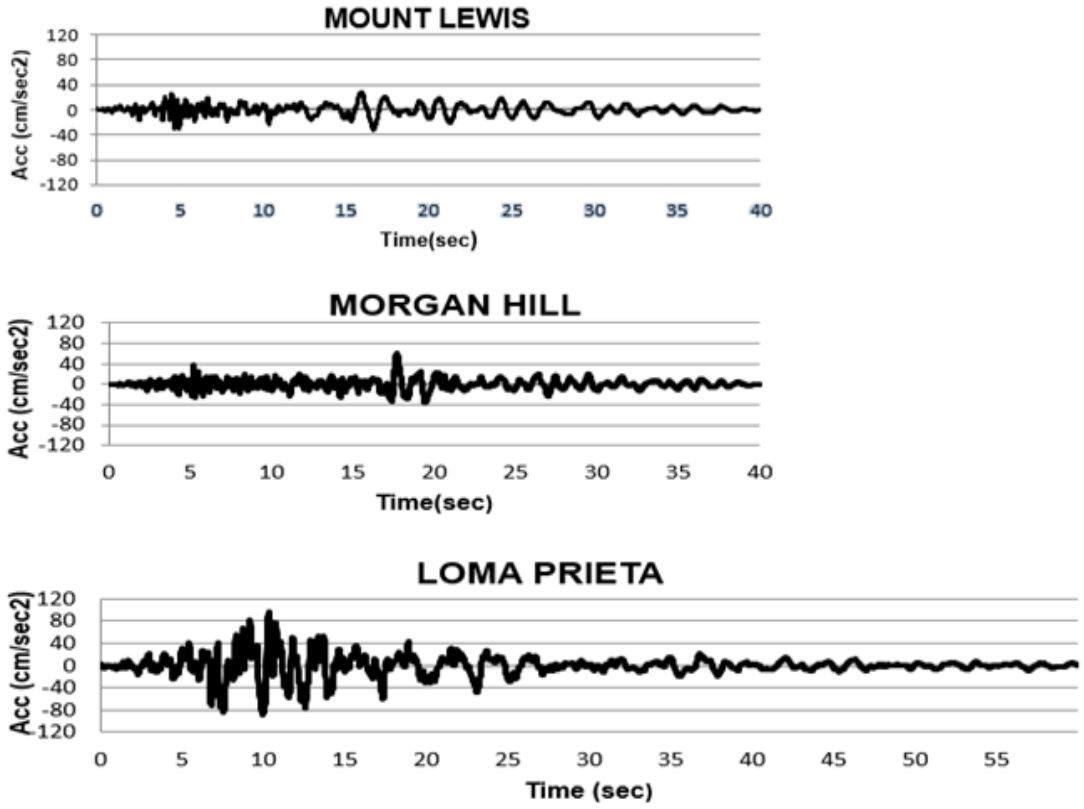

Fig. 3. Recorded acceleration time histories for Mount Lewis, Morgan Hill and Loma Prieta at the basement for EW direction.

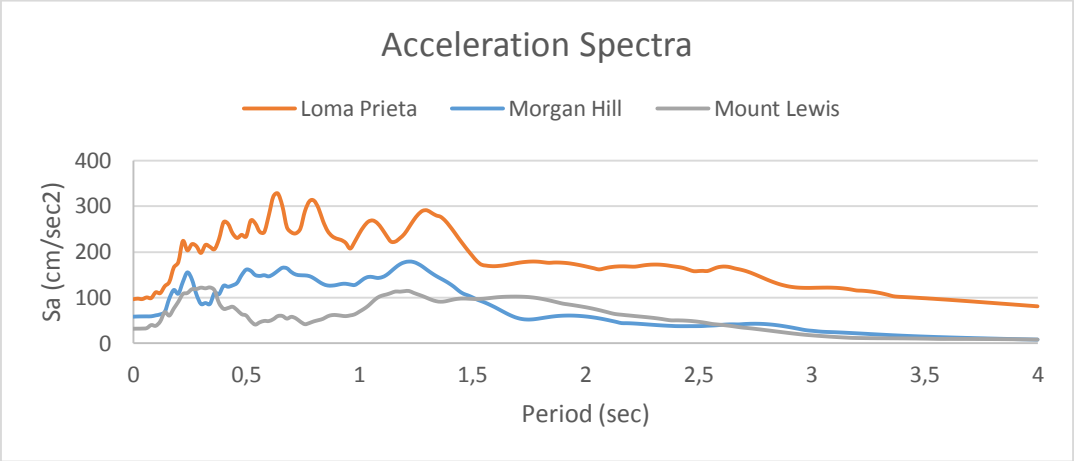

Fig. 4. - Comparison of acceleration spectra for Mount Lewis, Morgan Hill and Loma Prieta.

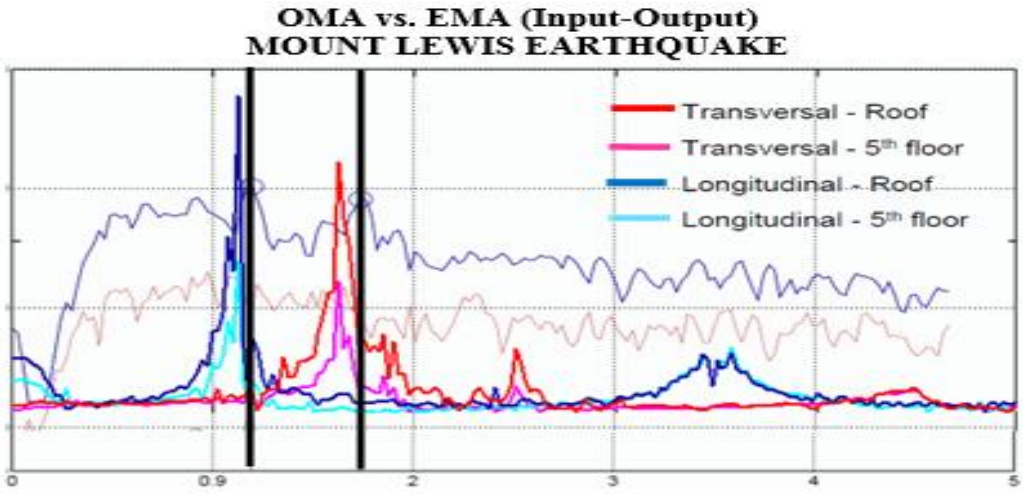

Fig. 5. OMA and input-output EMA results comparison in frequency domain for Mount Lewis.

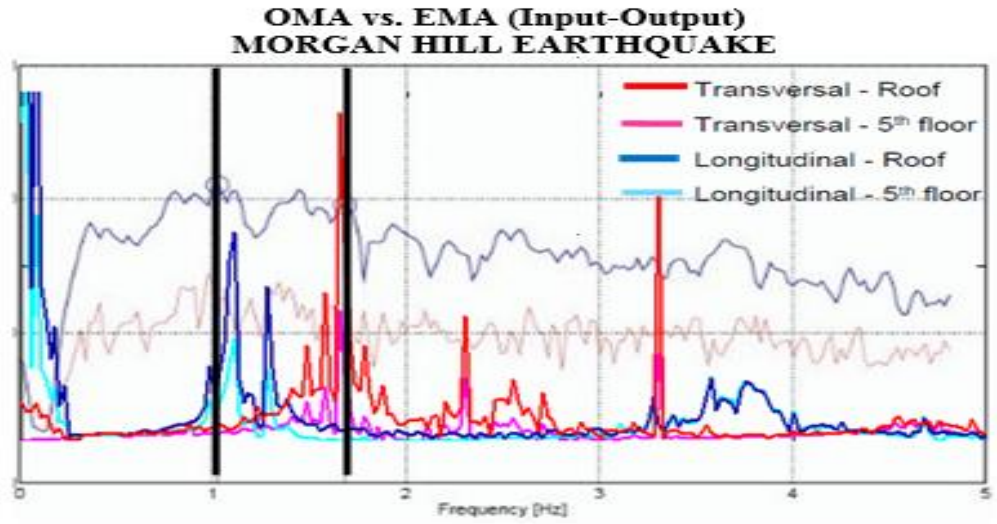

Fig. 6. OMA and input-output EMA results comparison in frequency domain for Morgan Hill.

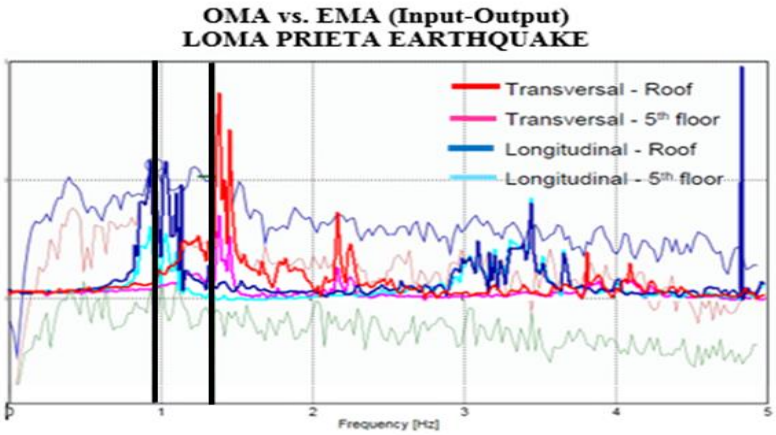

Fig. 7. OMA and input-output ema results comparison in frequency domain for Loma Prieta.

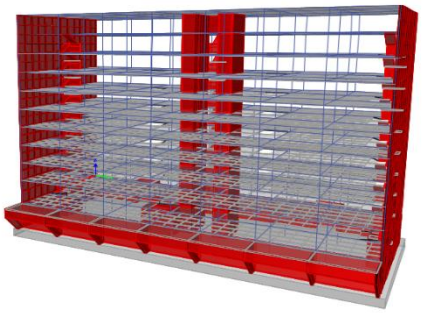

Fig. 8. 3D view of the ETABS model of the building.

4.3. Validation and updating of the model

In order to validate the model, time history analysis for the other two different earthquakes, one with a lower shaking (Mount Lewis) and the other one with a higher shaking (Loma Prieta) than Morgan Hill, were performed using the calibrated model. The same procedure used for Morgan Hill earthquake was followed. Whereas the model was performing well for Mount Lewis, the response of the model was not as good as expected for Loma Prieta. The results obtained for this last earthquake were not matching the experimental ones as desired.

The first and second natural frequencies, for the first calibrated ETABS model were compared to the ones obtained through modal analysis for each of the events. Both modal analysis techniques showed that the first natural frequency of the building occurs approximately at the same frequency of 1 Hz. However, the second natural frequency corresponding to the transversal mode of the structure slightly change depending on the earthquake. While for Morgan Hill, and consequently the calibrated FE model, this second natural frequency was shown to be 1.66 Hz, for Loma Prieta, the building responded more flexible with a natural frequency of 1.22 Hz. Therefore, a new FE model was created to capture better the less stiff response of the building under Loma Prieta earthquake.

No damage was detected in the building after any of the events. Consequently, none of the structural properties could have been changed. The increase of the flexibility of the building in the transversal direction, where the shear walls are acting as the lateral resisting system, for Loma Prieta event could be caused by the increase of the rocking effects. Hence, the first calibrated model was updated reducing the transversal stiffness of the springs from 0.1 k/in/in^2 to 0.02 k/in/in^2 and adding vertical springs in order to allow the building to rock. The natural frequencies of this second updated finite element model were compared to the ones obtained from the experimental data and a good match was obtained (see results in Table 2). The time histories and response spectra for acceleration, velocity and displacements obtained from the FE model for all of the channels were compared to the experimental data for each of the events. Good correlation coefficients between analytical and experimental results were obtained if the first calibrated model is used for Morgan Hill and Mount Lewis events and the more flexible updated model for Loma Prieta earthquake.

4.4. Results

The comparison between the experimental and analytical results is shown in this section. As mentioned in previous sections, natural frequencies, time histories and response spectra obtained from the FE model and the measured data are compared and good correlation is achieved.

4.4.1. Natural frequency comparison

The following table shows the natural frequencies obtained from both modal analysis techniques (OMA and input-output EMA) and compares them to the natural frequencies of both FE models (the first calibrated model and the more flexible updated model).

As mentioned in previous sections, a first longitudinal natural frequency of around 1 Hz was captured accurately by all the performed experimental modal analysis. Both FE models present the same natural frequency in that direction too. However, for the transversal direction either OMA or input-output EMA show a natural frequency decrease for Loma Prieta earthquake. The more flexible FE model matches this lower first transversal natural frequency of the structure (of around 1.25 Hz).

Table 2. First natural frequencies in longitudinal and transversal direction obtained from the experimental data and the FE models

EARTHQUAKE	Experimental				FE Model			
	OMA		Input-Output EMA		First Model		Flexible Model	
	$f_{1st\ longitudinal}$	$f_{1st\ transversal}$	$f_{1st\ longitudinal}$	$f_{1st\ transversal}$	$f_{1st\ longitudinal}$	$f_{1st\ transversal}$	$f_{1st\ longitudinal}$	$f_{1st\ transversal}$
Morgan Hill	1.03	1.66	1.1	1.65	1.06	1.66	1.07	1.28
Mount Lewis	1.07	1.56	1.12	1.65				
Loma Prieta	0.95	1.22	1.05	1.35				

4.4.2. Time history comparison

The first calibrated model was used to perform a time history analysis of the structure for Morgan Hill and Mount Lewis earthquakes, while the second updated model was used for Loma Prieta earthquake. The comparison between the absolute acceleration, velocity and relative displacement time histories for the recorded motions and the analytical motions show a good match in all the channels. The models captured the peaks, frequencies and values of the time histories quite accurately. The correlation coefficient (C.C.) between the experimental and analytical data was also calculated. The average of the C.C. for all the events was 85% with a minimum of 73%, which indicates a good correlation for practical purpose.

The relative displacements were obtained by subtracting the displacement at the basement to the total displacement of each channel. Therefore, the relative displacements account for the displacements due to the rocking and bending of the structure. Fig. 9 shows the comparison of the time histories of acceleration, velocity and relative displacement for two channels at the roof of the building, channel 5 (longitudinal) and 4 (transversal) for Morgan Hill earthquake.

4.4.3. Response Spectra Comparison

Acceleration, velocity and displacement spectra of the recorded measurements and the obtained from the finite element model were compared. 5% damping was considered for all the cases. Velocities and displacements for the measured data were obtained by integration of the recorded acceleration.

For all the events in all the channels good correlation was obtained in the studied period range of 0 to 4 sec. In all the cases, the highest error were obtained for both first natural periods of the structure; T = 1 sec / f = 1 Hz in longitudinal direction and T = 0.6 sec / f = 1.6 Hz (for Morgan Hill and Mount Lewis) and T = 0.77 sec / f = 1.2 Hz (for Loma Prieta) in transversal direction. For the rest period values, in which the structure is not excited that much, the FE model perfectly matches the response of the real building. The average of the maximum errors obtained at the peaks from the response spectra for each channel is computed; resulting in 11.4% for acceleration spectra and 15% for velocity and displacement spectra.

Figs. 8, 9 and 10 show the acceleration, velocity and displacement spectra obtained for Loma Prieta earthquake in the longitudinal direction. As explained above, the difference between the data measured by CSMIP and the FE model is higher at the main peak. Responses at the 5th floor and roof are plotted as well as the input in the basement.

5. Discussion of the Results

The results presented in the previous section showed that the response of the building under higher level of shakings can be captured by a proper modeling of the soil structure interaction (case of more flexible FE). Lower stiffness spring foundation will let the building to rock, increasing the horizontal motion of the structure and decreasing the natural frequencies. The following formulation shows the relation between the frequencies for a fixed system (w_{fix}) and a system accounting for SSI (w_{SSI}).

$$w_{SSI} = \frac{w_{fix}}{\sqrt{1+\frac{k_c}{k_h}+\frac{k_c * h^2}{k_r}}} \quad , \tag{1}$$

where h is the height of the structure, k_c the stiffness of the structure, k_h and k_r the translational and rotational stiffness of the structure respectively. In case of fixed base, k_c and k_r are equal to 0;hence, $w_{fix} = w_{SSI}$. However, if k_h and k_r are considered w_{SSI} will be reduced. Hence, it

is proved that the net effect of accounting for SSI is a reduction of the fundamental frequency.

The importance of the proper design of the soil structure interaction in the model is fundamental to characterize the real response of the building. It also was shown that the intensity of shaking affects the soil-structure interaction, becoming softer and more important for stronger shaking (Loma Prieta case) than for lower shaking (Mount Lewis and Morgan Hill cases).

6. Conclusions

Modal identification of a ten-story concrete shear wall building located in San Jose, California, was performed using OMA and input-output EMA. The recorded motions during Morgan Hill, Mount Lewis and Loma Prieta earthquake at different levels and locations of the structure were used. It was demonstrated that for the stronger shaking record, Loma Prieta, the building presented a lower fundamental frequency in the direction of the shear walls than for the other two earthquakes.

A FE model of the building was manually calibrated using the recorded motions during one of the low intensity shaking earthquakes (Morgan Hill). The natural frequencies obtained from the FE model were compared to the ones obtained through both experimental modal analysis approaches. Acceleration, velocity and relative displacement time histories, as well as, response spectra for the measured and the data obtained from the FE model for different channels were also compared. Good match between the experimental and analytical results was obtained for the two low intensity earthquakes (Mount Lewis and Morgan Hill). Nevertheless, a new more flexible FE model needed to be created in order to capture correctly the more flexible transversal response of the structure during Loma Prieta earthquake. For this last model softer springs were added to the base allowing the structure to rock.

In conclusion, in some cases soil-structure interaction becomes important and cannot be neglected. The nonlinear behavior of the soil could significantly affect in the prediction of the response of certain buildings. Modeling a building without considering these effects may not be enough to capture properly the behavior of the building under different ground motions.

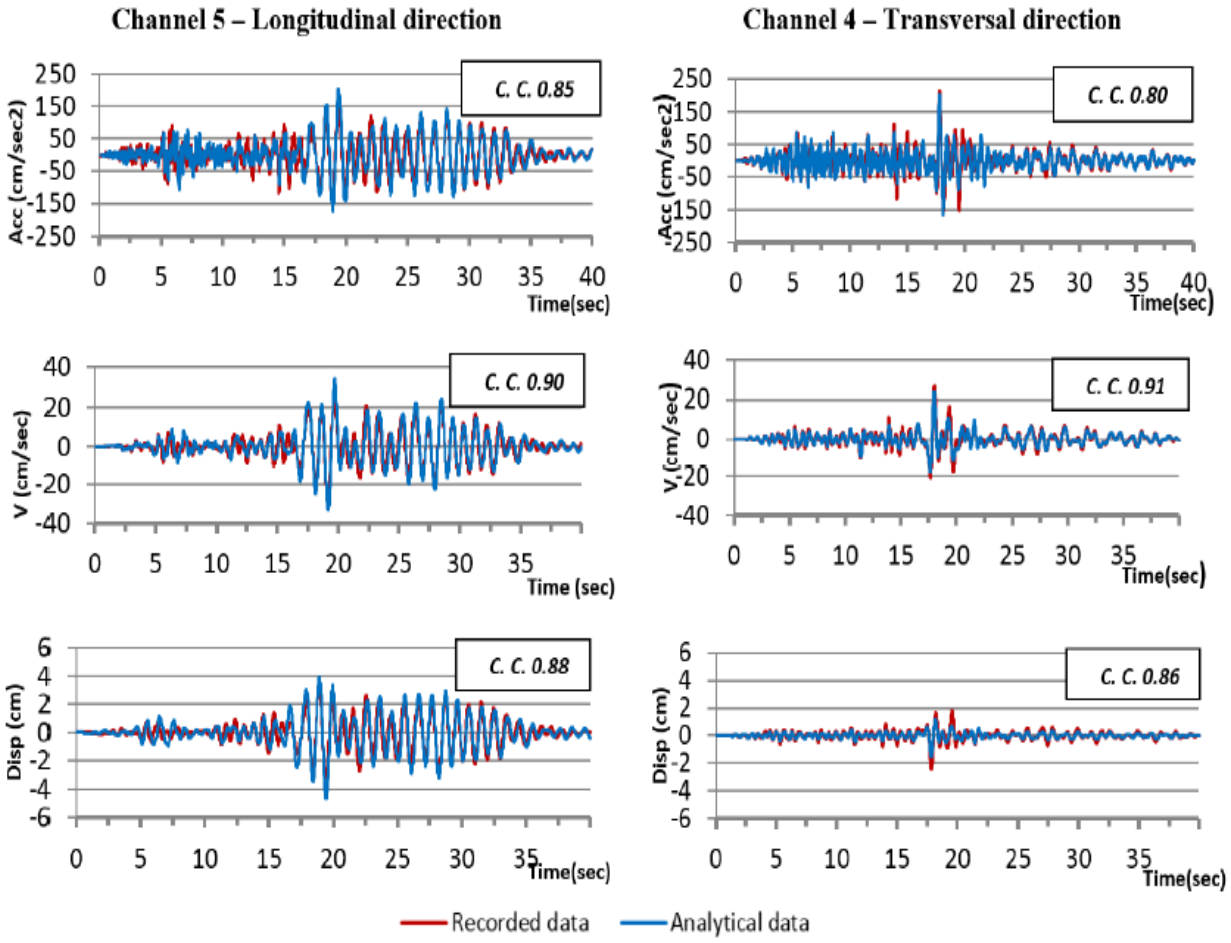

Fig. 9. Recorded and analytical acceleration, velocity and relative displacement time histories at channels 5 and 4 for Morgan Hill earthquake.

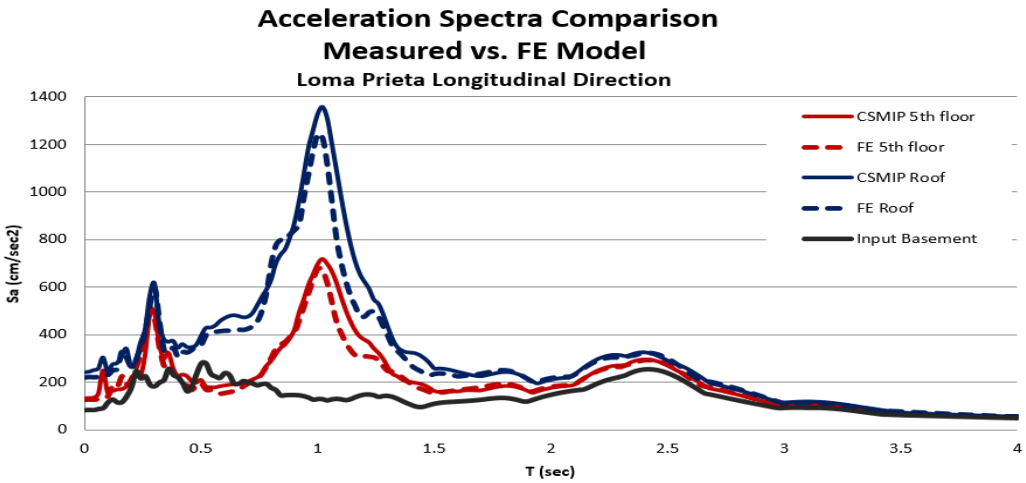

Fig. 10. Acceleration spectra comparison for loma prieta earthquake in the longitudinal direction of the structure.

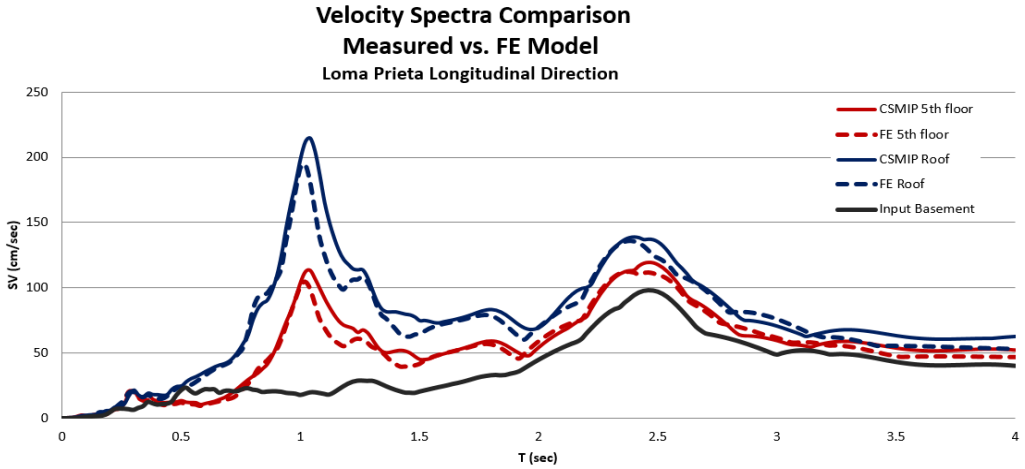

Fig. 11. Velocity spectra comparison for loma prieta earthquake in the longitudinal direction of the structure.

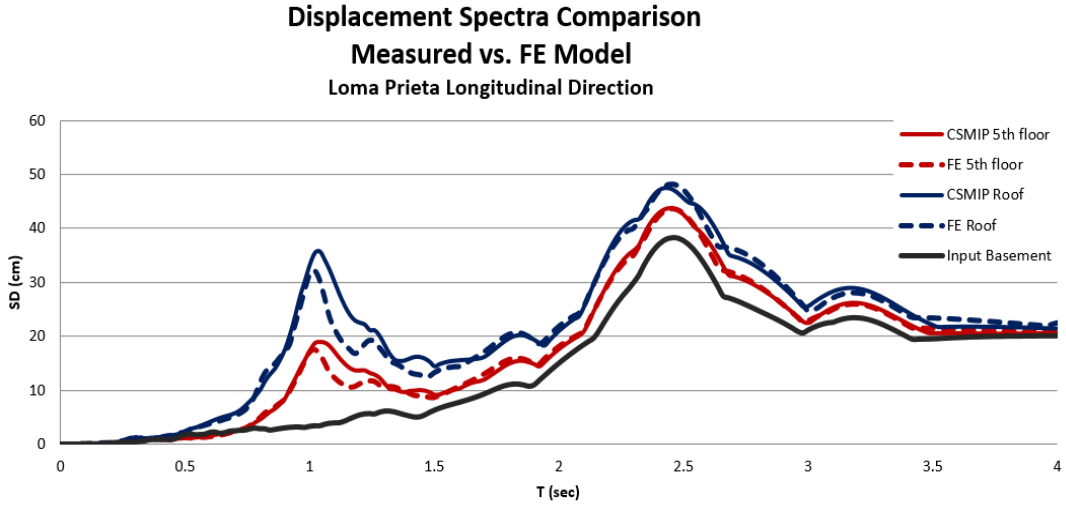

Fig. 12. Displacement spectra comparison for loma prieta earthquake in the longitudinal direction of the structure.

REFERENCES

CESMD (2016). Center of Engineering Strong Motion Data. http://www.strongmotioncenter.org. Downloaded on 10-01-2016.

Gazetas G (1983). Analysis of machine foundation vibrations: State of the art. *International Journal of Soil Dynamics and Earthquake Engineering*, 2(1), 2-42.

Martinez AV (2015). Modeling of a Building Subjected to Different Ground Motions. IMAC XXXIII, Springer Inc., Orlando, USA.